Gyroid Structured Polymer Templates for Optical Applications

This dissertation is submitted for the degree of Doctor of Philosophy
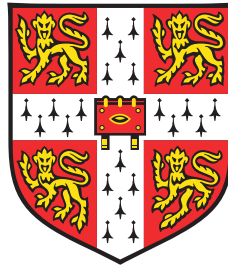
Raphael Dehmel

Jesus College

18th February 2016

Supervisor:

Prof. Ullrich Steiner

Cambridge University

Department of Physics

Declaration

This dissertation is the result of my own work and includes nothing which is the outcome of work done in collaboration except as declared in the Preface and specified in the text.

It is not substantially the same as any that I have submitted, or, is being concurrently submitted for a degree or diploma or other qualification at the University of Cambridge or any other University or similar institution except as declared in the Preface and specified in the text. I further state that no substantial part of my dissertation has already been submitted, or, is being concurrently submitted for any such degree, diploma or other qualification at the University of Cambridge or any other University of similar institution except as declared in the Preface and specified in the text.

It does not exceed the prescribed word limit of 60,000 words set by the Degree Committee for the Faculty of Physics & Chemistry.

The work presented in Chapter 4 was carried out in collaboration with Dr. M. R. J. Scherer. Chapters 5 and 6 are the outcome of collaborative work with J. A. Dolan, with significant contributions from Dr. B. D. Wilts and Dr. I. Gunkel. The experiments described in Chapter 7 were designed and conducted in collaboration with Dr. B. D. Wilts, and were inspired by Dr. S. Salvatore. Chapter 8 describes work carried out in collaboration with Dr. A. Abate and Prof. C. Neto.

Cambridge, February 2016

Raphael Dehmel

Acknowledgements

The work described in this dissertation was carried out between October 2012 and February 2016 in the laboratories of Thin Films and Interfaces group. During this time I have benefited greatly and in many ways from the interactions with various people, and I would like to take this opportunity to express my gratitude.

Firstly, I would like to thank my supervisor Professor Ullrich Steiner, who entrusted me with a PhD position and provided an excellent infrastructure for my research. Despite his busy schedule he was always able to answer my questions and provide useful advice. I am deeply grateful for the freedom I enjoyed when pursuing my work, and the friendly work environment Ulli created with his laid-back style of leadership.

I would also like to thank Professor Jeremy Baumberg, who generously granted me access to his excellent optics equipment, and agreed to formally stand in as my supervisor when Ulli moved to Switzerland. The time he and Angela Campbell spent with petty administrative work on my behalf is highly appreciated.

I am especially grateful to Karl Gödel, who was not only a great friend and colleague, but also helped me significantly in many ways by introducing me to the python programming language, which became an important tool for a large part of the work presented here. He selflessly guided me in my amateur attempts at creating programs for automated experimentation and data analysis, and saved me at least several weeks of trial and error. His expertise and helpfulness made him my first point of contact whenever I needed advice in matters of software and graphic design, and I would like to thank him for all the valuable lessons he taught me.

I would also like to thank Maik Scherer, who supervised me in the early days of the work presented here. He provided me with excellent laboratory

Contents

1

Bottom Up Nanofabrication

What would the properties of materials be if we could really arrange the atoms the way we want them? They would be very interesting to investigate theoretically. I can't see exactly what would happen, but I can hardly doubt that when we have some control of the arrangement of things on a small scale we will get an enormously greater range of possible properties that substances can have, and of different things that we can do.

– Richard P. Feynman, December 1959

The above quote is only one of many insightful and visionary statements issued by Richard Feynman in his famous 1959 Caltech lecture *There's plenty of room at the bottom.*[1] The paragraph is reprinted here in full length as it summarizes the motivation for all aspects of the work presented in this dissertation surprisingly well. Looking back on the entire lecture it is astonishing how accurately some of Feynman's more than 50 year old ideas describe today's reality. In fact, many of the techniques he postulated have become so common that life without their products is hardly imaginable.

The most significant example is without doubt the miniaturisation of electronic devices and computers. Mass-produced "wires" on integrated circuits are still orders of magnitude larger than the suggested "10 or 100 atoms in diameter", but even the most basic phones of today significantly outperform barn-filling supercomputers of Feynman's time. Computing has rapidly transformed nearly all aspects of our lives and is an impressive example of the enormous impact scientific development can have on society.

The techniques involved in the production of modern microprocessors all

fall into the *top-down* category, where external tools are used to machine and rearrange material into the desired shapes. These tools and the strict requirements to the environment they operate in, drive the cost of production plants for state of the art processors well into the billions of dollars.[2]

With this in mind the nanostructures spontaneously formed by nature are all the more impressive. The replication of DNA-strands, for example, works to single molecule precision with incredible reliability in a wide range of environmental conditions. It is a typical example for *bottom-up* techniques, where molecule-sized building blocks self-organise into functional shapes due to their chemical properties. The sheer number and variety of organisms and structures that nature forms this way is hard to grasp, and the underlying mechanisms are often difficult to uncover. Crystallisation — in some ways the most basic example of self-assembly — is well understood and an important aspect of the semiconductor fabrication procedures mentioned above. Here silicon crystals are modified by adding minute amounts of dopant atoms, drastically changing their electronic properties.

The implementation of more advanced bottom-up methods in commercial applications is still very much in its infancy. One example of an emerging technique is the controlled folding of DNA strands, often referred to as *DNA origami*.[3] Introduced by Paul W. K. Rothemund in 2005 it begins with a DNA-strand with a known sequence of bases. Short *staple strands* are added and bind to specific base sequences on the large strand. The two ends of the *staple strand* are designed to bind to non-neighbouring sequences, forcing the main strand to fold in a predefined way. This principle can be used to raster-fill a wide range of shapes or even self-assemble into more complex geometries with a resolution of about 6 nm. Applications mainly focus on drug delivery at the moment,[4, 5] more exotic examples include nanorobots and computing.[6]

Lipid bilayers are another system that is tested for drug delivery applications. They consist of amphiphilic molecules and form a large variety of membranes in living organisms.[7] The hydrophobic ends of neighboring molecules attract each other, as do the hydrophilic ends. The forces between different ends are repulsive though, limiting the number of energetically favorable arrangements. In polar solvents the hydrophobic ends will typically be on the inside of a structure with a completely hydrophilic surface. A small number of molecules will generally assemble into a spherical

micelle. When the number of molecules is increased, more complex morphologies such as cylinders, double layered spheres (so-called *liposomes*) or bilayers are formed. Lipid bilayers are very effective cell membranes as their permeability is highly selective and their flexibility makes them less susceptible to mechanical destruction.[8] Liposomes are common cross-membrane transport vehicles in living organisms and thus interesting candidates for drug delivery systems. Other applications of lipid bilayers are mostly research tools such as binding sensors[9] or model systems for drug permeability studies.[10] The small size and spherical shape of the hydrophilic part of the amphiphilic molecules are important for the formation of stable membranes, but they also limit the number of possible geometries significantly. Moreover, the fact that the morphologies of lipid assemblies are only stable in liquid environments prohibits a combination with many other fabrication techniques.

When large numbers of molecules are connected to so-called polymers, the resulting macromolecules can be dramatically different from a blend of the non-polymerised molecules in terms of their mechanical and chemical properties. The often chain-like geometry of polymers has interesting statistical implications that can, for example, cause elasticity or increased tensile strength, even in the case of homopolymers where all repeat units are identical. The properties of polymers can be tuned across vast ranges and they are omnipresent in our daily lives in the form of rubbers, plastics, and synthetic fibres.

They can, however, also be used for very complex and versatile bottom-up techniques, such as polymer self-assembly. The individual constituent molecules of two different homopolymers can be chemically very similar. In contrast to lipid systems, the forces between them are typically too weak to influence their spatial arrangement in a non-polymerised blend. With increasing chain-length, however, the entropy of mixing decreases and eventually phase separation becomes energetically favourable. In order to form regular structures, this phase separation has to be limited to the desired length scale. This can be achieved by connecting pairs or groups of different homopolymers to form so-called block copolymers. Compared to lipid systems, a much richer variety of morphologies can be created by adjusting the volume ratios of the various homopolymer blocks. Furthermore the structures are stable without surrounding media and under certain circumstances

individual blocks can be removed without affecting the rest of the material. This facilitates a combination with various other fabrication techniques and is the basis of large parts of this work. Chapter 2 will comprehensively discuss the physics of polymer self-assembly, and introduce the gyroid: a triply periodic minimal surface separating two continuous labyrinth networks. Polymers self-assembling into this geometry are very interesting for various applications as both networks are self supporting and can be used as templates for further processing.

The various fabrication and characterisation techniques utilised in the course of the presented work will be introduced in Chapter 3. The aim here is to explain the basic principles of relevant aspects only. The interested reader will find references to more exhaustive documentation.

The suitability of polymer self-assembly for nanofabrication applications and its compatibility to other techniques is demonstrated in Chapter 4. Here, a self-assembled polymer template is used in combination with conventional photolithography to pattern a conjugated polymer on two different length scales. Finally, a functional device is manufactured from the material and its performance is shown to be superior to its non-patterned equivalent.

The main goal of this dissertation was the development of a reliable fabrication pathway for gyroid structured polymer templates with enhanced long range order. This is a prerequisite for the characterisation of the anisotropic optical response of gyroid structured gold: To avoid averaging over multiple unit cell orientations, the long range order of the material must exceed the beam footprint of the optical probe. Chapter 5 discusses the related experimental work and the resultant findings. Briefly, thin polymer films are exposed to precisely controlled atmospheres of solvent-rich nitrogen gas. Depending on solvent concentration and exposure time, a range of different morphologies is observed. By carefully varying the concentration over several hours, long range order can be enhanced from less than ten micrometers to millimetre scales. The resulting films are turned into nanoporous gold structures via selective etching and electrodeposition. Goniometer measurements are performed in transmission and reflection to facilitate the modelling of the anisotropic electromagnetic parameters of the material.

The optimisation of the annealing protocols for the formation of the long range order is greatly aided by the phenomena discussed in Chapter 6:

Large birefringent structures are observed in the annealed polymer films, and they are found to be congruent with the domains of microphase separation. Further characterisation is carried out and reveals that the birefringence is caused by preferentially aligned crystallisation within the gyroid network.

A novel technique for measuring surface plasmon resonances is presented in Chapter 7. Surface plasmons play an important role in a wide range of sensing techniques, often in clinical and commercial contexts. Their resonances can be measured in the form of a dip in the angular reflectance spectrum and are highly sensitive to environmental conditions. State-of-the-art devices determine the angular reflection by mechanically moving the light source and detector through a range of angles. The technique proposed here allows the single-shot acquisition of a full angular reflectance spectrum. Furthermore, electrically switchable filters enable fast and movement free measurements over wide spectral ranges, facilitating the rapid characterisation of the plasmon resonance dispersion.

Chapter 8 revolves around the functionalisation of substrate surfaces. Locally manipulating the surface energy of a substrate is a nanofabrication technique of its own. Here, the focus lies on its complementary use to other methods, mainly in preventing de-wetting due to surface energy mismatches of sample material and substrate surface. In particular a new kind of self-assembled monolayer based on halogen bonding is introduced and characterised thoroughly.

In summary, the work presented in this dissertation revolves around various applications of artificially induced self-assembly and related characterisation methods. A focus lies on the self-assembly of polymers into the gyroid morphology and their use as templates for technical applications and scientific investigations.

2

Self-Assembly in Block Copolymers

Block copolymers are a large family of macromolecules, defined by their composition of multiple different homopolymers. The individual polymer blocks are connected in a sequential or branched fashion by covalent bonds, giving rise to a theoretically infinite number of possible configurations. The chemical and mechanical properties of block copolymers can be tuned across a vast range as they are defined by the nature and number of monomers in each block as well as the arrangement of the blocks. Unsurprisingly, block copolymers can be found in many commercial products, often in the form of protective coatings, functional adhesives, or thermoplastic elastomers with superior mechanical properties.[11]

In the majority of these applications the individual chains are randomly distributed and isotropically oriented in the material, creating a homogeneous substance. Under certain conditions however, repulsive forces between different polymer blocks can become strong enough to cause local de-mixing. In a blend of homopolymers this de-mixing would eventually lead to phase separation, similar to what can be observed when mixing oil and water at room temperature. Confined by the covalent bonds, the individual blocks of a block copolymer can however only separate on nanometre length scales. This is commonly referred to as microphase separation and can manifest itself in a variety of well defined periodic structures.

The aim of this chapter is to give a brief overview of the underlying mechanisms of this process, especially with regard to the practical challenges

associated with experimental work.

2.1 Thermodynamics of Block Copolymers

Block copolymer molecular weights are typically on the order of 10 to
100 kg/mol. This implies that a 1 μm thick film contains 10^{14} or more mo-
lecules per cm². Such complex systems can only be analysed statistically
within the framework of thermodynamics. Energetically stable configura-
tions of a many body system coincide with minima of its *Gibbs free energy*,
defined as $G = H - TS$.[12]

When the system consists of two or more groups of chemically distinct
particles, the entropy S increases with disorder and therefore favours com-
plete mixing. This tendency increases with increasing temperature T. The
enthalpy H on the other hand is typically increased when molecules of dif-
ferent kinds come close together, favouring a separation of the system into
two pure phases. The competition between these two terms determines the
mixing behaviour of molecules, but their quantification is far from trivial.

The most important approach to this challenge is undoubtedly the liquid
lattice model, developed independently by Maurice L. Huggins and Paul J.
Flory in 1941.[13,14] This model and its predictions for polymer solutions
and blends are briefly described here, following Flory's book from 1953[15]
unless otherwise specified.

2.1.1 Statistics of Polymer Solutions

First the entropic term of the free energy is evaluated by making a number
of simplifying assumptions and counting all possible states of the system.

The Flory-Huggins model approximates a polymer solution as a liquid
lattice with n_0 cells that each have z nearest neighbours and can be occupied
by either a segment[1] of polymer A, or a molecule of solvent B. A number of
assumptions are made, which remove all but one constraint from the system:
the polymer segments occur only in interconnected chains of length N_A.

Now, a situation is considered where i polymer molecules are in the sys-
tem and an additional one is added, effectively by sequentially replacing N_A

---

[1]Note that the segments are *not* equivalent to the chemical repeat units. Flory divides
the polymer into equally sized portions that each take up the same volume as one solvent
molecule. The number of segments x is proportional to the degree of polymerisation of
the polymer, which is defined as the number of chemical repeat units.
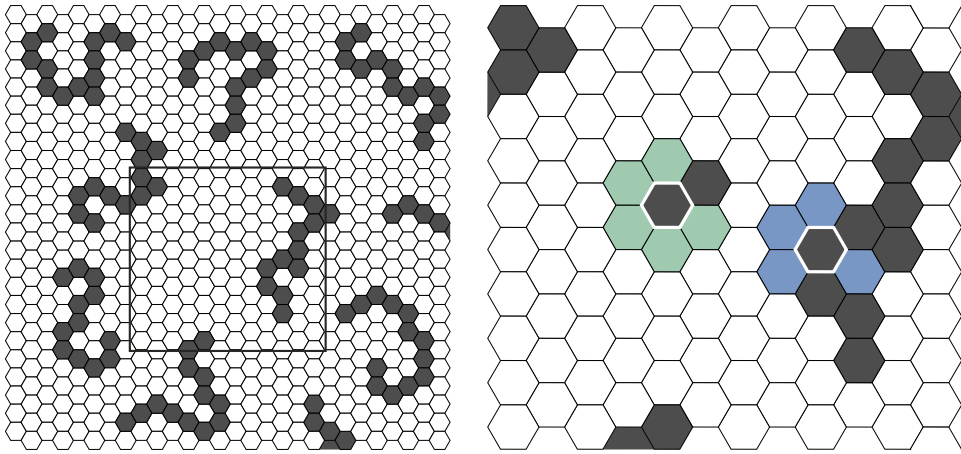
Figure 2.1. Illustration of the liquid lattice model. The Flory-Huggins theory is based on the modelling of a polymer solution to a liquid lattice, where all sites are occupied by either a solvent molecule or a polymer segment. The model is applicable to arbitrary geometries, and a hexagonal lattice with $z = 6$ nearest neighbours per site is shown here. Left: A fraction f_A of the lattice sites is occupied by polymer segments (grey). All solvent sites (white) are possible starting points for the insertion of additional polymers. Right: In a magnified view of the lattice such an insertion event is illustrated. There are $z - 1 = 5$ possibilities for the placement of additional segment (green), and the probability of this site being occupied by a solvent molecule is $f_B = 1 - f_A$. Also shown is the number $z - 2 = 4$ of free nearest neighbour contacts for a mid-chain polymer segment (blue).

solvent molecules with polymer segments. The number of solvent molecules in the system is $n_B = n_0 - i \cdot N_A$, and each of them occupies a possible position for the first segment of the additional chain. The number of options for the second segment is simply the number of connected lattice positions multiplied by the probability of finding a solvent molecule in any lattice cell and can be written as $z \cdot (n_0 - N_A \cdot i)/n_0$. All further segments are assumed to have $(z - 1)(n_0 - N_A \cdot i)/n_0$ possible positions, taking into account the blocking of a neighbouring lattice cell by the previous segment, as shown in Figure 2.1. Potential self-intersection, where two polymer segments occupy the same lattice site, is neglected, causing an overestimation of the number of possible states.

The number of possible configurations per polymer chain can be obtained by sequentially multiplying the number of possible states for each of its segments and dividing this number by two to account for the indistinguishability of two reverse but otherwise identical chains. Multiplication of the values for all numbers of polymers i from 1 to the final number of polymers n_A and the interchangeability correction factor $1/n_A!$ yields the number

of possible system states W. With Boltzmann's equation $S = k_\text{B} \ln W$, the entropy of mixing can be written as

$$\Delta S_\text{mixing} = -k_\text{B}\{n_B \ln[n_B/(n_B + N_A n_A)] + n_A \ln[N_A n_A/(n_B + N_A n_A)]\}.$$

An additional term of

$$k_\text{B} n_A (N_A - 1) \ln[(z - 1)/e]$$

was omitted here, as it is only relevant when the mixing of solvent molecules with perfectly ordered chains is considered. For $N_A = 1$ the formula is equivalent to the entropy of mixing of two ideal gases. It is worth noting that even with the overestimation due to the neglected self-intersection the number of possible states greatly decreases with increasing chain length. The entropic term in the free energy thus becomes less significant and the enthalpic term dominates.

2.1.2   The Enthalpy of Mixing in Polymer Solutions

In order to predict the mixing behaviour of the system, the entropy has to be compared to the enthalpy or heat of mixing as described above. The liquid lattice model can also be utilised for this purpose.

Interaction energies w_{AB}, w_{AA}, and w_{BB} are associated with all neighbouring pairs of unlike or like molecules or segments, respectively, and all other interactions are neglected. In a situation where polymer and solvent are in completely separate locations only w_{AA} and w_{BB} terms occur. Now a hypothetical mixing event is considered, where one solvent molecule and one polymer segment swap their positions (momentarily ignoring the condition on polymer connectivity). Both swapped units now interact with z neighbours of the opposing species, meaning that the total interaction energy is reduced by $z \cdot w_{AA}$ and $z \cdot w_{BB}$, and increased by $2 \cdot z \cdot w_{AB}$.

The energy balance of creating a single interaction between unequal units can therefore be written as

$$\Delta w_{AB} = w_{AB} - (1/2)(w_{AA} + w_{BB}).$$

The next step is to simply count the number of interactions for randomly distributed polymers in the solution: Each polymer segment has $z - 2$ free

nearest neighbour interactions, with the exception of the two terminal units which have an additional one each. The number of possible interactions per polymer is $(z - 2) \cdot N_A + 2$, which is approximated by $z \cdot N_A$. This number is then multiplied by the probability of finding a solvent molecule in any given lattice cell $f_B = n_B/(n_B + N_A \cdot n_A)$ and the number of polymers n_A to obtain the number of unequal interactions $zN_A n_A v_1$. The total heat of mixing can then be written as

$$\Delta H_{\text{mixing}} = k_{\text{B}} T \chi n_A f_B,$$

where χ, a dimensionless measure for the interaction energy per polymer chain, is defined as

$$\chi = z \Delta w_{AB} N_A / k_{\text{B}} T.$$

χ is commonly referred to as the *Flory-Huggins interaction parameter* or simply *Flory parameter* and has been used in the majority of polymer thermodynamics literature since it was introduced. It is typically positive as it originates from van der Waals interactions caused by the polarisabilities of the molecules involved.[16]

It can be adapted to account for blends of homopolymers by simply replacing the n_B single-cell sized solvent molecules with n'_B polymer molecules occupying $N_B = n_B/n'_B$ cells each. The advantage of this model is the reduction of a complex multi-body interaction to a single material specific parameter, facilitating quantitative predictions on the miscibility of polymer mixtures.

Experimentally, χ can be determined indirectly by measuring osmotic pressure[17] or vapour pressure.[18] Its scaling with the volume fraction is in reasonable agreement with the theoretical predictions,[14] more complex dependencies have, however, also been reported.[19]

In theory the Flory parameter χ is inversely proportional to the temperature T. An empirical relation of the form

$$\chi = K + \frac{L}{T}$$

has been established as a more accurate representation of experimental findings in many cases.[2] Values for K and L tend to be positive and on the order

---

[2]The two parameters are often named A and B in the literature. Here, K and L are

of 10^{-3}–10^{-1} and 10^0–10^1 respectively.[20] U and/or V can however also be negative and/or outside these ranges, and experimentally determined values are only valid in narrow temperature regimes.

2.1.3 Diblock Copolymers and Microphase Separation

In comparison to the homopolymer blends, block copolymers are further constrained by the covalent bonds between their constituent homopolymers. This means their behaviour in solution or in the melt is more complex and a new approach is required to identify the conditions under which they phase separate. A theoretical framework to investigate and quantify the ordered states in diblock copolymers was presented by Ludwik Leibler in 1980.[21] His key assumptions and conclusions are summarised here, without going into the details of the rather advanced mathematical methods.

Leibler discusses a melt of diblock copolymers consisting of N_A units of polymer A, and N_B units of polymer B, each. The total chain length is $N = N_A + N_B$ for all molecules. A volume fraction f is defined as $f = N_A/N$, and — assuming incompressibility — the local density of monomers $\rho_A(\vec{r}) + \rho_B(\vec{r})$ is set to be constant and equal to 1. The interaction energy per monomer is $k_\mathrm{B}T\chi\rho_A\rho_B$.

The key element of Leibler's analysis is an order parameter

$$\psi(\vec{r}) = \langle (1 - f)\rho_A(\vec{r}) - f\rho_B(\vec{r}) \rangle. \tag{2.1}$$

The brackets denote the thermal average. With the above definitions and assuming equal volume and weight for the A and B monomers Equation 2.1 can be reduced to $\psi(\vec{r}) = \langle \rho_A(\vec{r}) - f \rangle = \langle \delta\rho_A(\vec{r}) \rangle$. ψ quantifies the average local deviation from the global monomer ratio and is 0 at all points in a disordered system. Disorder occurs when the entropic terms, which decrease with increasing N, dominate over the enthalpic terms that scale with χ. For larger χN the enthalpic terms will become dominant and $\delta\rho_A$ will show large fluctuations. The density-density correlation function

$$\vec{S}(\vec{r} - \vec{r}^{\,\prime}) = \frac{1}{k_\mathrm{B}T}\langle \delta\rho_A(\vec{r})\delta\rho_A(\vec{r}^{\,\prime}) \rangle,$$

and in particular its Fourier transform $\vec{S}(\vec{q})$ are investigated with a *ran-*

---

used instead, to avoid confusion with the labels of the molecular species.

dom phase approximation method, adapted from de Gennes.[22] Here, the polymers are assumed to behave like ideal chains (without neighbours) and monomer–monomer interactions are accounted for through correction terms to the external potentials. The analysis reveals that only density fluctuations on a specific length scale become "anomalously large" and that $\vec{S}(\vec{q})$ shows a narrow maximum at $|\vec{q}| = q^* \neq 0$ as χ approaches the transition point value χ_t. Interestingly, the calculations reveal that q^* is independent of χ, indicating that the formed morphology is not influenced by the segregation strength.

To determine the phase behaviour of the material, Leibler examines an expansion of the free energy density $F(\vec{q})$. Terms of quadratic and higher order are evaluated around $|\vec{q}| = q^*$ and it is shown that ordered phases with a periodicity of $2\pi/q^*$ occur at $\chi N > (\chi N)_t$. Furthermore Leibler argues that due to the non-zero cubic term of F the ordering of the polymers is equivalent to a first order transition, i.e. the solidification of a liquid.

A more detailed analysis allows predictions of the dominant symmetries depending on the segregation strength χN and the volume fraction f, and a phase diagram is presented. If χN is continuously increased starting from a disordered polymer melt, the equilibrium morphologies are body-centred cubic spheres, hexagonally packed cylinders, and lamellae. A theoretical exception to this is the case of a symmetrical diblock with $f = 0.5$. Here the disordered phase is directly adjacent to the lamellar phase. The predicted value of 10.5 for $(\chi N)_t$ at $f = 0.5$ is a useful anchor point for the design of block copolymers for self-assembly purposes as it indicates under which conditions the phase separation can occur.

2.1.4 Block Copolymer Morphologies

The morphology of a self-assembled block copolymer is of paramount importance for nearly all scientific and commercial applications. In 1994 Matsen and Schick conducted a thorough analysis of the diblock system using a self-consistent mean field theory approach.[23] In addition to the phases discussed by Leibler they predict a region between the lamellar and cylindrical morphologies where the equilibrium morphology is the so-called double gyroid. The gyroid phase is very important for this work and will be discussed in Section 2.2. Matsen and Schick also discuss the catenoid-lamellar and ordered, bi-continuous, double-diamond phases that do not minimise the free energy
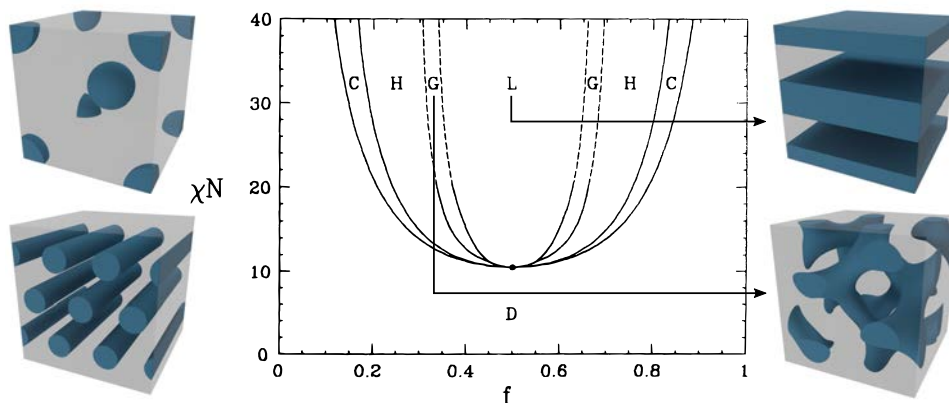
Figure 2.2. Diblock Copolymer Phase Space. Centre: diagram of the predicted morphologies of a di-block copolymer depending on volume fraction f and segregation χN. From Matsen and Schick, 1994.[23] Top left: body centred cubic spheres. Bottom left: hexagonally close packed cylinders. Bottom right: double gyroid. Top right: lamellae. The volume fraction f on the horizontal axis of the phase diagram corresponds to the blue phase in the visualisations.

at any point in the phase space. They are metastable phases as their energies are very close to the respective stable phase in certain regions of the phase space, and transitions between them are often infinitely slow. Matsen and Schick's phase diagram is shown in Figure 2.2 along with illustrations of the equilibrium morphologies.

The phase space of triblock copolymer systems is much richer than the one of the diblocks and can't simply be reduced to two dimensions. First, the arrangement of the blocks is of crucial importance: if the three blocks A, B, C, are all connected in one point, forming a so-called ABC star configuration, the confinement is fundamentally different to the linear case. Even if only linear triblocks are considered, there are three different possible arrangements, distinguishable by their central block. Also two volume fractions f_A and f_B are needed to fully describe the composition of the material. Moreover three different Flory-Huggins parameters χ_{AB}, χ_{BC}, and χ_{AC} have to be taken into account to determine the equilibrium morphology.[11]

Unsurprisingly, a large variety of morphologies can be observed in triblock systems and the stability or metastability of certain phases is subject to ongoing debate. The in some sense most basic morphologies are stacks of lamellae. Another fairly conceivable set of architectures can be derived from the remaining diblock phases: core-shell spheres,[24] cylin-

ders,[25] and gyroids[26] have been observed as well as alternating versions of them.[11, 27] More complex geometries arise for example when the end blocks both strongly repel the central block while the forces between them are relatively weak. In this case the middle block will no longer form a continuous layer between the two end blocks, and direct interfaces between them are formed. Bates and Frederickson discuss the scope of the triblock system in their 1999 publication.[11] They present a useful illustration of several possible morphologies for linear triblocks which is redrawn in Figure 2.3 to give the reader an impression of the vast variety of the phase space.

2.2 The Gyroid Morphology

In 1968 Alan Schoen discovered a triply periodic minimal surface he decided to name *gyroid* "to suggest the twisted character of its labyrinths".[28] Most of the work presented here revolves around self-assembling polymers capable of assuming morphologies equivalent to the gyroid's twisted labyrinths. This section gives a description of the most relevant features and properties of their rather complex geometry. Alan Schoen maintains a web page with extensive information including illustrations on the gyroid and the history of its discovery.[28] The information presented in this section is taken from this web page, unless otherwise specified.

2.2.1 Minimal Surfaces

Minimal surfaces are defined to be local minima in the area of the surface spanning a given closed contour. Before the discovery of the gyroid, the *P*, *D*, *H* and *CLP* surfaces described by Hermann Schwarz in 1865 and the Neovius surface of his student were the only known triply periodic examples of such surfaces. Their exact geometries and mathematical definitions are highly complex and of no direct relevance to this work. More information on them can be found, for example, in a book written by U. Dierkes *et al.*[29] The names of the *P* and *D* surfaces are derived from their simple cubic (primitive cubic) and face centred cubic (diamond) Bravais lattices, respectively.

The body centred cubic gyroid is in fact a hybrid of *P* and *D*, and can be constructed by a linear combination of their units cells. Schoen came across the Schwarz minimal surfaces, and eventually the gyroid, through
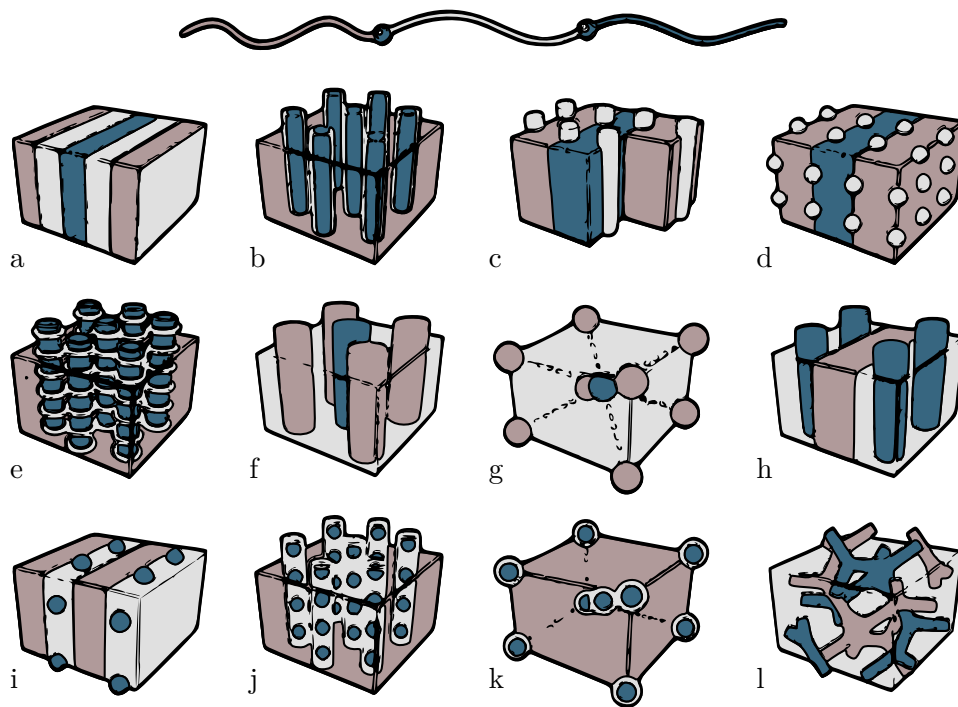
Figure 2.3. Triblock copolymer morphologies. Linear triblock copolymers can self-assemble into core shell or alternating versions of the diblock morphologies (b, k, and a, f, g, l, respectively). With two independent volume fractions and three interaction parameters their phase space is much more complex than the two-dimensional one of the diblocks and the number of possible morphologies is greatly enhanced. Redrawn from Bates and Frederickson, 1999.[11]
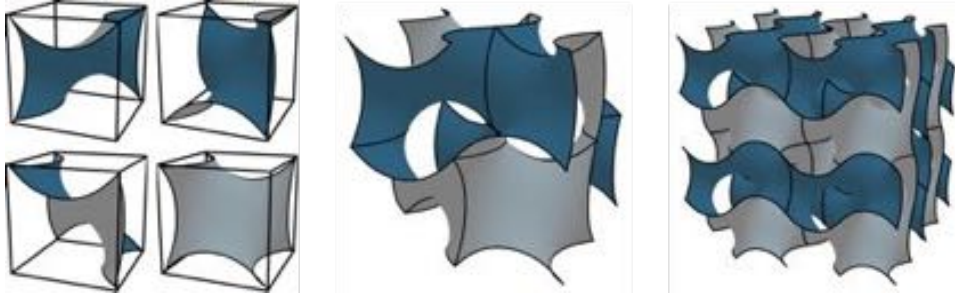
Figure 2.4. The gyroid minimal surface. Left: The skew hexagon in four different orientations. Center: Eight differently oriented skew hexagons combined to form a unit cell of the gyroid surface. The four front facing hexagons are individually shown on the left. Right: $2 \times 2 \times 2$ gyroid unit cells. All plots are of the *level-set* surface G^*.

his experiments on the vacuum forming of skew polygons. He describes the gyroid morphology in terms of a specific skew hexagon: "The infinite gyroid could in principle be constructed by first attaching a second hexagon to any open edge of an initial hexagon and then repeating the attachment process at every open edge of the developing assembly. Each attachment is implemented by applying a symmetry of the gyroid: a *half-turn* about an axis normal to the surface through the midpoint of each edge."

Figure 2.4 offers some assistance in understanding this rather abstract construction. The hexagon rotations become slightly more accessible when the cube frames drawn around them are considered. Each cube has two corners that don't coincide with corners of the inscribed hexagon. The position changes of these corners between neighbouring hexagon cells correspond to the respective rotations.

The graphs presented throughout this dissertation show the *level-set* surface G^* instead of the gyroid (G) surface. Level-set surfaces are defined through an equation that all points on the surface need to solve. This is very convenient for the implementation into computer algorithms and facilitates simple plotting and numerical analysis. The G^* surface is defined by the simple equation

$$\cos(x)\sin(y) + \cos(y)\sin(z) + \cos(z)\sin(x) = 0. \qquad (2.2)$$

It is not identical to the gyroid surface, but can be used to approximate it as the geometrical differences between the two surfaces are only minute.[30]

23

2.2.2 Symmetries of the Gyroid Surface

The space group of the gyroid is $Ia\bar{3}d$, where the I denotes a body centered cubic lattice and the a stands for a glide reflection consisting of a translation by half the lattice vector a and a mirror reflection by a plane parallel to that vector. A threefold rotation inversion symmetry is indicated by the $\bar{3}$, meaning that the system is symmetric with respect to a 120° rotation followed by a point reflection. The d describes a glide reflection along a full surface diagonal of the unit cell.

2.2.3 Gyroid-Shaped Polymer Networks

The interfacial area separating the different polymer blocks is minimised during self-assembly, constrained by the volume conservation condition and the limited monomer–interface distance. Minimal surfaces are therefore likely candidates for equilibrium morphologies, and the gyroid morphology was first identified in a diblock copolymer in 1994 by Hadjuk *et al.*[31] In a diblock system one of the blocks will form a "thickened" version of the gyroid surface, separating two continuous labyrinths filled by the other block. This configuration, and in particular the two separate networks, are commonly referred to as a *double gyroid*. The double gyroid consists of two *single gyroids* with surfaces approximated by the equation

$$\cos(x)\sin(y) + \cos(y)\sin(z) + \cos(z)\sin(x) = t. \qquad (2.3)$$

This equation can only be fulfilled for $|t| \leq 1.5$, and for $|t| < 1.413$ the solution divides the three dimensional space into two continuous networks.[32] Diblock copolymers can only form symmetrical double gyroids and the two intermaterial dividing surfaces (IMDS) are related by $t_1 = -t_2$. Triblock copolymers are less restricted and can self-assemble into symmetrical and asymmetrical double gyroids as well as core-shell double gyroids where five continous networks are formed. The symmetry group of the single gyroid is $I4_132$, which implies that compared to the G-surface or the double gyroid the inversion center is lost.[33] It is worth noting that the two single gyroids in a double gyroid are identical except for their opposite handedness and are thus referred to as an enantiomorphic pair. Figure 2.5 shows a single gyroid and a double gyroid, where all individual networks are confined by surfaces with $|t| = 0.9$.
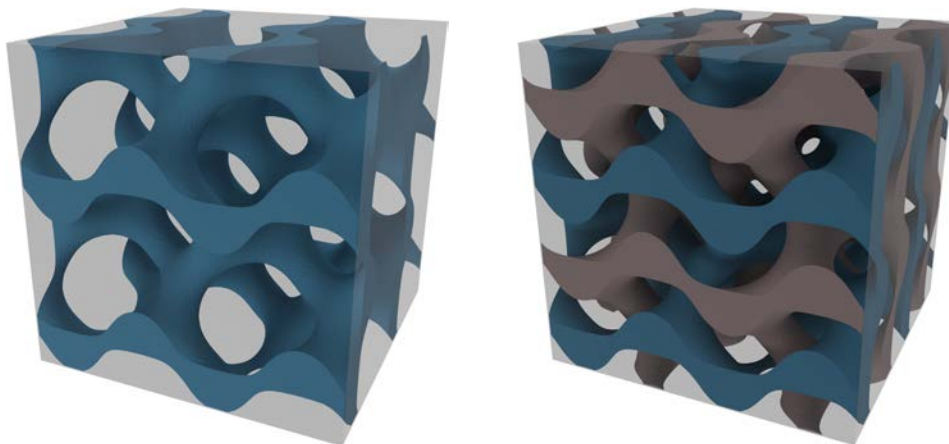
Figure 2.5. The gyroid networks. Left: The single gyroid network. Right: Two enantiomorphic single gyroid networks forming a *double gyroid*. The two networks are separated by by the gyroid surface. All plots are derived from the *level-set* surface G^* with $|t| = 0.9$.

Continuous network phases like the gyroid are particularly interesting for a range of applications as they facilitate three dimensional structuring of functional materials. Selective removal of one of the copolymer blocks is only possible if it is continuous and the etchant can reach all parts of the material. The resulting voided template is only stable if the remaining phase also forms a continuous, self supporting network. Gyroid forming block copolymers are therefore ideal candidates for template based nanostructuring and research on potential applications is ongoing. The motivation for nanostructuring a functional material is often to increase its surface area. This can dramatically enhance the performance of the material as chemical reactions and other diffusion based processes occur predominantly at the material interfaces.[34, 35] Figure 2.6 shows a numerical analysis of the single gyroid surface and volume for different values of t. At $t = 0.9$ the specific surface is calculated for typical polymer unit cell sizes between $10\,\mathrm{nm}$ and $100\,\mathrm{nm}$. The values in the hundreds of $\mathrm{m}^2/\mathrm{cm}^3$ are comparable to figures published for amorphous materials in recent years.[36–38] The advantage of the gyroid is its increased mechanical stability and the uniformity of its pore sizes. It is also worth keeping in mind that compared to single gyroids, double gyroids have twice the surface area per unit cell.
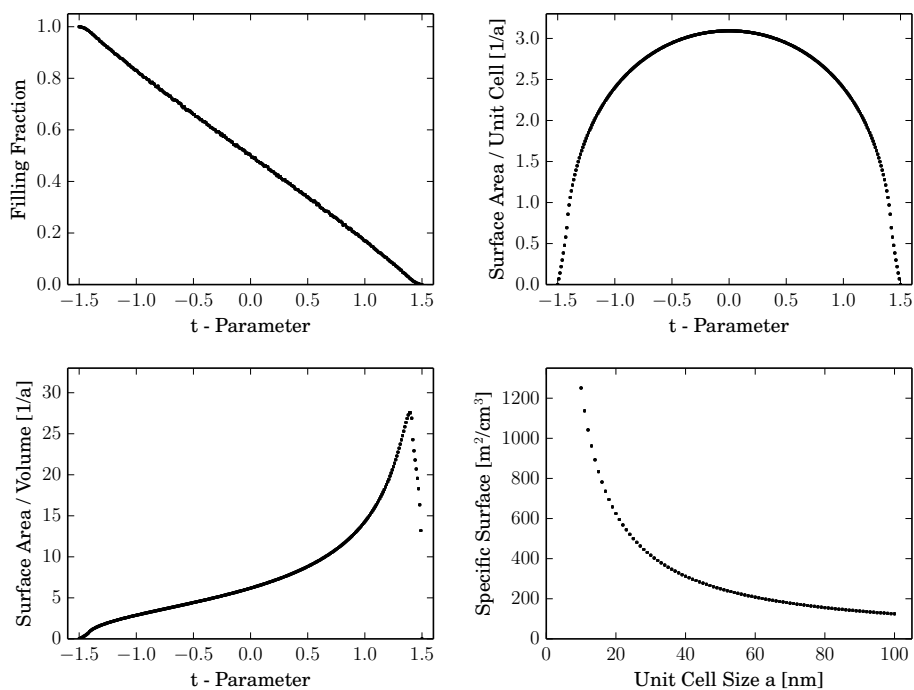
Figure 2.6. Numerical evaluation of single gyroid volume and surface depending on _t_. All data was numerically calculated using the _DiscretizeGraphics_ or _DiscretizeRegion_ functionality of _Wolfram Mathematica 10.0_. Values for $|t| \geq 1.4$ are likely to be inaccurate due to the small strut diameters. Top left: The proportion of the unit cell volume filled by the single gyroid network. Top right: The single gyroid surface area per unit cell. Bottom left: The surface area divided by the filling fraction yields the surface per occupied volume. Bottom right: The specific surface is obtained by dividing the surface per volume by the unit cell size a. Mass-specific surface values can be obtained by dividing through the relevant density value. The plot shows a single gyroid with $t = 0.9$ and unit cell sizes between 10 nm and 100 nm.

2.3 Block Copolymer Annealing

In Section 2.1 the possible equilibrium configurations of various block co-polymers are discussed, without mentioning any of the challenges associated with transforming a disordered polymer melt to its equilibrium state. This process is generally referred to as *annealing*, and the following section describes the underlying principles of several annealing procedures.

2.3.1 Glass Transition in Polymer Melts

The reason annealing procedures are often required to bring a polymer melt to its equilibrium morphology is that the individual chains are only free to move to their energetically most favourable position when the system is above its so-called *glass transition temperature* (T_g).[3] Below this temperature the molecular and structural relaxation time scales are too long for any reasonable experiment, and the material is hard, brittle, and practically solid. Above T_g, on the other hand, it is soft and elastic, and behaves like a viscous liquid. The glass transition temperatures of different polymers vary across a wide range, and in many cases they are significantly higher than room temperature. Glassy and non-glassy states can be observed under ambient conditions in polystyrene ($T_g \approx 95\,^{\circ}\mathrm{C}$ [39]) and polyisoprene (natural rubber, $T_g \approx -70\,^{\circ}\mathrm{C}$ [40]), respectively.

The glass transition temperature can be influenced by mixing additional molecules into the polymer melt.[41–43] So-called plasticisers are widely used in commercial applications of glassy polymers, to increase the flexibility and elasticity of the material at the anticipated operating temperature. Instead of just mixing them into the melt, plasticisers can also be incorporated into the system by copolymerisation, preventing their evaporation and unintended removal. This can be desirable in industrial applications as it enhances the longevity of a product by preserving the properties of its constituent materials. For polymer self-assembly, on the other hand, the fast and complete removal of the plasticiser can be important for further processing.

Despite its obvious symptoms and paramount importance for polymers in all application areas, the glass transition has no strict definition, and to this date there is no theoretical model capable of explaining the underlying

---

[3]This does not always imply microphase separation. Certain polymers can, for example, crystallise at a temperature T_c.

mechanisms to a satisfactory extent.[44] In practice T_g is determined via differential scanning calorimetry: the temperature dependence of a material's specific heat capacity is measured by heating and cooling the sample, and the glass transition can be seen in the resulting graph as an instantaneous increase of the slope. A limitation of this technique is the strong dependence of T_g on the heating and cooling rates,[45] caused by the inherent frequency dependence of the glass transition.[46] Comparable values are typically obtained by extrapolating to the isothermal case. Another approach is the definition of T_g as the temperature at which the material has a viscosity of $10^{12}\,\mathrm{Pa\,s}$. The idea behind this rather arbitrary definition is that — especially in the case of polymers — the glass transition mainly influences the viscosity of the material and with it the time-scale on which internal stresses can decay. The challenge here lies in measuring the huge viscosities of quasi-solid materials. Again, the frequency dependence of the glass transition influences the measurement, and in practice T_g-spectra have to be recorded.[47]

Several attempts have been made to explain the underlying mechanisms of the abrupt and dramatic viscosity change around $T = T_\mathrm{g}$. One of the proposed models is built on the hypothesis that translational polymer movements can only occur cooperatively in two or more regions of a certain volume. It is assumed that the number of possible reorganisations decreases with the temperature, and that therefore the minimum region size for reorganisations increases. In a case where the activation energy increases with the region size this can be shown to lead to a stronger increase in viscosity than predicted by the Arrhenius equation.[44] A weakness of this so-called *entropy model* is that the cooperatively rearranging regions would have to be unrealistically small at $T \geq T_\mathrm{g}$. Also, it implies an underlying phase transition to an obscure *ideal glass* state with zero entropy that has not been described.[44]

Another model is based on the *free volume* of the polymer melt. Here, the assumption is that polymer segments can only move when a sufficiently large unoccupied volume is available. This unoccupied space or free volume originates from the repulsion between individual molecules and the resulting minimal distance between them. It can thus be determined through the density of the melt, which varies by thermal expansion. If the free volume is evenly distributed, the individual portions are too small to accommodate an

entire polymer segment, and relocations are not possible. Thermal motion causes a fluctuation of the individual volumes, and sufficiently sized voids occur with a certain probability.[48] A low density implies a large size of the evenly distributed volumes, and the aforementioned probability will be high. This probability will decrease with increasing density, as collective movements of molecule clusters are now required. A temperature decrease increases the density, causing a reduced mean free volume and thus an increase in the minimal cluster size. T_g is defined as the temperature at which movements are suppressed by a diverging cluster size.

The free volume model offers a possible explanation for the effects plasticisers have on the glass transition temperature.[49] A rigorous definition of the free volume is, however, not possible, and some experiments suggest that the viscosity of a material doesn't only depend on its density.[44]

The entropy model and the free volume model are only two of the various theories that have been suggested as explanations for the observed phenomena. The true nature of the glass transition is subject to current discussion and investigation.[50]

In the context of this dissertation it is important to understand specifically the glass transition behaviour of block copolymers. It is generally assumed that the individual blocks become glassy separately at the T_g of the respective homopolymer. This has been experimentally confirmed for example by Gaur and Wunderlich in styrene – α-methylstyrene copolymers.[51] After careful analysis they conclude that the glass transition of the copolymer blocks occurs across a wider temperature range, but is otherwise identical to the corresponding homopolymer case.

In summary, it can be assumed that a block copolymer melt is free to self-assemble only when its temperature is higher than the highest glass transition temperature T_Gmax of its constituent homopolymers. In practice, a considerably higher temperature is often chosen to ensure the broadened glass transition window is overcome completely and the chains have sufficient mobility.

2.3.2 Thermal Annealing of Block Copolymers

A straightforward way of fulfilling the $T \gg T_\mathrm{Gmax}$ condition is to simply heat the polymer and keep it at the desired temperature for an appropriate amount of time. Key advantages of this approach are the simplicity of the

experimental set-up and it's inherent robustness towards external perturbations. Unsurprisingly, thermal annealing protocols are used in a large number of polymer self-assembly experiments and have been studied in great detail. Alaback *et al.* have used small angle X-ray scattering to monitor the morphology of polystyrene-polybutadiene-polystyrene triblock copolymer films during heating and cooling.[52] In another example, differential scanning calorimetry of polyurethane block copolymers was performed individually and in combination with X-ray scattering to investigate the glass transition and microphase separation at elevated temperatures.[53, 54] The general conclusion of these investigations is that the block copolymers behave as expected and slowly assume their equilibrium morphology as they are heated beyond T_g. This morphology is not affected by the subsequent cooling, and the films can be processed at room temperature.

In order to determine a suitable duration for the annealing step, it can be helpful to estimate the amount of time individual molecules need to move to their energetically most favourable positions. The reptation model of de Gennes predicts a characteristic time scale of $\tau \propto N^3/T$ for translational chain movements.[20] The annealing temperature is often limited by the finite temperature stability of the polymers involved and can't be increased to arbitrary values. Typical decomposition temperatures lie between $200\,°\mathrm{C}$ and $600\,°\mathrm{C}$,[55] and can be catalytically decreased by small solvent molecules or metallic particles.[56] This means that effectively only polymers below a certain chain length can be thermally annealed, as large molecules can't move to their equilibrium positions on reasonable time scales.[57]

Another consequence of an increased temperature is a change in the segregation strength between the different polymer blocks. The temperature depence of the Flory parameter χ implies that temperature changes can have a large impact on the system's vertical position in the phase diagram (see Fig. 2.2). Especially in polymers with large numbers of repeat units, the equilibrium morphology can change with the temperature and the cooling rate at the end of an annealing protocol becomes a very important parameter. Cooling on time scales below the characteristic time τ quenches the system, the polymer is effectively frozen and the current morphology is preserved. Slow cooling rates on the other hand give the system enough time to reorganise as the temperature passes though different regimes. In this case the room temperature material will exhibit the morphology that is dominant

close to T_g.

Thermal annealing offers a robust and reliable way to drive many block copolymer systems to microphase separation. Long range order, on the other hand, is not easily achieved, and more sophisticated adaptations of the technique are required for this. A commonly employed method involves temperature gradients to ensure the microphase separation doesn't nucleate simultaneously across the entire sample. Instead the disorder–order transition gradually moves across the sample and the number of defects is reduced.[58] This is experimentally challenging, as very large temperature gradients have to be created under strong local confinement without overheating the polymer. Also the gradient has to be moved across the sample slowly enough to allow for complete ordering in one pass, dramatically increasing the overall annealing time.

The work presented in Chapter 4 was carried out on samples prepared by thermal annealing. The protocols employed were taken from previous work[32] and alterations were not necessary.

2.3.3 Solvent Vapour Annealing of Block Copolymers

Apart from increasing the temperature T the $T \gg T_\text{Gmax}$ condition can only be satisfied by decreasing T_Gmax. This can be achieved, for example, by introducing solvent molecules to the polymer, effectively plasticising it. This is realised experimentally by exposing polymer films to solvent-rich atmospheres. In the case of good solubility, the solvent molecules will diffuse into the film due to the favourable free energy of mixing.[20] Macroscopically, the copolymer film will become softer and more malleable with increasing solvent content, which is due to the increased mobility of the individual chains.[59] This increased mobility will allow the chains to assume their equilibrium configurations on shorter time scales, provided the solvent content is sufficient to reduce the glass transition temperature well below the film temperature.

In principle, even systems with extremely long chains can be driven to a state of low viscosity by increasing the solvent content. This is, however, not always useful for self-assembly: The solvent molecules screen the interactions between the polymer segments, effectively overriding the driving force of the microphase separation. In the case of a neutral solvent this will decrease the interaction parameter χ and eventually suppress the microphase

separation.[60] If the solvent is preferential towards one of the homopolymer blocks the effective volume fraction of that block will be increased through selective swelling and the equilibrium morphology changes.[61] In practice solvents are unlikely to be perfectly neutral towards all polymer blocks and generally a superposition of both effects is observed. It is worth noting that strongly selective solvents can also increase the segregation strength between the homopolymer blocks.[62]

This means that in comparison to thermal annealing, the solvent based method has a stronger influence on the system's position in the phase space. Especially when a mixture of different solvents is used morphology tuning across wide ranges is possible.[63] This degree of freedom is very useful in many cases, as the synthesis of new block copolymers for different morphologies can be very time consuming[32] and difficult to control precisely. Another key advantage of solvent annealing is the generally increased speed on which the self-assembly occurs.[64] This is partly because rapid temperature changes are experimentally very challenging to realise whereas the diffusion of solvent molecules into and out of thin polymer films is often very fast.

The most basic experimental set-up for solvent vapour annealing is a sealed chamber containing the sample and a small amount of solvent. The solvent will evaporate until the drop, the partial vapour pressure in the atmosphere, and the solvent content in the polymer sample are in thermodynamic equilibrium. Further processing generally requires dry samples, and a solvent removal step is integral to all experimental procedures. This can either be done slowly, by opening a small hole or leak valve through which the solvent can evaporate, or rapidly, by removing the sample from the chamber and exposing it to a dry atmosphere. Such a configuration is suitable for experiments that don't require precise control over the drying step. This step is, however, often a crucial part of the procedure: analogous to the thermal annealing process, the equilibrium morphology of the system depends on the solvent content of the film. Only sufficiently fast solvent removal will preserve the current morphology, and a slow removal can induce further order–order transitions before T_g surpasses the polymer temperature. Furthermore, the drying rate can also have kinetic effects on the orientation of the microphases.[65]

Another way of introducing solvent to the polymer is to keep the sample

in a dry chamber which is purged with a carrier gas with a controlled solvent vapour content. Experimentally, this can be realised by mixing dry and saturated carrier gas in the desired ratio before flushing it through the chamber. The saturation can be achieved by bubbling the respective portion of the dry gas through a large solvent reservoir. This has significant advantages over the previously described method, as the solvent content of the film can be controlled dynamically instead of being tied to the evaporation of a liquid phase in the chamber. With the help of mass flow controllers, the drying rate of the film can be controlled with high precision across a wide range by tuning the flow rate and solvent content of the carrier gas. The experimental set-up used in this work is described in Setion 3.2.2, where a schematic of the assembly is presented.

Challenges with the solvent annealing are firstly the health and safety constraints to the design of experimental equipment: the often volatile and hazardous solvents cannot simply be released to the environment and chambers, bubblers and tubing have to be sealed with great care and connected to appropriate exhaust lines. Secondly, the solvent uptake of the sample depends strongly on the temperatures of the polymer, the carrier gas and the solvent bubbler. It is therefore advisable to operate the set-up in a temperature-controlled environment. Solvent uptake generally goes hand in hand with swelling induced film thickness increases, which means that interferometry can be used to monitor the solvent content of the sample. This is especially elegant given that non-destructive measurements can be conducted with a high sampling rate during the experiments by illuminating the sample through the glass lid of the annealing chamber. A third challenge is the sensitivity of highly mobile polymer films towards interfacial energies. If the polymer–substrate interaction energy is too high, the polymer film will dewet from the substrate, which is highly undesirable in most experiments. Also, further processing steps often rely on a non-preferential substrate wetting of two or more copolymer blocks.[32] In practice, substrate surfaces are often functionalised to obtain a suitable surface energy, circumventing these challenges. The desired surface energy depends on the materials involved as well as the annealing conditions and has to be determined for each experiment.

In summary, solvent vapour annealing is more sensitive to environmental influences than thermal annealing, and a larger number of parameters have

to be controlled precisely. This precise control is crucial for systematic studies, but it can be experimentally very challenging to achieve. The increased sensitivity can, however, be utilised as soon as the respective parameters are controlled to sufficiently narrow tolerances. Microphase separation can be tuned with more degrees of freedom and over wider ranges, and increased long range order can be achieved.[66]

Solvent vapour annealing of a linear triblock copolymer is an important part of the work presented in Chapters 5 and 6. The main goal was to reproducibly fabricate samples for optical characterisations of individual domains. This requires long range order on a $100\,\mu m$ scale, especially for measurements under shallow angles of incidence where the beam footprint is increased.

3

Methods and Techniques

This chapter gives brief descriptions of the various experimental methods and techniques employed during the course of the presented work. The aim is to allow the reader to phenomenologically understand their basic concepts, and to provide references to in-depth information where appropriate.

3.1 Sample Preparation

A large proportion of the experiments presented in this work were carried out on thin polymer films. To allow for comparison between different experiments, great care was taken to prepare samples that were as similar as possible. This section contains details on the protocols for substrate cleaning and functionalisation, as well as surface patterning and film casting.

3.1.1 Substrate Functionalisation

Thin polymer films are strongly influenced by surface effects at the polymer–air and polymer–substrate interfaces. To ensure reproducibility of the experimental work, it is of utmost importance that the substrates are always identical. This was achieved by first cleaning them with a 5 % solution of decon®90[1] in de-ionised water[2] to remove visible contaminations. After the soap treatment, the samples were successively immersed in acetone[3] and iso-propyl alcohol[3], and placed in an ultrasonic bath[4] for 5 minutes, in order to

---

[1]Decon Laboratories Limited, East Sussex
[2]Purified on site with PURELAB® Ultra, ELGA LabWater, Buckinghamshire
[3]Analytical Reagent Grade, Fischer Scientific, Leicestershire
[4]FB 15050, Fischer Scientific, Leicestershire

remove remaining surfactants.

To remove organic residue from the substrate and render the surface hydrophilic, a *piranha etch* was performed. For this purpose, the samples were first sonicated in de-ionised water, and then immersed in a 3:1 mixture of 98 % sulphuric acid[5] (H_2SO_4) and 30 % hydrogen peroxide[6](H_2O_2). Heating the solution to $80\,°C$ turns it into a powerful oxidising agent, capable of dissolving almost all organic matter. After approximately 15 minutes of immersion, the samples were removed from the solution and thoroughly rinsed and sonicated in de-ionised water. The hydrophilicity of a cleaned substrate is caused by the OH-groups the solution leaves behind on its surface, as well as the absence of organic contaminants.[67] The piranha solution has to be handled with great care, as it reacts highly exothermically with organic matter. Especially with organic solvents, this can cause violent reactions and explosions.[67]

In a third step, the surface energy of the samples was modified to prevent preferential wetting of individual copolymer blocks, which can cause a continuous non-porous layer of one of the polymer blocks at the substrate interface. This in turn prevents further processing of films voided by selective polymer removal: Either the polymer film will no longer be attached to the substrate after selective dissolution of the interfacial layer, or the electrodeposition from the substrate into the polymer template is prevented by an insulating polymer layer on the conductive substrate.[32]

The surface treatment used in this work relies on the formation of a self-assembled organic monolayer. The samples are immersed in a 0.2 % solution of trichloro(octyl)silane[7] (OTS) in anhydrous cyclohexane[8] for 15 seconds. Upon removal from the solution, the sample was immediately blow-dried with compressed nitrogen gas from the in-house line. The aim here was to swiftly, but carefully, blow the remaining solvent off the substrate before it evaporates, to prevent further silane deposition in drying rings. OTS molecules consist of one silicon atom in the centre of a tetrahedral geometry. The substituents are three chlorine atoms, and a long hydrocarbon chain. The first step of the silanisation process is the hydrolysis of the chlorine atoms in the vicinity of the surface OH-groups of the substrate. The res-

---

[5]Analytical Reagent Grade, VWR Chemicals, Leicestershire

[6]Laboratory Reagent Grade, Fischer Scientific, Leicestershire

[7]97 %, Sigma Aldrich, Dorset

[8]99.5 %, Sigma Aldrich, Dorset

ulting silanetriol is then attached to the surface by hydrogen bonding, and finally forms covalent Si–O–Si bonds with the substrate and neighbouring silane molecules.[68] The biggest challenge associated with this procedure arises from the fact that it is very sensitive to the amount of water present: The reaction can't proceed without water, and too little water will cause incomplete substrate coverage. Too much water, on the other hand, will cause uncontrolled polymerisation of the silane in solution.[68]

3.1.2 Spin Coating

The majority of the experimental work presented here was carried out with 0.7–3 µm thick polymer films. A simple and widely used technique for the fabrication of thin films is the *spin-coating* procedure. A drop of polymer solution is placed on a substrate, which is held in place by a vacuum chuck. The entire assembly is accelerated to a certain angular velocity. The interplay of centrifugal and adhesion forces causes a radial shear flow, spreading the solution across the sample. Excess solution is drained off the substrate edge, and eventually a film of homogeneous thickness is formed. The film thickness depends on the acceleration rate, the final angular velocity and the viscosity of the solution. The spin-coater used in this study[9] is continuously purged with nitrogen gas during operation. This gas flow, and the sample rotation, cause rapid solvent evaporation, decreasing the thickness of the film.

Apart from film thickening effects at the substrate edges, spin-coating generally results in very smooth films of uniform thickness. The procedure is highly reproducible, and film defects generally only occur when substrate or solution are contaminated. The thickness of the obtained films depends on the spin speed and acceleration, and in particular on the viscosity of the polymer solution.[69] Excess polymer solution is centrifuged off the sample, meaning the deposited amount of material has little influence on the final film thickness, provided the substrate can be covered in a sufficiently thick layer.[69] More comprehensive information on the spin coating procedure has been collated, for example, by C. J. Lawrence[69] and K. Norrman *et al.*[70]

---

[9]WS-650MZ-23NPP, Laurell Technologies Corporation, North Wales

3.1.3 Photolithography

An optional step after the surface functionalisation is the lithographical patterning of the substrate. Photolithography is a *top-down* microfabrication technique, widely used, for example, in the semiconductor industry.[71]

Generally, a substrate is spin-coated with a thin layer of photosensitive polymer. As soon as the film is dry, it is illuminated through a patterned photomask. In this work, a *mask aligner* is used for this process in contact mode. Mask aligners usually combine an optical microscope with a high power large area illumination lamp, and a mechanism to press the sample against the photomask. This is important, as the light output of the lamp is not collimated and parallax errors are proportional to the distance between sample and mask. With a collimated light source the sample can be positioned some distance from the mask, and the pattern can be magnified or miniaturised with the help of lenses.[72] The illumination wavelength, intensity and duration depend on the layer thickness and material properties of the photosensitive polymer. In some cases a *post-bake* is required after illumination, before the sample is immersed into a liquid developer. Here, either the illuminated or non-illuminated parts of the polymer film are dissolved and removed, leaving behind a positive or negative image of the illumination mask.

In Chapter 4, photolithography is used to locally insulate a conducting substrate. The block copolymer is deployed on top of the patterned substrate and processed as usual. This means that in a subsequent electrochemical deposition step a nanoporous template is filled in a microstructured pattern, creating a hierarchically structured material.

In-depth information on photolithogrpahy can be found, for example, in a book published by H. J. Levinson.[73]

3.2 Sample Processing

Once the thin polymer film is prepared with the desired properties, the sample undergoes various further processing steps. First, the polymer has to be annealed to assume its equilibrium morphology, then a voided template is formed by selectively removing one of the copolymer blocks. The template can then be filled with a functional material, and finally this material can be freed by removing the polymer template. This section gives descriptions

of the general methods used for these processes that will be referred to in the following chapters, where the detailed parameters are listed.

3.2.1 Thermal Annealing

Thermal annealing is a straightforward method of facilitating self-assembly in a polymer sample by heating it above its glass transition temperature T_g. Despite the inherent simplicity of the method, some care should be taken when conducting experiments, to ensure precise control and good reproducibility.

In this work, a vacuum oven[10] was used in combination with a custom made brass chamber[32] inside the oven's vacuum chamber. The brass chamber contains heating cartridges and temperature sensors, which are connected to an external temperature controller[11] via a vacuum feed-through. The brass body provides a large thermal mass that is in direct contact with the sample. This significantly improves the temperature control compared to a vacuum oven alone, where the temperature sensor is often placed in a corner of a large chamber, and effectively measures the temperature of the surrounding gas. Especially in the case of an evacuated chamber, the thermal mass of the gas will be very low compared to the sensor, and large time lags in temperature sensing occur.

In a typical experiment, the samples were first placed in the brass chamber, and the vacuum oven was closed. Subsequently, the chamber was evacuated and purged with nitrogen gas several times to remove all oxygen from the system. For the heating step, the chamber was constantly connected to the vacuum pump, to make sure it stays evacuated and residual solvent is swiftly removed from the sample and the chamber. Now the predefined heating protocol, consisting of a temperature ramp and a dwell step, is started. At the end of the dwell step, the heater is automatically turned off, and the oven and sample slowly cool down to room temperature. The sample can also be quenched at the end of the dwell step by opening the oven, and swiftly placing the hot sample on a cool piece of metal with sufficient thermal mass. This brings the sample close to room temperature on time scales of tens of seconds, and it can be assumed that the high temperature morphology is preserved.

---

[10]FP 53, Binder GmbH, Tuttlingen (Germany)
[11]CAL 9400, CAL Controls, Hertefordshire
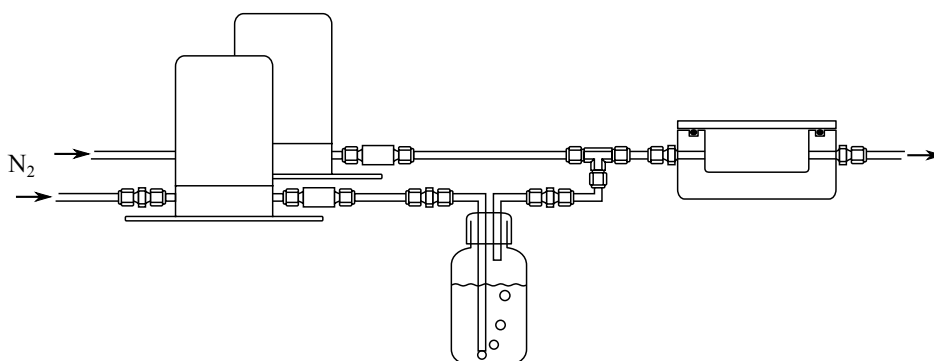
Figure 3.1. Schematic of a set-up for dynamic solvent vapour annealing. The annealing chamber on the right is purged with a mixture of dry and solvent-rich nitrogen gas. The solvent content of the gas can be adjusted by individually regulating the flow rate in both channels, for example with mass flow controllers (depicted on the left).

3.2.2 Solvent Vapour Annealing

Solvent vapour annealing was conducted in a home built experimental set-up. The sample was placed in a small, sealed chamber and nitrogen gas with a controlled solvent vapour content was flushed through the chamber. The gas flow is created by combining two nitrogen streams, one consisting of dry gas, while the other one is bubbled through a large solvent reservoir.

The crucial parameters here are the the temperatures of the sample, the carrier gas and the solvent reservoir, as well as the solvent content and flow rate of the gas. The sample temperature is kept at a constant value by placing the substrate directly onto a copper base that is temperature controlled with a resistance thermometer and a Peltier element. To prevent heating or cooling through ambient air, the rest of the chamber is made from PFTE, which exhibits excellent solvent resistance combined with a low thermal conductivity. The solvent reservoir is a carefully sealed bottle with a gas inlet and outlet connected to bubbling pipes. The bottle is submerged in a temperature controlled water bath, along with the directly connected metal pipework. To ensure a uniform temperature in the entire bath, a pump is used to circulate the water. This pump also facilitates the connection of an external water cycle to the bath, which is utilised to keep the gas lines between solvent reservoir and annealing chamber at a constant temperature.

By individually controlling the flow rates in the dry and the solvent-saturated gas lines, the flow rate and solvent content of the combined line

can be set to a wide range of values. Precise and reliable control is facilitated by mass flow regulators[12], which are connected to a controller and power supply unit[13]. This controller is connected to a computer via an RS232 connection, enabling automated experimentation. For this purpose a simple python program based on the *pyserial*[74] library was written. The program periodically sends updated flow rate set-points to the controller, following a predefined time profile.

This is firstly very convenient, as it removes the requirement for the manual updating of the parameters, and the individual flow rates can be automatically calculated from the desired total flow rate and concentration values. Moreover, it also facilitates experiments that would be highly impractical in manual operation, such as multi-hour profiles with gradually changing flow and/or concentration, or abrupt changes that would require new data input each second. Finally, it increases the precision of the entire experiment, and logs not only the set-points, but also the actual values measured by the mass flow controllers. Deviations between set-point and actual value can occur through either external pressure loss or internal pressure build-up that are often not visible without the software.

In the course of the presented work, many experiments were conducted with chloroform[14] and other hazardous solvents, such as tetrahydrofuran[14] or toluene[14]. As the set-up was used outside a fume hood, these solvents should not leak out of the system under any circumstances. Careful sealing of the entire set-up, and the exclusive use of solvent resistant materials is thus of paramount importance. 1/4" stainless steel tubing[15] was used for all gas lines in the water bath, connecting the mass flow controllers, the solvent reservoir and the T-junction where the dry and saturated gasses are mixed. The annealing chamber was connected to this junction and the house exhaust with flexible PFA tubing[16]. A particle filter[17] was installed in the nitrogen supply line before the mass flow controllers, to protect them from mechanical damage. Poppet valves[18] were connected directly to the outlet of the mass flow controllers, to prevent damage caused by back-flow

---

[12]1179A Mass-Flo® (100 sccm), MKS instruments Ltd., Cheshire East

[13]PR4000B, MKS instruments Ltd., Cheshire East

[14]Analytical Reagent Grade, Fischer Scientific, Leicestershire

[15]instrumentation grade, swagelok® Company, London

[16]swagelok® Company, London

[17]7 µm pore size, swagelok® Company, London

[18]PTFE sealed, swagelok® Company, London

or diffusion of solvent molecules. Both gas lines also have solvent resistant quarter turn plug valves[19] for manual shut-off.

The gas inlet and outlet of the custom made annealing chamber were threaded, to seal tightly with available swagelok® connectors. Viton® o-rings[20] were used to create a solvent resistant seal between the PTFE chamber and the copper base, as well as the chamber and the glass lid. The bubbling unit was also custom made, and consisted of a modified GL45 screw cap[21] and a 100 ml bottle with a GL45 thread[22]. A hole was punched through the screw cap and its PTFE-coated silicone rubber seal, to accommodate a welded assembly of two 1/4" stainless steel tubes axially passing through a brass cylinder. This feedthrough was sealed with viton® and PTFE seals, and a retainer nut was screwed onto the brass cylinder to press the seals tightly against the cap surface. The length of the protruding tube ends was such that the incoming gas was released at the bottom of the bottle, while the gas outlet was at the very top. This ensured maximum exposure of the gas to the solvent, while preventing the displacement of liquid solvent.

The glass lid of the annealing chamber facilitates *in-situ* optical examination of the sample with a long working distance microscope. Another possibility is to track the solvent content of the polymer film by monitoring it's thickness through interferometry.

3.2.3   Selective Polymer Removal

In order to use the annealed block copolymer films as templates for the deposition of other materials, one of the polymer blocks has to be removed without affecting the structural stability of the remaining polymer.

The block copolymer used in Chapter 4 consisted of poly(lactic acid) and polystyrene. The poly(lactic acid) was removed by immersing the sample in a 0.1 molar solution of sodium hydroxide in a 1:1 mixture by volume of water and methanol.[32]

A linear triblock of polyisoprene, polystyrene and polyethylene oxide was examined in Chapter 6. Here, the annealed films were first exposed to ultraviolet light[23] for approximately 30 minutes. This step cross-linked

---

[19]swagelok® Company, London
[20]Polar Bearings Limited, Cambridge
[21]Premium Cap, Duran Group, Wertheim/Main (Germany)
[22]21 801 24 5, Duran Group, Wertheim/Main (Germany)
[23]VL-100.C (254 nm, 100 W), VWR International, Leicestershire
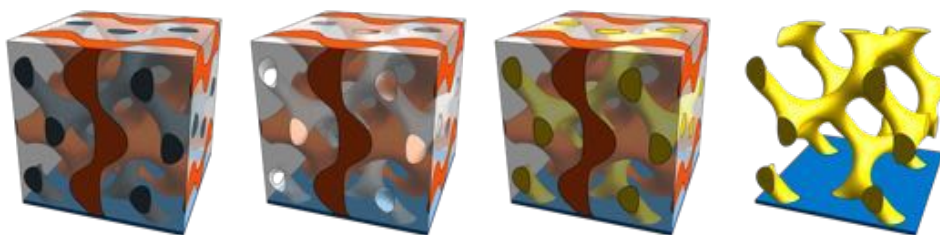
Figure 3.2. Illustration of the templated fabrication of gold gyroids. The images show a section of a self-assembled triblock copolymer in the gyroid phase (left). In the first step the isoprene block (grey) is selectively removed, leaving behind a voided template. The connectivity of these channels to the conducting substrate allows the electrochemical backfilling of the voids. Finally, the styrene (transparent) and ethylene oxide (orange) blocks are removed by oxygen plasma etching, yielding a free-standing gold gyroid (right).

the polystyrene block,[75] while degrading the polyisoprene block.[76] The sample was then submerged in ethanol[24] for a further 30 minutes, which is a solvent for the polyethylene oxide and the polyisoprene, but not for the polystyrene. The polyethylene oxide chains are still intact at this point, and remain attached to the cross-linked polystyrene blocks, which means that they are only temporarily dissolved in the ethanol. The polyisoprene chains, on the other hand, are broken-up during the UV exposure, and are thus washed out by the ethanol. A diagram on this procedure is shown in Figure 3.2

3.2.4   Templated Electroplating

Electrochemical deposition is a convenient method of replicating the previously removed polymer block into a different material by filling the voided template. For this technique, two conducting electrodes have to be immersed into an ionic solution. When a voltage is applied between the two electrodes, positively charged ions in the solution start moving towards the negative electrode (cathode), and negatively charged ions move towards the positive electrode (anode). At the cathode, the ions will be *reduced* by gaining electrons, and at the anode, the ions will be *oxidised* by losing electrons. In a typical experiment one of these processes will lead to the deposition of a solid film on the surface of the respective electrode. This electrode is referred to as the *working electrode*, and the other electrode is the *counter electrode*. As long as the deposited film is conductive, the deposition can

---

[24]Analytical Reagent Grade, Fisher Scientific, Leicestershire

continue, gradually increasing the film thickness. In the absence of parasitic reactions, such as electrolytic solvent decomposition, the amount of material deposited is proportional to the charge flowing between the two electrodes. This means that the deposition rate can be monitored and controlled via the current and voltage between the electrodes.

For many applications a so-called *reference electrode* is used to precisely determine the absolute potential of the working electrode. This is necessary, as voltage measurements can only ever reveal the difference between two potentials. The reference electrode is typically enclosed in a glass vial containing a buffer solution, to keep it at a constant potential. Electrical contact to the electroplating bath is established through a porous ceramic or metal oxide plug, which limits the liquid passage to minute amounts, preventing depletion of the buffer solution. The absolute potentials of the other electrodes can be determined this way by comparing them to the known reference potential.

Conducting substrates are required for the templated electroplating, as the deposition only occurs on surfaces that are in electrical contact with the working electrode. For optical applications, transparent substrates are often required, and soda lime glass with a thin layer of fluorine doped tin oxide[25] was chosen for the experiments discussed here. Since the polymer templates used in this work aren't electrically conducting, they have to be porous across the entire film to enable direct contact between the plating solution and the substrate surface. A further challenge is to ensure that the nano-channels of the template are fully infiltrated by the often water based ionic solutions despite their high surface tension. This is commonly achieved by wetting the template with a low surface energy solvent, such as methanol, before immersing it in the electroplating bath. Entropic forces ensure swift mixing of the two liquid phases, and the ionic solution can infiltrate the entire template.

More information on the Electrodeposition of metals can be found in a book published by Y. D. Gamburg and D. Zangari.[77]

---

[25]TCO22-15, Solaronix SA, Aubonne (Switzerland)

3.2.5 Template Removal

In a successful electroplating step a nanoporous conducting material is created inside a polymer matrix. The key advantage associated with nanoporosity — the increased surface area — can only be utilised when the interfaces are not covered by the template.. For many applications it is thus essential to remove the template to obtain a free standing material. This process has to be adapted to the respective materials to ensure that the template can be completely removed without affecting the deposited material.

For the experiments presented in Chapters 6 and 5 the polystyrene–polyethylene oxide templates were filled with gold, making the task of finding a suitable selective etchant rather simple. Due to the excellent corrosion resistance of gold, the samples were placed in an oxygen plasma etcher[26] for 30 minutes. The chamber of the plasma etcher was evacuated, before a low pressure oxygen atmosphere was created by introducing a constant flow of oxygen gas. An electric generator was activated to create a strong AC electric field between two large area electrodes, typically placed at the top and the bottom of the chamber. This ionises the gas molecules in the entire chamber, creating a plasma with a characteristic white glow. The ions are accelerated by the electric field, and the sample is exposed to a large influx of oxygen ions which will gradually etch away any organic compounds. The polymer molecules are thus decomposed and flushed into the chamber exhaust by the constant gas flow. The nanostructured gold and the substrate are not affected by this procedure, resulting in the desired free-standing material.

The work presented in Chapter 4 comprised a less straightforward task, as the deposited material was a conducting polymer. In this case, a selective solvent had to be identified through careful experimentation. This proved to be especially challenging, since the nanostructured nature of the deposited polymer made it more susceptible to dissolution and deformation than the bulk material.[78]

---

[26]Femto, Diener electronic GmbH + Co. KG, Ebhausen, Germany

3.3 Characterisation Techniques

A number of characterisation techniques were employed during the course of this work for various purposes. The most important ones are briefly explained here, with more specific descriptions following in the respective chapters.

3.3.1 Differential Scanning Calorimetry

The glass transition behaviour of polymers can be examined with a technique called differential scanning calorimetry (DSC). Here, the glass transition can be detected in the form of a change in the derivative of the specific heat of the polymer upon change of the temperature.

For a DSC measurement, several micrograms of the polymer are weighed into a small aluminium dish. The dish is then closed with a lid and sealed tightly. An empty dish of the same material, size and shape is prepared in the same way, and both sealed dishes are placed in small identical chambers in the calorimeter. The two chambers are now simultaneously cooled and heated through a predefined temperature range several times. The heating and cooling rates are controlled to narrow tolerances, and the heat capacity is measured continuously throughout the procedure. The precision of this measurement is greatly enhanced by the empty reference dish, as it facilitates the direct subtraction of the influence of the sample holder.

The glass transition temperature can be extracted from the data by careful analysis of the slope of the heat capacity graph. Other phenomena can also be analysed via DSC. Crystal growth and melting processes, for example, are directly visible in the data in the form of peaks and dips.

3.3.2 Interference Based Thickness Tracking

The kinetics of the swelling and de-swelling that occurs in polymer films during solvent uptake or drying can be measured via the film thickness. The thickness measurements have to be fast and non-destructive to facilitate time-dependent data acquisition. Another important criterion is the possibility to use a probe outside the annealing chamber. Otherwise, complex feed through ports would be necessary, and measurement induced perturbations could occur.
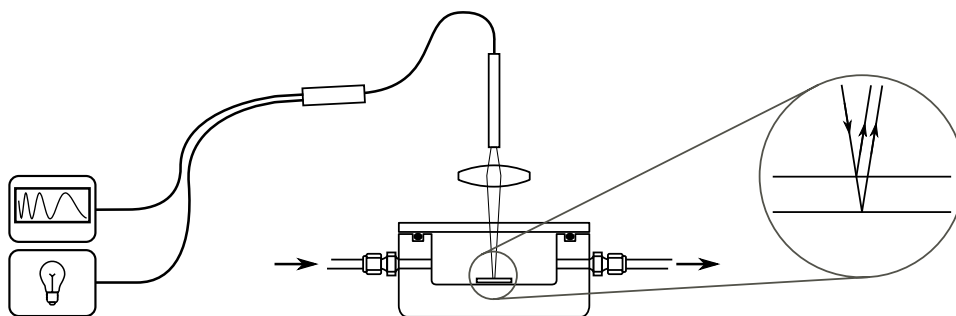
Figure 3.3. Schematic of the interferometry set-up. The solvent content of a polymer film can be determined by measuring the film thickness before and during solvent exposure. The transparent lid of the annealing chamber allows *in situ* interferometry measurements, and a bifurcated optical fibre can be used for the sample illumination and the detection of the reflected signal.

All these criteria can be fulfilled by an interferometric set-up. Here, a bifurcated optical fibre[27] is connected to a light source[28], the spectrometer[29] and the probe. A bifurcated fibre consists of a bundle of individual fibres that are all combined at the probe end. This bundle is split into two separate bundles with independent ends, which means that the sample illumination can be provided by one set of fibres and the reflected signal can be transmitted to the detection apparatus by another set. Normal incidence measurements are thus possible without a complex beam-splitting assembly.

The sample is illuminated with an unfiltered halogen lamp, and incoming light is partially reflected and partially transmitted at the surface of the polymer film. A proportion of the transmitted light is then reflected off the substrate surface, and the interference between these two reflected beams can be measured with a spectrometer. Constructive interference occurs, when the

$$2 \cdot t \cdot n = k \cdot \lambda \tag{3.1}$$

condition is fulfilled. Here, t and n are the thickness and the refractive index of the film, k is an integer number, and λ is the wavelength of the incident light. The detection of a single maximum is not enough to determine t, as the order k of the maximum is generally unknown. As soon as two adjacent maxima are detected, this unknown can be eliminated and the thickness can be calculated. To increase the measurement precision, multiple maxima and

---

[27]R400-7-SR, Ocean Optics Inc., Oxford
[28]HL-2000-FHSA, Ocean Optics Inc., Oxford
[29]USB4000, Ocean Optics Inc., Oxford

minima can be taken into consideration through a simple fit. This can be done by rearranging Equation 3.1 to

$$k = 2 \cdot t \cdot n \cdot 1/\lambda. \tag{3.2}$$

The k values can be set to an arbitrary sequence of numbers, as long as their spacing is one. The thickness can now be extracted from the slope of a straight line fitted through the inverse wavelength values.

In practice, it may be advisable to add a collimating lens to the illumination and detection fibre to maximise the light intensity at the spectrometer. This is especially useful for measurements during solvent annealing, where long working distances are often necessary. In this context it is also important to carefully measure the background and reference signal, as there are often additional reflections from the surfaces of the lens and the glass cover of the annealing chamber.

In the course of this work, a python program based on the *oceanoptics* python module[79] was developed, to facilitate automated measurements and live thickness fitting. Dispersion or solvent induced changes of the polymer refractive index were neglected. This implies that values obtained at large swelling ratios are likely to be inaccurate. This is acceptable for experiments where the aim is to compare two different processes with identical materials, rather than to determine the absolute film thickness values.

3.3.3   Scanning Electron Microscopy

The structures formed by polymer self-assembly typically have feature sizes on the nanometre length scale. The resolution of optical microscopy is limited to roughly the wavelength of visible light, and is generally unsuitable for observing sub-micrometre features. Electron microscopy, on the other hand, probes the sample at much lower wavelengths, and can resolve the unit cells of all block copolymers used in this study.

In a scanning electron microscope (SEM) the sample is placed in a vacuum chamber, and probed by a collimated beam of electrons with energies in the kilovolt range. At the surface of the sample, the electrons first penetrate the material, and eventually collide with atoms near its surface. This causes a variety of effects, such as the ejection of so-called secondary electrons from the exposed atoms and subsequent emission of X-ray radiation,

or the backscattering of primary electrons. These effects can be detected independently from each other, and allow the combination of different characterisation techniques. The most commonly used technique relies on the detection of secondary electrons, and was also utilised in this study.

Each secondary electron that is emitted in the sample has a certain probability of escaping the sample before being decelerated by collisions with surrounding atoms. This probability depends on a number of material parameters, as well as its initial velocity and distance from the surface. When a large number of incoming primary electrons is considered, this means that the number of emitted secondary electrons depends on the topography of the impact location, because the volume of a "hill" is on average closer to the nearest surface than the equivalent volume under a "valley". In practise, it is impossible to determine the exact spatial origin of the secondary electrons, and instead they are counted globally. This means that in order to gain localised topography information, the sample has to be rastered with a focused electron beam. The number of detected secondary electrons per raster point is then translated into an intensity value, and the scanned sample area can be displayed as a grey scale image. These images provide accurate representations of the sample topography in the plane perpendicular to the incident electron beam. Height information can only be seen indirectly through depth of field effects.

In practice, scanning electron microscopy facilitates swift sample inspection and two-dimensional measurements on nanometre length scales. Film thicknesses can be determined by first cleaving the film, and then imaging the cross-section. Three-dimensional information, on the other hand, can not be directly extracted from the images. Also, the technique is limited to conducting samples, as the constant influx of electrons would otherwise cause a charge build-up that would deflect subsequent electrons, distorting the measurement. This constraint can be circumvented by covering the sample in a thin layer of conducting material, for example through sputter-coating. The layer thickness has to be sufficient to provide enough conductivity, but should otherwise be limited to a minimum to prevent a masking of sample features.

Comprehensive and exhaustive information on scanning electron microscopy has been collated by J. Goldstein *et al.*[80]

3.3.4 Atomic Force Microscopy

Atomic force microscopy is another useful high-resolution sample characterisation technique. Here, the sample surface is mechanically scanned with a sharp probe, and local height information is collated into a topography map of the scanned area. The resolution of this map is typically limited by the finite dimensions of the probe tip, as high precision scanning is readily achieved with piezoelectric elements. In practice, lateral resolutions in the nanometre and sub-nanometre range are possible with standard instruments. The height resolution depends on the nature of the surface probe and the operation mode of the device, and is typically in the angstrom or sub-angstrom range.

The most basic operation mode is the so-called *contact mode*. Here, a flexible horizontal cantilever is dragged across the sample surface. A sharp tip protrudes from the free end of the cantilever, and is in constant contact with the sample. As the tip is dragged across an elevated feature, the cantilever is bent upwards. This deflection can be detected with high precision, and an electronic feed-back loop is used to adjust the height of the cantilever, keeping the deflection at a constant value. The cantilever thus scans the sample with a constant distance to its surface, so that the sample topography can be directly extracted from the cantilever height map.

The instrument can also be operated in the *non-contact-mode*, to prevent abrasion damage to the tip or the sample. In this mode, the cantilever is driven to oscillate at its resonance frequency by a piezoelectric element. When the tip is in close proximity to the sample, there will be attractive van der Waals forces, which dampen the oscillations of the cantilever. This can be detected as a change in the resonance frequency, and analogous to the contact mode a feed-back loop can be used to keep the cantilever at a constant distance from the sample. In a damped oscillation there is always a phase difference between the driving force and the oscillation. This phase difference can also be recorded for each sampling point, and the resulting phase map can be used to locally evaluate the magnitude of the interaction between sample and tip. The non-contact mode offers superior sensitivity, and thus increased resolution compared to the contact mode. The drawback of this is that measurements have to be conducted under vacuum, to minimise environmental perturbations.

The operation mode used in this study is somewhat of a hybrid between

the contact mode and the non-contact mode. In the so-called *tapping mode* the cantilever also oscillates close to its resonance when hovering over the sample. The amplitude of these oscillations as well as the cantilever-sample distance are much larger than in in the non-contact mode. This implies that the attractive interaction only occurs once per oscillation cycle, when the cantilever reaches maximum downward deflection. The cantilever-sample distance is kept constant by fixing the oscillation amplitude. The tapping mode is generally less sensitive to environmental influences than the non-contact mode, and facilitates high precision measurements under ambient conditions.

Atomic force microscopy is a useful technique for the evaluation of self-assembled polymer films. Its main advantage compared to electron microscopy is its ability to characterise the surface of non-voided films. This is achieved through a carefully adjusted phase measurement, where the different polymer–tip interactions of the individual copolymer blocks facilitate a 2D morphology mapping. Other advantages are that the samples don't have to be conducting or in a vacuum chamber, and that for voided templates a shallow three dimensional image can be obtained.

More information on atomic force microscopy can be found in a book recently published by Greg Haugstad.[81]

3.3.5 X-Ray Scattering

A common technique for three-dimensional morphology analysis is based on the scattering of high energy photons.

X-ray radiation interacts mainly with the electrons of the irradiated matter. The probability for elastic and coherent interaction is often sufficient to facilitate measurable interference effects between the scattered photons. Prerequisites for this are the coherence of the incident radiation, and a periodically ordered array of scatterers. In practice, the interaction between X-rays and matter is often very weak, and a large number of ordered scatterers is required to produce a detectable signal. The advantage of the weak interaction is the fact that the attenuation of the incident beam is also very low, which facilitates three dimensional measurements in thick samples. This makes X-ray scattering a very suitable technique for the characterisation of crystals, where all atoms are arranged in a periodic lattice.

Bragg's Law defines the

$$2 \cdot d \cdot \sin \theta = k \cdot \lambda \tag{3.3}$$

condition for interference maxima.[82] Here, d is the distance between two planes in the crystal lattice, θ is the X-ray angle of incidence, k is an integer number and λ is the X-ray wavelength.

In poly-crystalline samples the orientations of the individual crystallites are typically randomly distributed and all angles of incidence can be probed in a single measurement. The resulting diffraction pattern exhibits a maximum for each characteristic unit cell dimension under an angle of $2 \cdot \theta$ with respect to the incoming beam. As the X-rays are scattered in all directions, the diffraction pattern is symmetrical under rotation around the wave vector of the incoming beam. This rotational symmetry is broken when the crystallites in the sample exhibit a preferential orientation, and segmented rings or discrete spots can be measured.

Mathematically, the scattering pattern corresponds to the Fourier transform of the sample's electron density. The full Fourier transform would — in theory — facilitate the complete reconstruction of the three-dimensional structure, provided the full scattering cross-section of all atoms is known. In practice, detectors only record the intensity values, and the phase information is lost. This means that the sample morphology is typically determined iteratively, by comparing the measured scattering pattern to the Fourier transform of a model structure.

As already indicated by Ludwik Leibler in 1980, X-ray scattering can be used to probe the Fourier transform $\vec{S}(\vec{q})$ of the density–density correlation function of a block copolymer system.[21] He explains that this is only viable when the different homopolymers have significantly different electron densities, which typically corresponds to a large χ-value. The periodic variations of the electron density are equivalent to an ordered array of scatterers in this case, and a diffraction pattern can be observed. This diffraction pattern allows the evaluation of the three-dimensional morphology of self assembling block copolymer systems, which is often highly useful for related experiments.

An important factor for the design of experiments is the geometry of the measurement set-up. The first order maximum for a 40 nm structure probed

by 10 keV X-rays ($\lambda = 1.24$ Å) occurs under an angle of $2 \cdot \theta = 0.178°$. As the transmitted primary beam is several orders of magnitude more intense than typical scattering signals, it is often prevented from reaching the sensitive detectors by obstructing the beam path with a beamstop (often a small piece of lead). Shallow scattering angles thus require sample-to-detector distances on the order of several metres to ensure that the scattered signal is not affected by the beamstop.

Another factor is the required exposure time. Especially materials with low electron density contrast produce very weak scattering signals. When a conventional X-ray tube is used for imaging, it can be necessary to integrate the detected signal over several hours. This is, however, only viable if the signal is significantly stronger than the noise level of the detector, and if the sample is stable over the entire measurement time. All other cases require a higher incident beam intensity, which can be provided by synchrotron light sources. Here, the integration times can typically be reduced to several seconds, and the signal to noise ratio is boosted significantly. This facilitates dynamic measurements for a variety of systems, and, for example, the self-assembly of block copolymers can be studied *in situ*.

Aside from potential beam damage through over-exposure, X-ray scattering is a non-destructive morphology characterisation technique for polymer samples. It is a crucial tool for self-assembly experiments, as it allows three-dimensional morphology analysis on nanometre and sub-nanometre length scales. In combination with a synchrotron light source, this can be used to investigate the dynamics of the microphase separation under various conditions.

L. A. Feigin and D. I. Svergun have published a book with useful in-depth information on small-angle scattering.[83]

4

Hierarchical Structuring of Conjugated Polymers

This chapter revolves around the nanostructuring of soft functional materials via polymeric templates. A processing route based on orthogonal solvents is presented that facilitates the selective removal of the templates, and thus yields free-standing nanoporous material. Films of electrochromic conjugated polymers are fabricated, to demonstrate the enhanced performance of nanostructured materials. Finally, macroscopic functional devices with hierarchical structures are fabricated, to investigate the compatibility of polymer self-assembly with conventional top-down fabrication techniques.

4.1   Introduction

When polymers have hybridised sp^2 orbitals along their backbones, they can form a conjugated system with de-localised electrons, rendering the material electrically conductive.[85] Conductive polymers are interesting candidates for a variety of applications in the fields of printed electronics,[86] organic

---

solar cells,[87] batteries,[88] and display technologies.[89] The advantages over conventional materials lie mainly in their mechanical flexibility and their viability for novel fabrication pathways. These advantages are, however, often not enough to counterbalance their reduced performance,[90] and the adaptation in commercial applications is relatively slow.

Particularly for processes based on ionic diffusion, such as coloration in displays or charge intercalation in batteries, the achievable performance is limited by the low ion mobility in bulk materials.[91] Performance enhancements can be achieved, for example, by nanostructuring the material to increase the interfacial area and reduce the required diffusion distances.[92–94]

Nanostructured soft materials are more susceptible to mechanical deformation than their bulk counterparts, especially in the presence of plasticising molecules.[78] Mechanical stability is, however, a crucial prerequisite for practical applications, and among the nanostructured materials, 3D architectures are the most robust.[95, 96] Another desirable property is the interconnectivity of both the material network and its pores. This ensures fast transport of charge carriers in either phase, as well as the accessibility of the complete surface area.

The double gyroid morphology introduced in Section 2.2 is therefore a very promising candidate for a stable, performance-enhancing structure, and the self-supporting nature of its constituent phases facilitates a variety of fabrication pathways. Double gyroid structured polymer templates with uniform strut diameters and pore sizes can be created on macroscopic scales via self-assembly.[97, 98]

The template-based fabrication of nanostructured materials is established for inorganic materials in polymer templates,[99, 100] and has been demonstrated for organic materials in inorganic templates.[101] The latter technique involves energy intensive acid etching steps, which is a drawback when it comes to large scale production. Poly(3,4-ethylenedioxythiophene) gels have also been self-assembled into a double gyroid morphology via microemulsion synthesis.[102] Similarly to lipid bilayer structures, this system can, however, not be dried for further processing, and free standing functional materials can not be extracted. These drawbacks can be circumvented by using polymeric templates for the synthesis of three dimensional nanoporous conjugated polymers.

The similar chemical properties of the template material and the act-

ive material impose a variety of constraints on this process. After the self-assembly process, the polymer film has to be voided by selectively dissolving one of the copolymer blocks without altering the morphology of the remaining phase. Now the functional material has to be deposited without affecting the structural integrity of the template. In a third step, the polymer template has to be dissolved without impairing the structure or chemical properties of the conjugated material. Finally, an electrolyte is required, that facilitates a stable high performance operation of the active material.

The identification of a suitable set of orthogonal solvents for the various processing steps is a significant challenge. The drastically increased surface-area-to-volume ratio of the 3D nanostructured material, which is the primary desired feature, also has detrimental effects on the stabilities of the template and the active material. In particular, upon exposure to even a poor solvent, a certain surface layer of the polymer might be infiltrated and partially dissolved. In nanostructures a much larger proportion of the material is affected by this than in the bulk. Solvent-induced surface plasticisation with a penetration depth comparable to the strut radius will cause deformation and collapse of the respective structure, even for solvents incapable of dissolving the bulk polymer.[78]

A versatile synthesis route for 3D nanostructured conjugated polymer films using polymeric templates is presented in this chapter. Poly(pyrrole) (PPy), poly(3,4 - ethylenedioxythiophene) (PEDOT), as well as poly(3,4 - ethylenedioxythiophene methanol) (PEDOT-MeOH) were synthesised in double gyroid templates created by self-assembly of poly(styrene)-*block*-poly(D,L-lactide) or poly(4-fluorostyrene)-*block*-poly(D,L-lactide).

PEDOT and PEDOT-MeOH can be reversibly switched between two oxidation states with different optical appearances. This process relies on ionic transport,[103, 104] and its effect can be quantified by measuring the transmittance change, facilitating convenient performance benchmarking. To investigate the impact of the 3D nanopatterning on the material properties, the electrochromic performance of double gyroid structured PEDOT-MeOH was compared to nontemplated films. Finally, the compatibility of the presented synthesis pathway with conventional microfabrication techniques, and the sub-micron-scale accuracy of the electrodeposition step were demonstrated by the fabrication of electronically switchable Fresnel zone plates, capable of focusing incident light via diffraction.

4.2 Results and Discussion

4.2.1 Gyroid-Structured Conjugated Polymer Films

Figure 4.1 illustrates the central processing steps, and shows the resulting porous materials. The fabrication of nanostructured conjugated polymer films consists of four separate steps:

1. Fabrication of self-assembled gyroid templates.

2. Selective polymer removal, yielding a mesoporous scaffold.

3. Electropolymerisation of conjugated polymers in the voided template.

4. Template dissolution to obtain a free-standing conjugated polymer network.

Steps 1 and 2 are well established,[105–107] and a previously reported system was used in this study.[108] Steps 3 and 4 are not straightforward, and suitable solvents have to be identified and validated experimentally.

PPy and PEDOT are typically synthesised from acetonitrile and protic solvents, such as water.[86, 109–112] In the case of PPy, films with superior mechanical and electrical properties are generally achieved in acetonitrile-based electrolytes. This is likely because the chains become more and more hydrophobic as they grow during electropolymerisation.[109] The capability of acetonitrile to dissolve polystyrene, however, prohibits its use in combination with the present templates. Poly(styrene) and poly(fluorostyrene) exhibit excellent stability in water, which was therefore used as a solvent for the electropolymerisation of PPy, and high quality films were readily obtained.

The electropolymerisation of PEDOT and PEDOT-MeOH from aqueous solutions was less successful, and only non-uniform films could be fabricated. The results improved drastically, when a 1:1 mixture of water and methanol by volume was used instead, and dense blue films could be synthesised reliably. An alternative attempt to synthesise PEDOT derivatives from a trifluoroethanol based solution yielded inferior results.

The removal of the styrenic template in Step 4 without compromising the synthesised material required several attempts. First, toluene was used for this purpose, as it is generally considered a poor solvent for PEDOT,
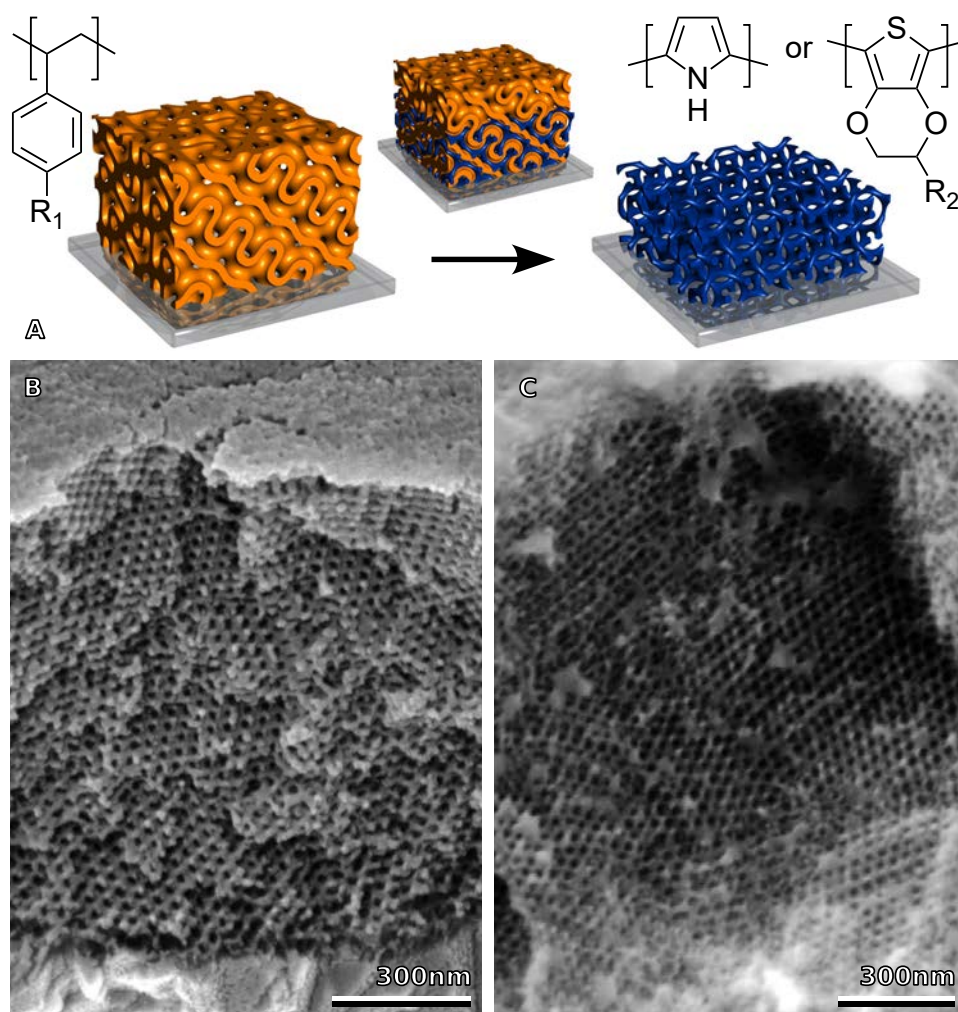
Figure 4.1. Preparation of DG-structured conjugated polymer electrodes. (**A**) Schematic illustration of the gyroidal polystyrene template, electropolymerisation and subsequent template dissolution, yielding a free-standing conjugated polymer replica (R_1=H, F and R_2=H, CH$_2$OH). (**B,C**) Cross-sectional SEM images of free-standing, mesoporous PEDOT-MeOH (B) and PPy (C) networks. This figure was created by M. R. J. Scherer.

and a good solvent for polystyrene. Jones *et al.* have demonstrated the synthesis of nanoporous PEDOT with a strut radius of around 50 nm from a toluene based solution,[113] indicating that even the nanostructured material is unaffected. The double gyroid structure of the PEDOT synthesised in this work was, however, degraded by toluene, as revealed via scanning electron microscopy (see Figure 4.2). The deformation was likely caused by the solvent induced plasticisation of a nanometre-thick surface layer.[78] This drastically reduced the stability of the nanometre-sized struts, and resulted in the decay of the entire periodic DG structure. The fact that the structure does not completely collapse suggests that the penetration depth of toluene in PEDOT is marginally smaller than the strut radius of the double gyroid.

In order to identify more suitable solvents, the Hansen solubility parameters were evaluated for a number of available substances. The Hansen solubility theory is based on the empirical assumption that mixing and dissolution occurs predominantly between similar molecules.[114] Three parameters are assigned to each molecule: δ_D, δ_P, and δ_H represent the intramolecular dispersion energy, the dipolar interaction energy, and the hydrogen bond energy, respectively. These parameters are interpreted as coordinates in an Euclidean space, and the distance Ra between two substances is

$$(Ra)^2 = 4(\delta_{D2} - \delta_{D1})^2 + (\delta_{P2} - \delta_{P1})^2 + (\delta_{H2} - \delta_{H1})^2. \tag{4.1}$$

A material-specific interaction radius R_0 is assigned to each substance, and it is assumed that all solvents within a sphere of this radius are capable of dissolving the substance.[114] This model is at best an approximation to the real solubility behaviour, as all δ-parameters are determined empirically. It is, however, commonly used for the screening of large numbers of solvents, in order to find a set of promising candidates for further evaluation.

The Hansen parameters for a variety of relevant materials are listed in Table 4.1. Table 4.2 shows the resulting Ra values for each polymer–solvent pair, and indicates the behaviour observed in this work.

This way, diethyl ether could be identified as a suitable selective solvent for freeing PEDOT and PEDOT-MeOH nanostructures. Due to its high volatility it proved practical to mix it in a 2:1 ratio by weight with hexane. PPy nanostructures, on the other hand, could be freed with xylene. Both template removal strategies worked reliably and without affecting the

Solvent/Polymer	δ_D [MPa$^{0.5}$]	δ_P [MPa$^{0.5}$]	δ_H [MPa$^{0.5}$]	Reference
PS	21.3	5.75	4.3	[114]
PFS	19.4	3.4	3.6	[115]
PPy	18.9	12.9	10.4	[115]
PEDOT	21.2	7.4	8.1	[115]
Acetone	15.5	10.4	7.0	[114]
Acetonitrile	15.3	13.0	6.1	[114]
Benzene	18.4	0.0	2.0	[114]
Cyclohexane	16.8	0.0	0.2	[114]
Diethyl ether	14.5	2.9	5.1	[114]
Ethanol	15.8	8.8	19.4	[114]
Ethanolamine	17.2	15.6	21.3	[114]
Ethylene carbonate	19.4	21.7	5.1	[114]
Formamide	17.2	26.2	19.0	[114]
Hexane	14.9	0.0	0.0	[114]
Isopropanol	15.8	6.1	16.4	[114]
Methanol	15.1	12.3	22.3	[114]
Toluene	18.0	1.4	2.0	[114]
Water	15.6	16.0	42.3	[114]
Xylene	17.8	1.0	3.1	[114]
Chlorobenzene	19.0	4.3	2.0	[114]

Table 4.1. Experimentally determined and theoretically calculated Hansen solubility parameters for selected polymers and solvents. This table was adapted from Ref.[32]

delicate features of the double gyroid structured materials (see Figures 4.1, 4.2).

4.2.2 Optical Properties

Colouration Contrast

The impact of the nanostructured morphology on the properties of the conjugated polymers was evaluated by comparing the electrochromic performance of double gyroid structured PEDOT-MeOH films to non-patterned equivalents.

In a first step, a range of films with different thicknesses were electropolymerised from solution. The electric charge required for the electropolymerisation of PEDOT-MeOH is proportional to the amount of material deposited. This facilitates an indirect control of the deposited film thickness via the spatial charge density. The deposition was carried out in styrenic double

	PS		PFS	PPy		PEDOT	
Acetone	13	★	11	8		12	
Acetonitrile	14	★	13	8		13	
Benzene	8	★	4	15		11	
Cyclohexane	11	★	7	17		14	
Diethyl ether	14	★	10	14		14	●
Ethanol	19	●	18	12		16	●
Ethanolamine	21	●	22	12		17	
Ethylene carbonate	16	○	18	10		15	
Formamide	26	●	28	16		23	
Hexane	15	●	10	18		17	
Isopropanol	16	●	15	11		14	
Methanol	23	●	22	14		19	●
Toluene	8	★	4	14	○	11	○
Water	41	●	41	33	●	37	●
Xylene	9	★	4	14	●	11	○
Chlorobenzene	5	★	2	12		8	

Table 4.2. Calculated Ra values for selected polymer–solvent combinations.
★ Good solvent, complete polymer dissolution.
○ Poor solvent, only affects nanostructured features.
● Non-solvent, no effect on nanostructures.
This table was adapted from Ref.[32]
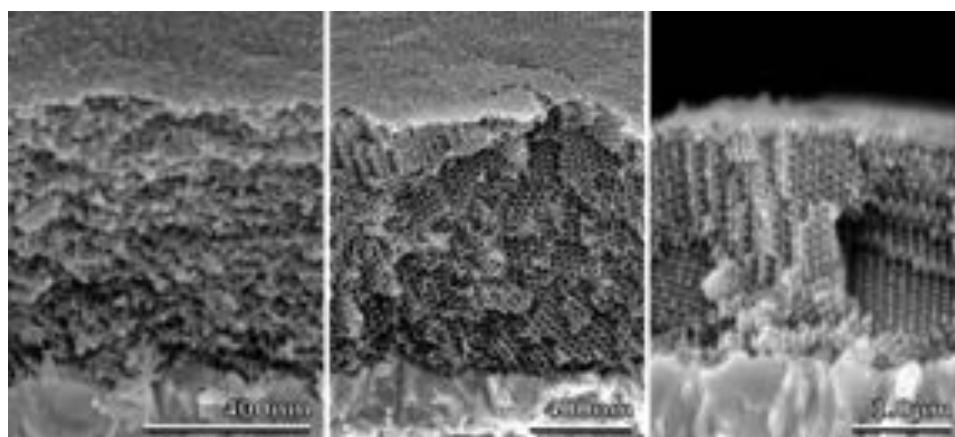
Figure 4.2. PEDOT derivatives after solvent exposure. Left: Deformed PEDOT network after template removal with toluene. Centre: PEDOT network after template removal with a 2:1 mixture of diethyl ether and hexane. Right: PEDOT-MeOH network after template removal with a 2:1 mixture of diethyl ether and hexane. The electron micrographs were recorded by M. R. J. Scherer.
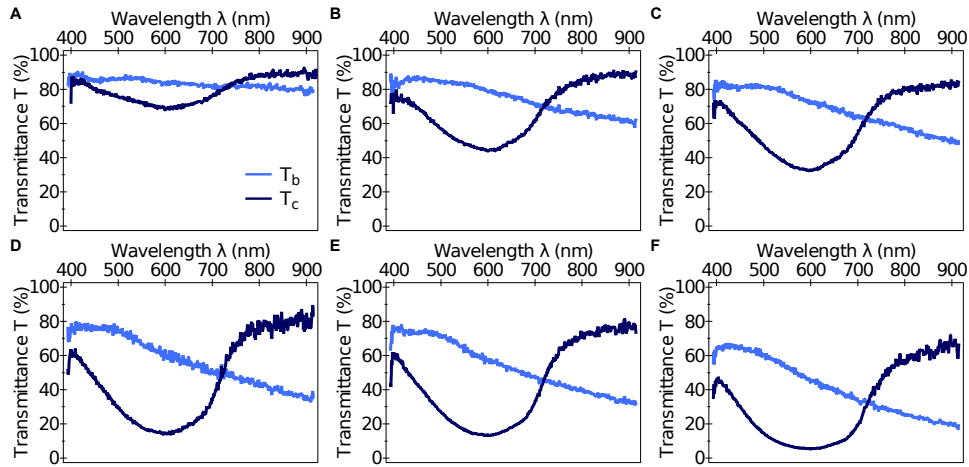
Figure 4.3. **Optical transmittance spectra of DG-nanopatterned PEDOT-MeOH devices in a 0.2 M aqueous lithium perchlorate electrolyte.** Displayed are the coloured $(-2.1\,\text{V})$ and bleached $(+1.0\,\text{V})$ spectra for electrochromic devices with the following deposition charge densities: **A**, $0.21053\,\text{mC/mm}^2$, **B**, $0.31579\,\text{mC/mm}^2$, **C**, $0.52632\,\text{mC/mm}^2$, **D**, $0.63158\,\text{mC/mm}^2$, **E**, $0.84211\,\text{mC/mm}^2$, and **F**, $1.05263\,\text{mC/mm}^2$. This figure was created by M. R. J. Scherer.

gyroid templates on transparent conducting electrodes (FTO). After deposition and template removal, the films were immersed in a $0.2\,\text{M}$ solution of lithium perchlorate in deionised water, and encapsulated with another transparent electrode. The optical transmittance $T(\lambda)$ of the films was measured across the visible spectrum while a voltage was applied. With the voltage at -2.1 V the films are in their coloured state with transmittance T_{c}, at a potential of $+1.0\,\text{V}$ the films are bleached (T_{b}). The terms "coloured" and "bleached" refer to the spectral range below $\approx 720\,\text{nm}$. For higher wavelengths the behaviour is inverted.[103]

The transmittance spectra are shown in Figure 4.3, and the values for λ = 532 nm as well as the contrast $\Delta T = T_{\text{b}} - T_{\text{c}}$ at this wavelength are plotted against the respective deposition charge densities in Figure 4.4A. A non-templated device was fabricated with $|Q| = 630\,\text{mC}\,\text{mm}^{-2}$, and compared to the equivalent templated film in further characterisation steps. Figure 4.4B shows that the colouration contrast ΔT of the mesoporous device is increased across the entire spectrum, and at 532 nm it is approximately 48 % compared to 34 % for the non-templated film.
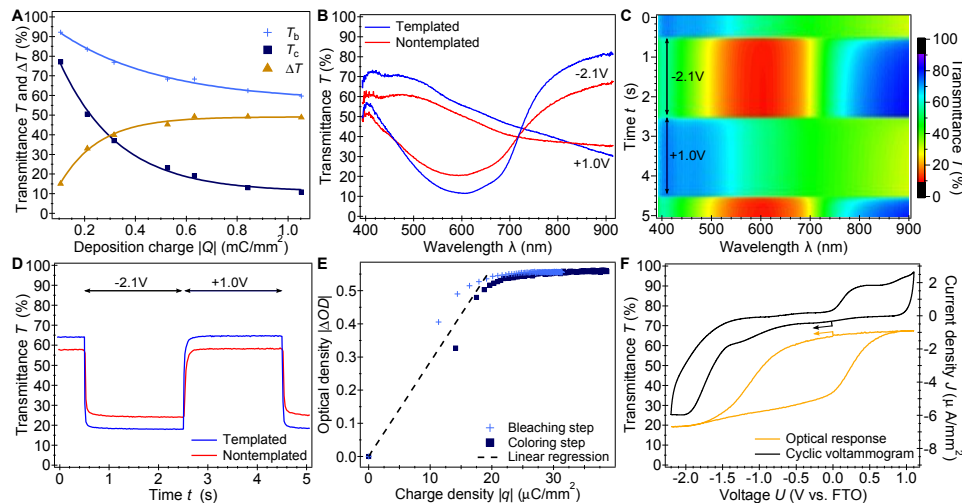
Figure 4.4. Electrochromic performance of PEDOT-MeOH films in 0.2 M lithium perchlorate in water. (**A**) Dependence of the extreme transmission values (T_c at -2.1 V and T_b at $+1.0$ V) at $\lambda = 532$ nm on the overall film deposition charge (Fig. 4.3). The film electrosynthesised with 630 mC/mm^2, which corresponds to a film thickness of about 520 nm, showed an optimal colouration contrast of $\Delta T = T_b - T_c = 48.5\%$. (**B**) Optical transmittance spectra of the coloured (-2.1 V) and bleached ($+1.0$ V) states. A nontemplated film prepared with the same deposition charge density showed a lower colouration contrast of only $\Delta T = 34.2\%$ at $\lambda = 532$ nm. (**C**) Transmittance variation upon alternating 2 s potential steps (-2.1 V and $+1.0$ V), recorded with a 20 ms integration time, visualising a consistently fast switching response over the entire visible spectrum. (**D**) Time-resolved switching behaviour of DG-structured and non-templated PEDOT-MeOH films at $\lambda = 532$ nm. The DG device exhibited characteristic switching times τ of 23 and 14 ms for the colouring and bleaching processes, respectively. The corresponding values for the non-templated sample were 40 and 29 ms. (**E**) Optical density $|\Delta OD|$ at $\lambda = 532$ nm versus charge density $|q|$ calculated from (D) and the switching current. A linear regression of the combined bleaching and colouration cycles give an average CCE of 285 cm^2/C for a 94 % completed switch. (**F**) Optical transmittance response at $\lambda = 532$ nm in relation to the applied cell potential, and corresponding CV curve, recorded for the 24$^{\text{th}}$ switching cycle at a scan rate of 0.1 V/s. This figure was created by M. R. J. Scherer.

Composite Colouration Efficiency

The energy consumption of electrochromic devices is an important factor for potential applications. It can be evaluated by measuring the composite colouration efficiency $CCE = \Delta OD/q$, which quantifies the electrical charge q required to drive a change in the optical density $\Delta OD = \log(T/T_0)$.[116] The nanostructured device exhibited a CCE value of approximately $285\,cm^2/C$ for $94\,\%$ of the total transmittance change at $\lambda = 532\,nm$ between potentials of -2.1 and $+1.0\,V$ (see Figure 4.4E). This CCE value compares well to values between 180 and $360\,cm^2/C$, that have previously been reported as high.[117–119] The bulk film only reached a CCE value of $140\,cm^2/C$.

For practical applications, the ability to precisely tune the transmitted intensity of an electrochromic device is often advantageous. Figure 4.4F shows the optical response of the fabricated mesoporous device to a cyclic voltammogram between -2.2 and $+1.1\,V$. The moderate slope of the transmittance curve indicates that subtle changes in transmittance can be generated by controlling the applied voltage. The transmittance changes in both switching directions occur when the current density changes, which is mainly in the voltage range between -1.5 to $+0.5\,V$. Outside this range only small changes occur, driven by much larger currents. These high currents are probably related to unwanted side reactions, such as water splitting, and will limit the achievable CCE values. It might therefore be possible to achieve even higher CCE values if the double gyroid structured films are cycled in more stable electrolytes, like acetonitrile or propylene carbonate.

The results presented in Fig. 4.4 were reproducible, subject to only minor fluctuations. These are likely to originate from variations in environmental conditions, such as ambient temperature and humidity, during the sensitive infiltration and electropolymerisation processes.

Switching Rates

A crucial parameter for display materials is the time scale, on which colour-changes can be achieved. In order to display 25 different images per second, a colour change has to be completed within $40\,ms$. To analyse the switching rates, a step potential was applied with instantaneous voltage changes between $+1.0$ and $-2.1\,V$. The time-resolved spectral response of the templated film is plotted in Figure 4.4C, and shows consistently fast switching.

Time dependent transmission values at $\lambda = 532\,\text{nm}$ are shown in Figure 4.4D for the templated and non-templated films. To quantify the switching rate, the function $T(t) = T_0 \pm \Delta T \cdot e^{-t/\tau}$ was fitted to the data. The characteristic time τ of the mesoporous film was $\tau_\text{b} = 14\,\text{ms}$ for the oxidation step, and $\tau_\text{c} = 23\,\text{ms}$ for the reduction process. Both reactions took roughly twice as long in the standard film ($\tau_\text{b} = 29\,\text{ms}$ and $\tau_\text{c} = 40\,\text{ms}$).

The enhanced switching speed in the templated films is likely caused by the electrolyte in the pores, which reduces the required ionic diffusion distances to strut radius length scales. The thickness of the non-templated film was approximately 200 nm, which can be considered very thin. The switching time of a bulk film is expected to increase significantly with the film thickness, whereas the response time of the nanostructured material is likely to be largely unaffected.

Even faster colour switching processes in PEDOT have been reported previously, with characteristic times of less than 10 ms.[101] It can be assumed that these high switching rates are mainly caused by the acetonitrile based electrolyte.[120] In an attempt to further enhance the performance of the nanostructured devices, new films were fabricated and immersed in an acetonitrile based electrolyte for optical characterisation. Electrical switching of these samples, however, led to a rapid decay of the optical contrast between the coloured and bleached states. This is a strong indication for partial dissolution and a resulting structure loss, which was confirmed for PEDOT and PEDOT-MeOH via electron microscopy.

The reason some PEDOT nanostructures are stable in acetonitrile based electrolytes is probably related to their fabrication history. Cho *et al.*, for example, also synthesised their material from acetonitrile,[101] which means that only polymer chains long enough to be insoluble were actually deposited. In agreement with this hypothesis is the observation that films synthesised from, and operated in, the same electrolyte exhibit superior stability. The use of triethylsulfonium bis(trifluoromethylsulfonyl) imide resulted in very stable films with inferior switching performance. The water based films examined here also exhibited stable switching performance for more than 50 cycles, (see Fig 4.5) and significant degradation only occurred after several hundred voltage changes. It is difficult to put these values into perspective, as the stability of other electrochromic devices is often not investigated or reported in the literature.
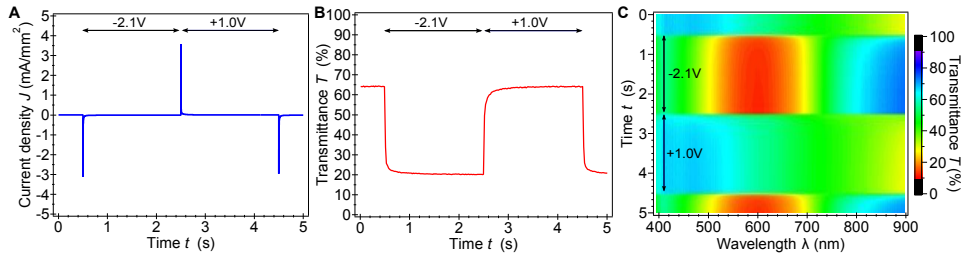
Figure 4.5. Electrochromic performance of DG-structured PEDOT-MeOH after 50 switching cycles. To investigate the stability of the material under the extreme electronic potentials, a device was characterised after 50 full switching cycles. The zero current density during the potentiostatic steps proves the absence of unwanted side-reactions, and the chemical stability of the material. The time constants, as well as the switching amplitude, only showed slight deviations from the respective values in the first cycles, indicating good chemical stability. This figure was created by M. R. J. Scherer.

In summary, all of the examined electrolytes have distinct advantages and disadvantages in terms of switching speed, optical contrast, or chemical stability. Cho *et al.*, for example, report switching rates of 10 ms, while the reflectivity changes of their films are limited to $\Delta R \approx 25\,\%$.[101] The identification of electrodeposition and operation electrolytes, that combine the desired advantages, is therefore a highly promising route towards devices applicable in a commercial context.

4.2.3 Fresnel Zone Plates

The templated fabrication of double gyroid structured materials was combined with photolithography, to demonstrate its versatility and compatibility with commercial processing routes. A zone plate pattern was chosen for this exercise, as it facilitates a global quantitative analysis of the fidelity of the overall process: Fresnel zone plates focus light via diffraction, which can only be effective when all features are precisely positioned and sized.

The opaque zones of a Fresnel zone plate block half of the incident light in such a way, that the remaining light shows constructive interference in a focal point on the optical axis of the device. This interference is achieved by covering the device with a set of concentric ring zones with outer radii $r_{\mathrm{k}} = \sqrt{k\lambda f + k^2\lambda^2/4}$. Here, λ is the wavelength to be focused, and f is the focal length of the zone plate lens. The radii are chosen so that the optical path between any point on the corresponding circle and the focal point is $f + k \cdot \lambda/2$. This means that light passing through two neighbouring rings has a path difference of $\lambda/2$ and shows destructive interference at the

focal point. Zones with even indices, however, only have path differences that are integer multiples of λ between each other. Light focusing can thus be achieved by preventing transmission through all zones with odd indices, while keeping even index zones transparent (or vice versa). Deviations from the ideal pattern will reduce the intensity at the focal point, and global defects will prevent the positive interference altogether, making it an ideal test pattern for delicate procedures. A zone plate was fabricated here with the opaque zones made from PEDOT-MeOH, which facilitates electrical switching between a focusing and a non-focusing state.

Because the bleached state of the PEDOT-MeOH is not fully transparent, and the coloured state is not fully opaque, such a device can only be switched between two states with a finite focal intensity ratio. In a simplified model, one can assume that all light transmitted through the opaque zones reduces the focal intensity via destructive interference, and is practically deducted from the constructive interference of the transparent zones. As the transparent and opaque zones cover approximately equal areas of the device, equal numbers of photons will be transmitted through them. The focal intensity is thus proportional to the transmittance difference $T_\mathrm{t} - T_\mathrm{o}$ between the transparent and opaque zones. The transparent zones can be assumed to have a transmittance of 1, while the opaque zones are switched between T_b and T_c. This means that the expected focal intensity ratio between the coloured and the bleached states is $(1 - T_\mathrm{c}) : (1 - T_\mathrm{b})$.

Another deviation from the ideal case is the fact that the device has to be encapsulated between two glass substrates, and the light diffracted by the zone plate will undergo refraction at the glass–air interface. The magnitude of this refraction, and with it the additional optical path traversed by the light on its way to the focal spot, will depend on its angle of incidence on the glass–air interface. This angle of incidence is a function of the radius of the respective zone, which in turn has to be adjusted from the formula stated above to ensure the interference condition is still valid.

Here, a $15 \times 15\,\mathrm{mm}^2$ zone plate was fabricated for green light ($\lambda = 532\,\mathrm{nm}$) and a focal length f of $250\,\mathrm{mm}$. First, the transparent zones were replicated in SU-8 via photolithography on an FTO-covered glass substrate. A double gyroid polymer template was then manufactured on top of this assembly, before the electropolymerisation of PEDOT-MeOH was carried out. The local insulation by the SU-8 pattern ensures that the electrochromic
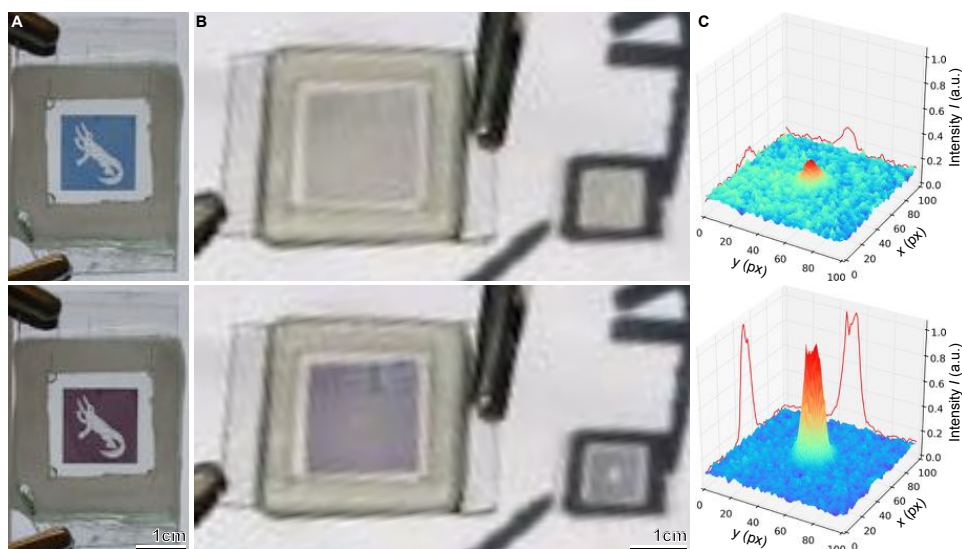
Figure 4.6. Electrochromic PEDOT-MeOH devices. (**A**) A $13 \times 13\,mm^2$ device in the bleached (top, $+1.0\,V$), and coloured (bottom, $-2.1\,V$) states, showing the Cavendish Laboratory logo. The device exhibits homogeneous colouration throughout the entire active area in both states. (**B**) A zone plate device, illuminated by unfiltered sunlight. Despite the intrinsic wavelength dependence of the diffractive focusing, the focal point is clearly visible for the bleached (top) and coloured (bottom) states. As expected, the focal intensity is significantly increased in the coloured state, supporting the working assumption on the underlying mechanism. Note that devices (A) and (B) were photographed with different cameras under different lighting conditions. This, and the fact that only 50% of the device in (B) is covered with electrochromic material, causes different colour contrasts in the images. (**C**) 2D intensity profile of the focal plane of a PEDOT-MeOH zone plate. The device was illuminated with a collimated beam of green light ($\lambda = 532\,nm$) with a diameter of approximately $10\,mm$. The profile was recorded with a Canon EOS 450D sensor (exposure $= 1/4000\,s$, ISO-400, $1\,px = 5.2\,\mu m$). In the coloured/focusing state (bottom) the intensity of the focal spot was increased by more than a factor of 3 compared to the bleached state (top). The focal spot was very well defined, with a full width at half maximum of $\approx 72\,\mu m$.

material is only deposited in the opaque zones, and after the removal of the template a zone plate pattern remained on the substrate. Finally the entire device was encapsulated in an electrolytic cell, to facilitate voltage induced transmittance changes.

Despite its intrinsically wavelength-dependent focusing mechanism the device performs well in unfiltered sunlight (see Figure 4.6B). To quantify this performance, the device was irradiated with a $10\,mm$ wide collimated beam of filtered light from a xenon lamp[2] ($\lambda = 532 \pm 2.5\,nm$). In order to measure the magnitude and spatial extent of the focal spots, an objective-

---

[2]XBO 75 W/2 OFR, OSRAM GmbH, Munich (Germany)

less digital SLR camera[3] was used, with the sensor placed in the focal plane of the zone plate. To improve the signal-to-noise ratio, the entire assembly was shielded from ambient light, and the camera exposure time was maximised, narrowly avoiding overexposure. Intensity maps were recorded under identical conditions for the bleached and coloured states, and are presented in Figure 4.6C. The focusing power of the zone plate was evaluated by comparing the peak intensities of the focal points of the bleached and coloured states. This ratio was approximately 1.0:0.3, which is better than the estimated ratio of 1.0:0.4 for a device with transmittances between 18% to 65% (see above for derivation). The full width at half maximum of the focal spot can be determined via the pixel spacing of the SLR sensor, which Canon states as $5.2\,\mu\mathrm{m}$.[121] The resulting value of only $72\,\mu\mathrm{m}$ shows that the focusing is working well, and that therefore the overall precision of the processing route is high.

4.3 Conclusion

In summary, a reliable fabrication pathway for free-standing 3D nanostructured PEDOT, PEDOT-MeOH and PPy via self-assembled polystyrene templates is presented in this chapter. The fabrication route does not involve etching steps with corrosive acids, and can be adapted to a variety of other conjugated polymers, if a suitable set of orthogonal solvents can be identified. The electrochromic devices fabricated via this pathway were superior to non-patterned equivalents in terms of maximum optical contrast, switching speed and composite colouration efficiency. The performance may be further enhanced by carefully optimising the synthesis and operation conditions, for example by adjusting the electrolyte composition. The fabrication of the electrically switchable zone plate demonstrates the reliability and scalability of this 3D nanopatterning approach, considering in particular the large number of constraints imposed on the system by the various independent processing steps.

---

[3]Canon EOS 450D

4.4 Experimental Methods

The polymer templates with a double gyroid morphology were fabricated following a protocol previously published by Scherer *et al.*[122] Poly(styrene)-*b*-poly(D,L-lactide) (PS-*b*-PLA)[4] and poly(4-fluorostyrene)-*b*-poly(D,L-lactide) (PFS-*b*-PLA)[5] were spin-cast onto fluorine-doped tin oxide covered soda lima glass (FTO), and thermally annealed as described in Section 3.2. The samples were heated to $173\,°C$ at a rate of $150\,°C/h$ in vacuum. After 20 minutes at the peak temperature, the vacuum oven was purged with nitrogen, the chamber was opened, and the samples were immediately placed on a large piece of cool metal. The PLA microphase was selectively dissolved in an aqueous sodium hydroxide solution with a pH value of ≈ 13, leaving behind a double gyroid network with $\approx 37 - 38\,\%$ porosity.

The templated synthesis of conducting polymers was carried out using a potentiostat[6] with a saturated calomel reference electrode (SCE) and a stainless steel counter electrode. Before immersing the substrates in the electrolyte, they were rinsed with methanol[7]. This improves the infiltration of the porous network by the high surface tension electrolytes, and ensures defect-free deposition.

PEDOT and PEDOT-MeOH were electropolymerised from a 1:1 water:methanol mixture with $0.02\,M$ of the respective monomer, and $0.1\,M$ lithium perchlorate. First, a potential of $1.55\,V$ vs. SCE was applied for $0.5\,s$ to ensure homogeneous nucleation, before the synthesis was carried out at $1.05\,V$ until the desired deposition charge density was reached. After the electrodeposition, the samples were again rinsed with methanol and then dried on a hotplate at $50\,°C$ for $10\,min$.

The polystyrene templates were dissolved by immersing the samples in a 2:1 mixture by volume of diethyl ether and hexane, and a free standing double gyroid structured PEDOT(-MeOH) network was obtained.

The PPy synthesis was carried out in a similar fashion, with the exception of the electropolymerisation step. Here, an aqueous solution containing $0.1\,M$ p-toluenesulfonic acid monohydrate, $0.1\,M$ sodium chloride and $0.5\,M$ pyrrole was used.[123] The nucleation sites were created by a $1\,s$ step at $1.05\,V$

---

[4]$M_{\mathrm{W}} = 21.6\,kg/mol$, PDI $= 1.09$, $f_{\mathrm{PLA}} = 39.8\%_{\mathrm{wt}}$
[5]$M_{\mathrm{W}} = 24.0\,kg/mol$, PDI $= 1.10$, $f_{\mathrm{PLA}} = 38.2\%_{\mathrm{wt}}$
[6]AUTOLAB PGSTAT302N, Metrohm Autolab B.V., Utrecht (Netherlands)
[7]Analytical Reagent Grade, Fischer Scientific, Leicestershire

vs SCE, and the electropolymerisation was carried out at 0.65 V. As oxygen promotes the spontaneous oligomerisation of pyrrole, the solution had to be bubbled with nitrogen before use, and the synthesis was carried out under an inert atmosphere. The PPy synthesis was optimised by M. R. J. Scherer and A. Nicholas.

The fabrication of the PEDOT-MeOH zone plate devices relies on a patterned modification of the conducting substrate. This was achieved via photolithography, and first a 1:3 mixture of SU-8 2000.5 photoresist and SU-8 2000 thinner was prepared. The substrate was then spin-coated with this mixture at 6000 rpm for one minute (ramp rate 500 rpm/s), obtaining an approximately 80 nm thick layer of SU-8. The next steps were a pre-bake, to ensure a completely dry polymer layer, and a 2 s masked UV-exposure to locally cross-link the resist. The exposure was carried out in a mask aligner[8] with a custom made chrome mask[9]. A post-bake was performed to complete the cross-linking process, and the samples were immersed in SU-8 developer[10] for 10 s. The pre- and post-bake procedures were as follows: 1 min at 65 °C, 1 min at 100 °C, and 1 min at 65 °C.

Encapsulated electrolytic cells were manufactured by first preparing an approximately 1 mm thick thermoplastic gasket[11], and placing it around the active material. Now a FTO counter-electrode was placed on top of the gasket with the conductive side facing downwards, and the thermoplastic was fused at 50 °C for 1 min. The resulting sealed cell was filled with electrolyte via injection through the gasket with a small needle. Finally, the gasket was covered with a protective layer of epoxy glue[12].

---

[8]MJB4, SussMicroTec; λ >365 nm; 60–80 mJ/cm^2

[9]JD Photo-Tools, Hitchin

[10]propylene glycol monomethyl ether acetate

[11]Parafilm M®, Bemis NA, Wisconsin, USA

[12]Loctite® Double Bubble, Henkel Ltd., Hemel Hempstead

5

Optical Characterisation of Large Domain Gold Gyroids

The work presented here is being prepared for publication by James A. Dolan*, Raphael Dehmel*, Matthias Saba, Bodo D. Wilts, Angela Demetriadou, Yibei Gu, Ilja Gunkel, Timothy D. Wilkinson, Ulrich Wiesner, Ortwin Hess, Jeremy J. Baumberg and Ullrich Steiner. Optical characterisation was coordinated by J. A. Dolan, while the author was responsible for the solvent vapour annealing.

This chapter describes the fabrication of gold gyroid metamaterials and their optical characterisation via goniometric measurements. Polymer templates were fabricated for this purpose via self-assembly and selective etching. The goniometric measurements involve shallow illumination angles and thus large beam footprints. Long range order on the $100\,\mu m$ scale is therefore an important prerequisite for the characterisation of individual domains, and a solvent vapour annealing protocol was optimised for this purpose. A large number of transmission and reflection spectra were recorded under various illumination conditions, and selected data are presented here. The detailed and in-depth analysis of the data requires advanced modelling, which will be presented in future publications.

---

*J. A. Dolan and R. Dehmel contributed equally to this work.

5.1 Introduction

In recent years *optical metamaterials* have gained increasing attention in the scientific community. Optical metamaterials are materials whose optical properties are influenced by their morphology as well as their chemical composition.[124] This is also the case for so-called photonic crystals, where periodic structures on the wavelength scale cause diffractive effects.[125] Metamaterials, on the other hand, have features significantly smaller than the observation wavelength, and can thus be seen as a homogeneous medium.

Much of today's theoretical and experimental work is — directly or indirectly — inspired by V. G. Veselago's paper from 1967, where he investigates the propagation of electromagnetic waves in "Substances with Simultaneously negative Values of ε and μ".[126] Starting from the Maxwell equations, he derives that $\vec{E}$, $\vec{H}$ and $\vec{k}$ form a left-handed set for a plane wave propagating in a medium with negative ε and μ. This implies negative refraction, as these vectors always form a right-handed set for $n > 0$. A lot of attention was directed to this work in the year 2000, when J. B. Pendry showed that lenses made from such a *negative index material* (NIM) could overcome the diffraction limit of conventional light microscopes, and resolve features significantly smaller than the observation wavelength.[127] A negative dielectric permittivity occurs in many metals at optical frequencies. Materials with a negative magnetic permeability, on the other hand, don't occur naturally. Arrays of conducting split ring resonators (SRRs) can be used to achieve this effect,[128] and an SRR-based NIM for microwave frequencies was successfully fabricated by Smith *et al*.[129] The electronic resonance condition was fulfilled by combining the SRR array with a grid of thin metallic wires, where self-inductance effects suppress the plasma frequency to an adjustable extent.[130] Negative refraction in the short-wavelength infrared spectrum has been demonstrated by scaling the structures to much smaller sizes via focused ion beam milling.[131] A disadvantage of this approach is the often lossy nature of magnetic resonators.

An alternative concept was suggested by J. B. Pendry in 2004.[132] He argues that the insertion of oscillating dipoles into a strongly chiral medium causes a wide frequency range with a negative refractive index for a particular polarisation. This prospect makes the gyroid an interesting

candidate for negative refraction: the chiral gyroids resulting from polymer self-assembly naturally have unit cell sizes significantly smaller than visible wavelengths.[133] Moreover, the template-based fabrication approach facilitates the structuring of a wide range of materials, and is — in contrast to conventional top-down techniques — not limited to microscopic sample sizes.

Vignolini *et al.* have fabricated and analysed a gold single gyroid with a unit cell size of 50 nm and domain sizes of 10–100 µm.[134] They report the observation of linear and circular dichroism, as well as a significant depression of the plasma frequency. In a further report the fill fraction and the unit cell size of the single gyroid, as well as the refractive index of its surrounding medium were varied, and the impact of these changes on the optical response was investigated.[135] To explain the observed optical properties of the single gyroid, a theoretical model based on arrays of conducting helices has been developed and refined.[136, 137] Both versions describe well some of the observed phenomena, while failing to account for others.[138] One particular shortcoming is the failure to correctly predict the polarisation dependence of the optical response, i.e. the linear dichroism.

Previous optical measurements on gold gyroids were carried out under normal incidence, with the exception of one scan of the azimuthal angle at a fixed angle of elevation. The existing theoretical models can therefore only be fitted to a very limited data set, as all of the characterised gyroids were oriented with the (110) direction out of plane. Based on the assumption that the optical responses for different illumination angles of a structure are intrinsically related, the degree of uncertainty of any fit can be significantly reduced when a wider range of data points is considered.

J. A. Dolan is currently working on a model capable of describing the observed behaviour for all angles of incidence. This endeavour relies on experimental measurements, which were conducted in collaboration with the author and are described in this chapter. Reflectance and transmittance spectra were recorded for all feasible combinations of the azimuthal and elevation angles for a variety of polarisation states. For these measurements it was of utmost importance that only one domain contributes to each recorded data set, as otherwise a superposition of several orientations would falsify the spectra. The increased beam footprint at shallow angles of incidence implies that samples with long range order on the 100 µm scale are required.

Previously, polymer samples with long range order were fabricated by slowly drying semi-dilute polymer solutions.[134, 135] In a first attempt, the same method was applied to the available isoprene-*b*-styrene-*b*-ethylene oxide triblock copolymers (ISO). These polymers have a significantly higher molecular mass compared to the material used for previous reports, while the volume fractions of the individual blocks are identical. The drying method proved unreliable and time consuming, and a more controlled approach to the sample fabrication was sought.

The combination of mass flow controllers and solvent bubblers as described by S. Hüttner *et al.* facilitates precise and dynamic control of the solvent vapour pressure in the annealing chamber.[139] This was utilised to first swell and then dry thin polymer films in predefined ways, and samples with sufficient long range order could be produced reliably. Gold replicas of the self-assembled structures were characterised optically in custom built goniometers, and a selection of the data is presented here. The detailed analysis of the recorded spectra will be presented in future publications.

5.2   Results and Discussion

Based on the principles outlined in Section 2.3.3, a solvent vapour annealing protocol was developed, with the aim of promoting microphase separation with enhanced long range order in thin films of a gyroid forming ISO polymer. The idea of this approach was to ensure a high degree of reproducibility, which is a crucial prerequisite for any systematic study.

5.2.1   Long-range Order Microphase Separation via SVA

The initial working hypothesis was that sufficiently slow drying of the sample films from a highly swollen disordered state would cause a reduced nucleation density of the microphase separation, and yield samples with a certain degree of long range order. In subsequent experiments, the film swelling ratio at which this nucleation occurs should be identified, allowing the design of short and effective annealing protocols.

For this purpose a thin film sample was annealed, with the temperatures of the solvent reservoir and the annealing chamber held at 25 °C, and the mass flow controllers initially set to 1.0 sccm for the dry channel, and 19.0 sccm for the channel connected to a chloroform bubbler. The total

gas flow thus consisted of 5 % dry gas, and 95 % saturated carrier gas. For the sake of simplicity the gas flow settings are described in the following by stating the proportion — or concentration — of saturated gas. Unless otherwise specified the combined flow of both channels was always 20.0 sccm. The concentration was held at 95 % for 30 minutes, until it was decreased at a constant rate, reaching 0 % after 20 hours. Examination of the annealed film revealed a complete microphase separation into the gyroid phase, and the absence of any significant long range order. The experiments were repeated with drying times of up to 100 hours, again without success.

These observations suggest that the nucleation of the microphase separation takes place before the annealing procedure, i.e. during spin coating or in solution. During solvent vapour annealing, the mobility of the polymer is sufficient for the completion of this microphase separation, but reorganisations of entire domains are still too slow to be observed.

To investigate this hypothesis, the solvent content of the films had to be increased to further enhance the mobility of the polymer chains. A potential side effect of this is a change of the equilibrium morphology through selective swelling. To increase the solvent uptake of the polymer, a negative temperature gradient between the bubbler and the annealing chamber was introduced. The carrier gas was thus cooled down into a supersaturated state upon entering the chamber, and the amount of solvent transferred to the sample was increased. Thin film interferometry, as described in Section 3.3.2, confirmed the significant impact of temperature gradients on the achievable swelling ratios. The drawback of this approach is the potential condensation of solvent vapour in the annealing chamber, which limits the controllability of the procedure. In contrast to the isothermal case, the film thickness does not asymptotically approach a certain value. A slow linear increase after a fast initial swelling step is observed instead. When the temperatures of the annealing chamber and the solvent reservoir are 23 and 25 °C, respectively, the swelling ratio reaches values of around 7 approximately 15 minutes after a gas flow with a concentration of 95 % is introduced. These values should, however, only be seen as rough orientation points, as the detected interference fringes significantly decrease in amplitude with increasing solvent content of the film, and reasonable interference patterns can no longer be fitted to the recorded spectra. This is likely due to an increasingly smooth refractive index profile at the interface between the swollen
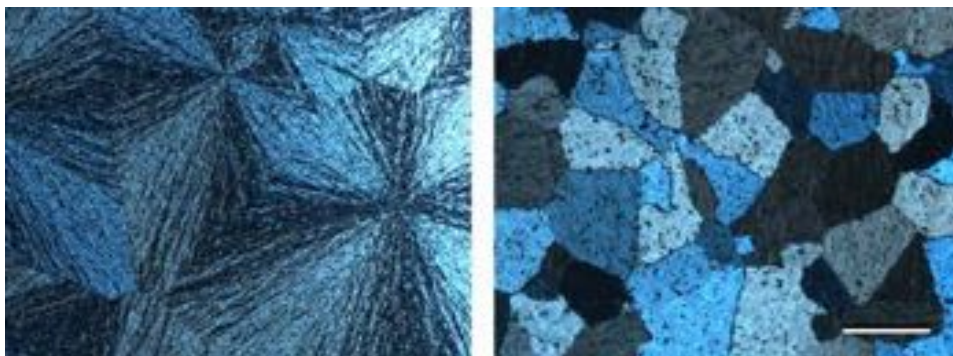
Figure 5.1. Optical micrographs of as-annealed polymer films. ISO films on silicon substrates observed under crossed polarisers. The left image shows a spherulitic Maltese cross pattern. The sample shown on the right is covered with uniform domains. The scale bar is 200 µm.

polymer film and the supersaturated gas atmosphere, which suppresses and blurs the light reflection at this surface.

A variety of annealing protocols was tested in this configuration, and enhanced long range order was first observed when the following concentration profile was applied: After 30 minutes at 95 %, the concentration was steadily ramped down to 60 % over a 19 h timespan. The film was then dried by a 30 minute linear concentration decrease to 0 %. The sample exhibited long range order with domain sizes of up to approximately 400 µm, which is sufficient for optical characterisation. Although the result aligns well with the prediction that slow drying from a strongly swollen state causes a low nucleation density and thus large domains, the reproducibility was extremely poor. The results of identical follow-up experiments varied hugely, and samples with a variety of optical appearances were obtained. The observations fall into three categories: Spherulitic birefringence patterns, uniform domains of birefringence, and samples without birefringent features. All of these categories occurred either in the form of smooth films, or with a micron-scale surface roughness. Optical micrographs of spherulitic and uniform birefringence are shown in Figure 5.1.

The birefringence is caused by a preferentially aligned crystallisation of the poly(ethylene oxide) microphase,[140] and the uniform domains coincide with domains of long range order in the microphase separated structures, as shown in Chapter 6. This correlation was immensely useful for further studies, as it allowed a rapid characterisation of the microphase separation via polarised light microscopy. Alternatively, the nanoscale morphology of
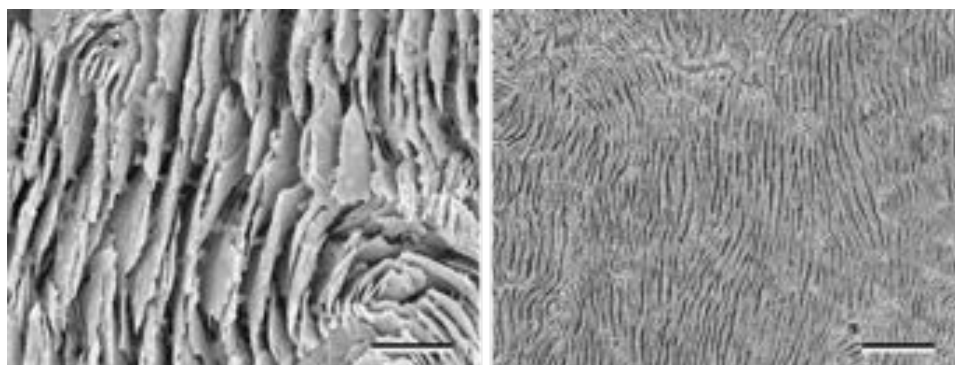
Figure 5.2. SEM micrographs of self-assembled lamellae. The gold replica of the isoprene block forms lamellar structures with the sheets oriented perpendicular to the substrate. The scale bars are 1 μm (left) and 5 μm (right).

the samples could be evaluated by imaging a free standing gold replica of the isoprene phase via scanning electron microscopy. Samples with uniform birefringent domains were always found to exhibit a gyroid morphology with enhanced long range order. Disordered gyroids were observed in the spherulitic samples. For these films the electrodeposition was, however, only possible in parts of the film, and the top layer could not be replicated successfully. This indicates that layers of different morphologies are present, which is likely due to break-out crystallisation or a quenched order–order transition. At early stages in the project, lamellar nanostructures were observed individually and in combination with gyroid phases. The temperature control of the experimental set-up was, however, still poor at this point, and ambient fluctuations were not sufficiently shielded. This prohibits a quantitative classification of the results, but it can be concluded that an order–order transition is experimentally accessible. For non-birefringent samples only small domain gyroids were observed. Electron micrographs for each of these cases are shown in Figures 5.2–5.4. It should be noted that for all of these categories a significant proportion of the samples could not be successfully replicated in gold. This is likely caused by preferential wetting at the polymer–substrate interface, and is possibly unrelated to the self-assembly process. The observed surface roughness is likely the result of reorganisation processes, caused by either break-out crystallisation or strong variations in the surface energies.

To confirm the gyroid morphology observed in the SEM measurements, small angle X-ray scattering experiments were performed by J. A. Dolan
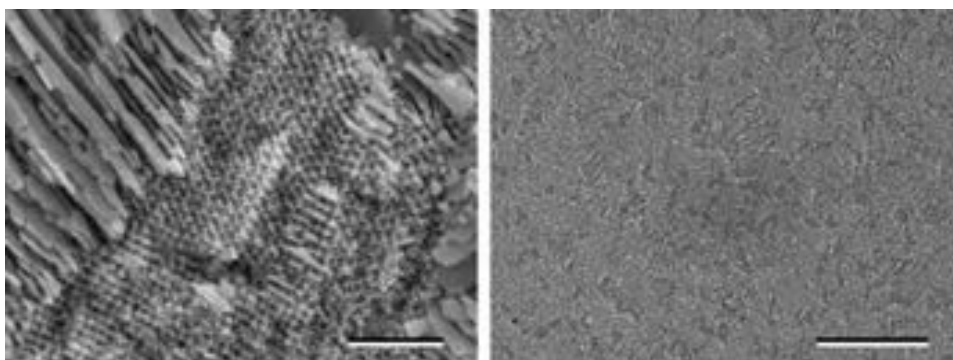
Figure 5.3. SEM micrographs of self-assembled lamellae and gyroids. The coexistence of two different morphologies was observed in a number of samples. This likely results from quenching the sample during an order–order transition. The scale bars are 500 nm (left) and 5 µm (right).
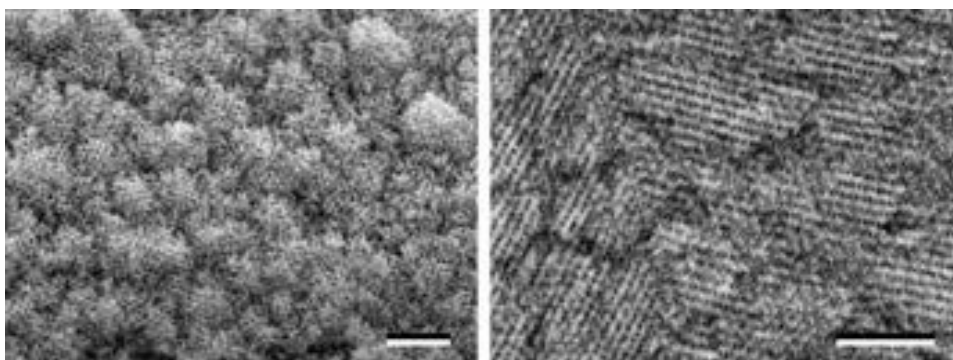

Figure 5.4. SEM micrographs of self-assembled gyroids. The gyroid morphology was observed with (right) and without (left) long range order. Samples were considered long range ordered when the unit cells were aligned across regions significantly larger than 1 µm. The image on the right shows a domain boundary, and the non-uniformity originates from the electroplating procedure. The scale bars are 500 nm.

and A. Sepe. Data analysis was carried out by I. Gunkel, and the results for a polymeric template and the corresponding gold replica are illustrated in Figure 5.6. The scattering patterns are not unambiguous, but the visible peaks imply the presence of periodic structures with cubic symmetry. Only the $I4_132$-symmetry of the single gyroid yields reasonable lattice dimensions when fitted to the data: The calculated unit cell sizes are 85 nm for the polymer templates, and 91 nm for the gold structures, which is in agreement with the dimensions extracted from electron micrographs. The discrepancy between the two dimensions is probably due to a swelling of the polymeric template during the selective polymer removal and the electrodeposition steps.
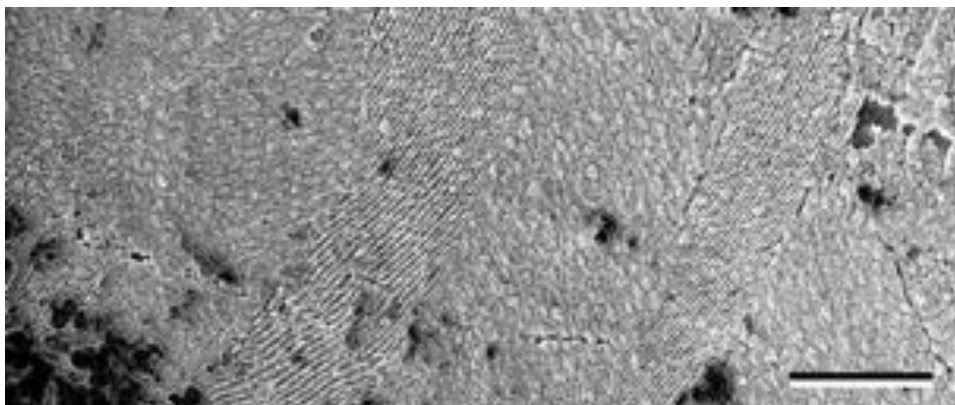
Figure 5.5. Moiré patterns of large gyroid domains. Low magnification electron micrographs undersample the features of the gyroid structures. For well ordered regions this causes moiré patterns, and long range order can be examined via electron microscopy. The scale bar is 10 μm.

As the interferometry had proven unreliable at the swelling ratios of interest, the samples were instead observed with a long working distance microscope during the annealing procedure. These observations revealed, that the polymer films started to slowly dewet from the substrate edges once a certain solvent content was reached. This dewetting could be stopped by further increasing the solvent concentration, and eventually the film started spreading out across the entire substrate again. This counter-intuitive behaviour can be explained by a simple model: The surface energy of the polymer film is higher than that of the substrate, and the increasing solvent content of the film facilitates a dewetting by enhancing its mobility. At the same time the surface energy of the swollen polymer is altered by the increasing solvent content. As the pure chloroform wets the surface, it can be assumed that the interaction between the solvent–polymer mixture and the substrate becomes energetically favourable to a gas–surface interface once a certain solvent content is reached. This can, however, only be the case when the solvent content of the polymer film is higher than the one of the carrier gas.

To investigate the microphase separation at the corresponding swelling ratios, the films were quenched by instantaneously setting the solvent concentration of the inflowing gas to 0 %. This caused a rapid de-swelling of the film, and the thicknesses of the dry films were typically restored within 1–2 minutes. For some of the samples, birefringent structures started to appear several minutes after the de-swelling: Swelling ratios below the dewetting

80
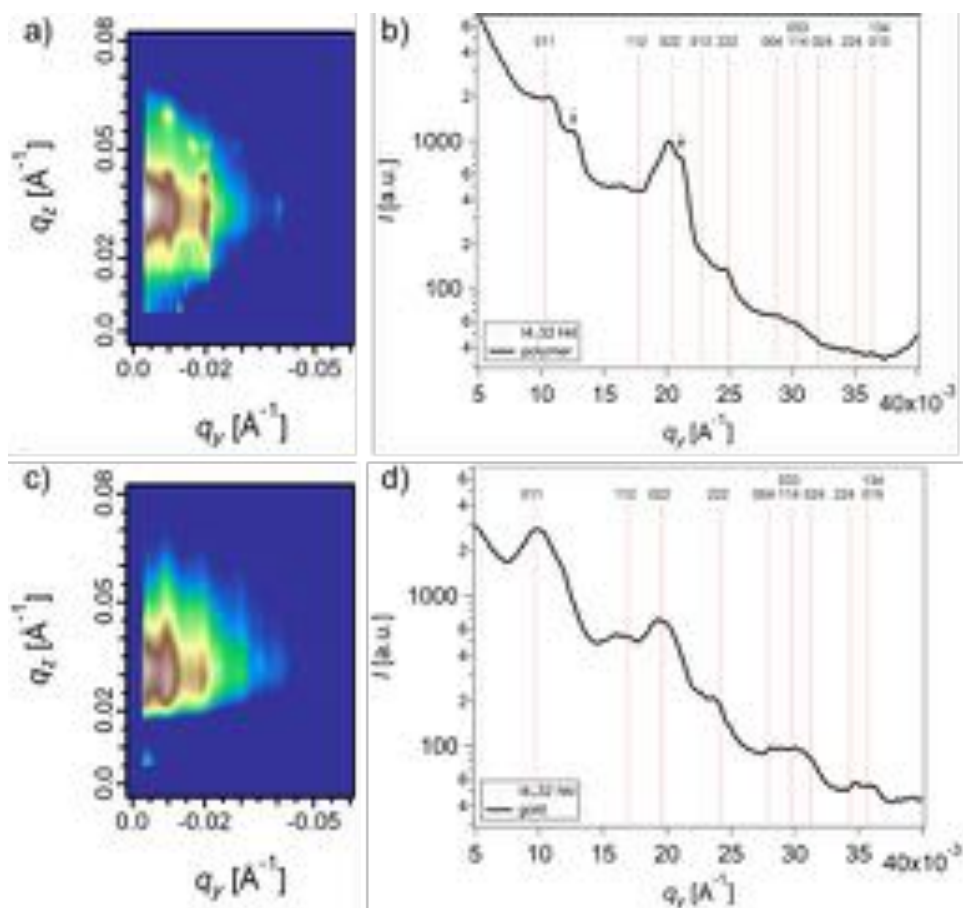
Figure 5.6. X-ray scattering data for polymer templates and gold replica. The 2D scattering intensity is shown for a polymer template (a) and its gold replica (c). The peaks observed in the corresponding intensity profiles (b and d) imply a periodic cubic structure. The single gyroid symmetry can be fitted to the data in a reasonable way, corroborating the conclusions drawn from the electron micrographs. The peaks marked with arrows in b) do not match the expected scattering pattern. This was not investigated further, as they were not observed for the gold replica of the same structure. This figure was created by I. Gunkel.

Figure 5.7. Qualitative phase diagram of the observed birefringent features.
Samples quenched from different solvent contents exhibited the following appearances under crossed polarisers: **a):** For the highest achievable swelling ratios spherulitic Maltese cross patterns were observed. **b):** Large domains were found when samples were quenched from the rewetting regime. **c):** No birefringence was visible in films quenched from the dewetting regime. The microscope image was recorded without polarisers. **d):** At swelling ratios below the dewetting regime spherulitic patterns were observed again. The scale bar is 200 µm.

regime resulted in spherulitic mesostructures, while samples quenched during the dewetting stage exhibited no birefringence. For the rewetting case, however, uniform domains occurred, and for significantly higher swelling ratios spherulites were observed again. No quantitative description of these four regimes is given here, as the concentration and swelling ratio required to trigger the dewetting and rewetting effects varied significantly between different samples.

Despite these fluctuations the relative position of the four described regimes in the parameter space remained reproducible, as illustrated by the diagram shown in Figure 5.7. This finding allows a reliable sample fabrication by first identifying the solvent concentration required to reach the rewetting regime, and then maintaining the corresponding swelling ratio for a certain time. The onset of the dewetting is a useful indicator for a mobility that is sufficient for reorganisations on experimentally accessible time scales. The absence of long range order in films quenched from this state could be due to the deviation of the resulting structures from the thin film geometry. The formation of the long range order in the rewetting films implies that the solvent content here is high enough to facilitate swift reorganisations, and at the same time still too low to fully suppress microphase separation. It is unclear at this point what the dominant morphology in this situation

82
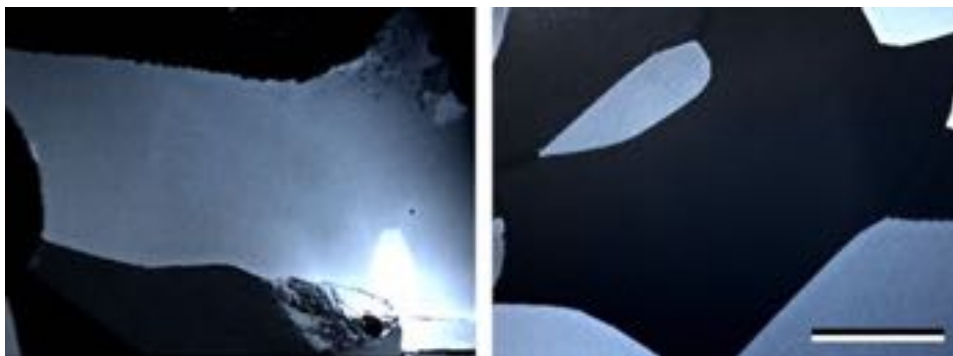
Figure 5.8. Millimetre scale long range order in gyroid structures. Crossed polarisation optical micrographs of the two largest domains observed in this work, recorded in transmission. Both domains have sizes of approximately $2 \times 1\,\text{mm}^2$ The scale bar is 500 μm.

is. Either the gyroid is formed directly, or an intermediate lamellar phase occurs that is transformed into gyroid structures during the quench step. The latter hypothesis is weakly supported by the previous observation of lamellar structures via electron microscopy, and by the fact that the gyroid unit cells are oriented with the (110) direction out of plane for all samples with long range order.

The experimental results obtained for higher and lower swelling ratios can be explained in a consistent way: For swelling ratios below the dewetting regime the mobility of the polymer chains is too low for large scale reorganisations. If, on the other hand, the solvent content is increased beyond the onset of rewetting the segregation strength decreases, and the microphase separation will eventually be suppressed. During the quench, the microphase separation briefly becomes favourable, the limited time frame, however, prevents the formation of long range order.

The presented hypotheses will be probed in upcoming *in-situ* scattering experiments by I. Gunkel, J. A. Dolan *et al.* With the high intensity X-ray beam of a synchrotron, the morphology of the microphase separation can be examined during solvent exposure with a time resolution on the scale of seconds. An experimental set-up for this purpose was designed and tested by I. Gunkel and the author.

5.2.2 Goniometry on Single Domain Gold Gyroids

The successful annealing of large domain gyroid films facilitated the fabrication of gold samples suitable for optical characterisation. The aim was
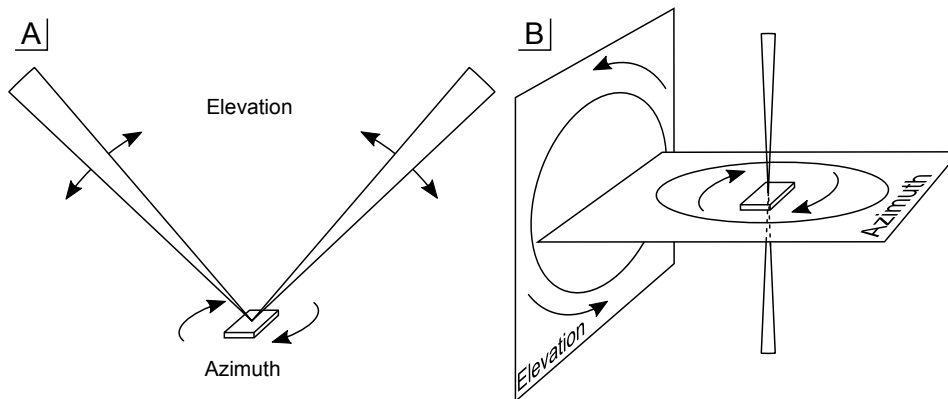
Figure 5.9. Schematic of the reflection and transmission goniometers. A: During the reflectance measurements the elevation angle was varied by adjusting the illumination and detection angles in equal ways. The schematic is a simplification, and in the experiments the illumination angle was varied by tilting the sample by an angle θ while the detection arm was tilted by 2θ. The azimuthal angle was adjusted by rotating the sample in-plane. B: For the transmission measurements the beam path was fixed, and the elevation and azimuthal angles were varied by rotating the sample around two perpendicular axes.

to obtain a comprehensive data set, which facilitates the modelling of the anisotropic optical response of the gold gyroid. This is motivated by the assumption that the gyroid is an optical metamaterial, and that its optical properties are equivalent to the ones of an effective homogeneous medium with dielectric permittivity $\varepsilon_{\text{eff}}(\omega)$ and magnetic permeability $\mu_{\text{eff}}(\omega)$. The previously reported linear and circular dichroism of gold gyroids — and in particular the angle of incidence dependence of these effects — implies that the material is optically anisotropic, and that $\varepsilon_{\text{eff}}(\omega)$ and $\mu_{\text{eff}}(\omega)$ are not scalars, and might be approximated by tensors to reasonable accuracies instead. If these tensors are known, the reflectance and transmittance for incident light can be calculated for each angle of incidence and polarisation state. Models for $\varepsilon_{\text{eff}}(\omega)$ and $\mu_{\text{eff}}(\omega)$ can therefore be developed and validated with increased accuracy if a large number of data points across a wide range of illumination angles are considered.

To provide a suitable set of data points, goniometric measurements were conducted in reflection and transmission. In both cases a set-up is required that allows the precise control of the polarization state of the incident light, the illumination angle, and the detection footprint, i.e. the area of the sample that contributes to the recorded spectrum.

For the reflectance measurements a set-up with a fixed illumination arm
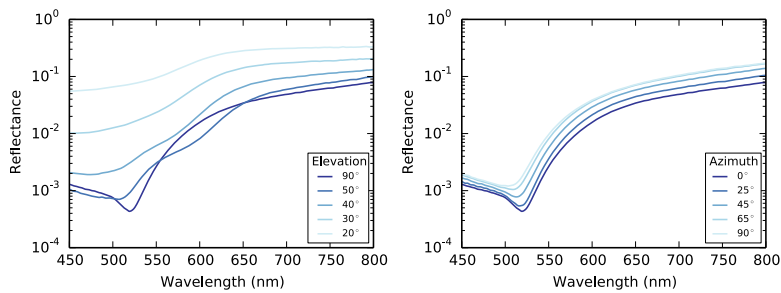
Figure 5.10. Reflectance spectra for parallel polarisers. Left: Elevation series of spectral reflectance at an azimuthal angle of 0°. Right: Azimuth series of reflectance at an elevation angle of 90°. The incident light was p-polarised in all cases.
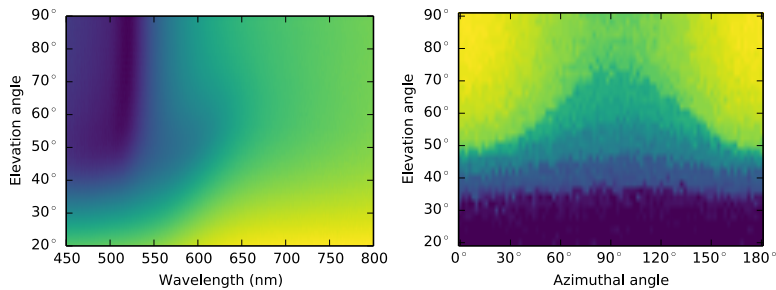

Figure 5.11. Visualisation of multidimensional data. Left: Heat map of the reflectance depending on illumination wavelength and elevation angle (azimuthal angle = 0°). Right: The wavelength of minimal reflectance for each recorded spectrum. The colour scale ranges from 450 to 520 nm.

was utilized. The sample and the detection arm were in the θ–2θ configuration: whenever the sample was tilted by an angle θ, the detection arm was tilted by an angle 2θ. The set-up was carefully aligned, such that the specular reflection was recorded for all tilt angles. This alignment was particularly challenging, as the rotation axes of the sample mount and the detection arm have to coincide with each other and the sample surface to narrow tolerances. To ensure that only a single domain contributes to the recorded spectra the illumination beam was focused onto the substrate. The signal was recorded by coupling the reflected light into an optical fibre connected to a spectrometer. This set-up facilitates the scanning of the elevation angle at a fixed azimuthal angle. To scan the azimuthal angle the sample had to be rotated around its surface normal with the corresponding rotation axis centred in the domain of interest. This imposes further constraints on the alignment of the set-up, as the sample has to be mounted on a rotation stage in a predefined position. The polarisation was controlled by inserting the desired polarisers into the illumination and detection beam paths. Reflectance spectra
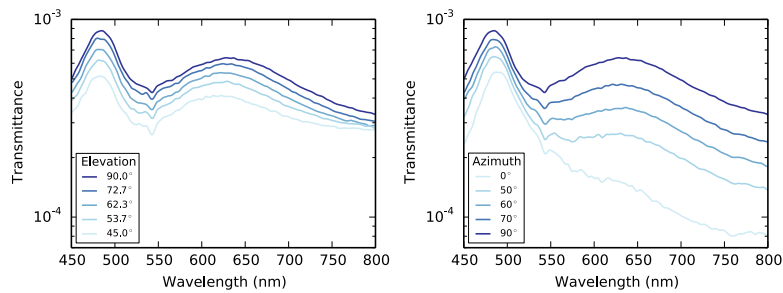
Figure 5.12. Transmittance spectra for parallel polarisers. Left: Elevation series of spectral transmittance at an azimuthal angle of 90°. Right: Azimuth series of transmittance at an elevation angle of 90°. The light was p-polarised in all cases.
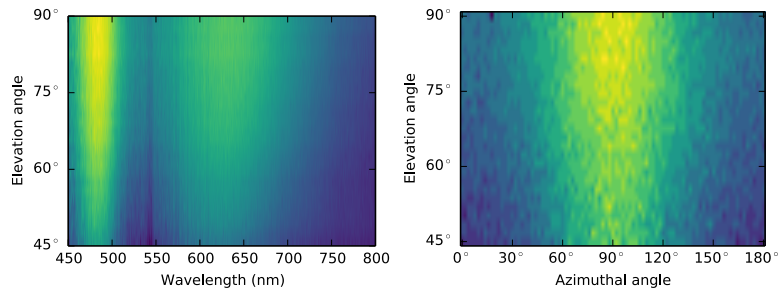

Figure 5.13. Visualisation of multidimensional data. Left: Heat map of the transmittance depending on illumination wavelength and elevation angle (azimuthal angle = 0°). Right: The wavelength of maximal transmittance for each recorded spectrum. The colour scale ranges from 480 to 490 nm.

could be recorded at elevation angles between 20 and 90° in 2°-steps in an automated way. For each of these steps, the azimuthal angle was scanned across a half turn (180°, 2°-steps). The entire procedure was repeated for the following polarisation conditions: s– and p–polarisations were measured with crossed and parallel polarisers each, and right handed and left handed circularly polarized light were measured with right handed and left handed analysers each. Selected reflectance spectra are shown in Figure 5.10. The elevation and azimuthal angles were chosen to represent the full recorded range. The entire elevation series is shown in Figure 5.11, along with a visualisation of the linear dichroism: As a preliminary data analysis the wavelength of minimal reflectance was determined for each spectrum. The plot shows that the reflected spectrum depends significantly on the angle of incidence. The data is especially convincing for the azimuthal series, as the expected periodicity is clearly visible.

Transmittance measurements were carried out in a separate set-up. The beam path here is a straight line, which allows the use of a standard op-

tical microscope for illumination and detection. A sample stage, capable of rotating a sample around two perpendicular axes, was designed by J. A. Dolan and manufactured by S. Drewitt (Department of Engineering). Linear translation stages were incorporated into this design in such a way that the intersection of both rotation axes and the sample surface could be moved into the focal plane of the microscope objective.

To ensure that only light transmitted through the intersection of the rotation axes was recorded the detection fibre had to be temporarily disconnected from the spectrometer. Instead, a light source was connected, and the light emitted at the other end of the fibre was focused onto a small spot in the rotation centre. This implies that regardless of the elevation and azimuthal angles the spectra were always recorded from the same area on the substrate. Here, the positioning of the sample on the stage is a challenge, as the detection area should be centred in a single domain. This set-up was geometrically confined to elevation angles below approximately 45°, as the sample mount would either obstruct the beam path or collide with the objective for larger angles. Analogous to the reflectance goniometer, the polarisation configuration could be adjusted by adding polarisers to the illumination and detection beam paths.

Measurements were conducted in a fully automated manner, as both sample rotation axes, as well as polariser and analyser were motorised. A 180° azimuthal scan was conducted in 2°-steps for each elevation angle between 45 and 90° (1.73° increments). The polarisation states probed were equivalent to the transmission measurements: Crossed and parallel s– and p–polarizations, and equal and opposite handedness for right and left handed polarisations.

The transmittance data is presented in Figures 5.12 and 5.13 analogous to the reflectance data: Representative spectra are shown, indicating the spectral variations along tilt and rotation, and the wavelength of maximal transmittance is plotted for all spectra. Each spectrum exhibits a small intensity dip at 546 nm, which is likely related to the mercury line emitted by the laboratory lighting. The wavelength of maximal transmittance varies only slightly in the presented dataset. The shift is, however, clearly detectable, and the observed periodicity is as expected. To illustrate the linear dichroism of the samples, the recorded spectra were converted to RGB colours. This was achieved with the *ColorPy* python package, which was de-
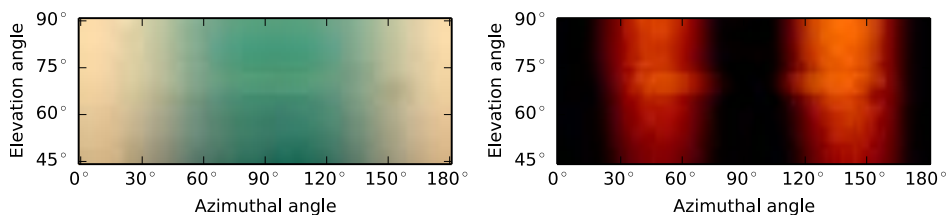
Figure 5.14. RGB colour representation of the recorded spectra. Left: Colour values in transmission for p-polarised light with parallel polarisers. Right: Colour values in transmission for p-polarised light with crossed polarisers. The colour transitions for parallel polarisers coincide with the regions of increased transmission in the case of crossed polarisers. Both data sets exhibit discontinuities along the elevation axis between 68 and 74°. A possible reason for this is a specular reflection of ambient light. The brightness of the images was enhanced to improve the visibility of the features.

veloped by Mark Kness based on the light receptors of the human eye.[141] The linear dichroism of the reflectance spectra (not shown) is much less striking than what can be seen in transmission (see Figure 5.14).

5.3 Conclusion

In summary, a fabrication pathway for thin films of gold single gyroids with near-millimetre scale long range order was developed, and the resulting samples were characterized optically.

A reliable solvent vapour annealing protocol for the template fabrication was developed, aided by the correlation between distinct birefringent features and the long range order of the microphase separation. The underlying mechanisms, however, remain ambiguous, and further investigation is required to fully explain the observed phenomena. It is unclear whether or not the enhanced long range order is formed in an intermediate lamellar phase. Another open questions is why the (110)-axis of the long range ordered gyroid structures is always normal to the substrate surface. These questions are likely related, and *in-situ* scattering experiments have been scheduled and prepared to shed some light on the matter. The preferential out of plane orientation is of particular interest for goniometric measurements, as control over this parameter would extend the range of accessible angles of incidence.

Another inscrutable observation is the fluctuation of the annealing conditions required for the formation of long range order. Significant effort was undertaken to prepare and anneal the samples in identical ways, but the

results remained highly variable. At this point it can only be speculated that ambient humidity during sample preparation and storage has a strong influence on the hygroscopic PEO block. Also, it can not be stressed enough how critical the tight control of the temperatures of the solvent reservoir, the annealing chambers, and the gas lines between the two is for the reproducibility of the resulting vapour pressure. Finally, it is likely that the interior surface roughness of the annealing chamber determines the solvent condensation rate, which can influence the vapour pressure during the annealing step, as well as the drying rate during the quench step.

For the goniometric measurements two separate experimental set-ups have been developed. Automated data acquisition at high precision is of utmost importance here, as a large number of measurements have to be conducted on a small region ($\ll 100\,\mu\text{m}$) on the sample surface. The experimental data from the first measurements shows that the spectra are recorded reliably and to sufficient precision. Aside from tedious alignment protocols the procedures are fully automated, and samples can be characterized in a reproducible way.

Only qualitative conclusions can be drawn from the data at this point. Linear dichroism is apparent in all recorded data sets, and in transmission it is directly visible (see Figure 5.14). The azimuthal series have periods of 180°, which implies a strong optical anisotropy of the gold structures. This is a further verification of the measurement precision, as significant contributions from differently oriented domains would appear in the azimuthal series as additional features with a random offset. The variations in the elevation series have to be analysed more carefully. They could be caused by optically anisotropic structures, but alternative explanations such as surface roughness effects can not be ruled out.

The next step in this project is the development of a theoretical model, capable of explaining the observed phenomena. Of particular interest is the extraction of an effective plasma frequency from each spectrum, as this would allow a precise quantification of the angular dependence of the optical response. J. A. Dolan is working on this highly complex project in collaboration with the Hess group (Imperial College London).

5.4 Materials and Methods

Sample preparation was carried out as described in Section 3.1. Soda lime glass coated with fluorine doped tin oxide (FTO) and silicon wafers were used as substrates. The FTO was piranha etched and silanised, and the silicon substrates were only piranha etched. Poly(isoprene)-*block*-poly(styrene)-*block*-poly(ethylene oxide)[1] was dissolved in anisole[2] ($10\,\%$ by weight). Thin films were prepared via spin-coating: Approximately $7\,\mu l/cm^2$ of the polymer solution were manually spread out on the substrate before the spin-coater was accelerated to $1200\,\mathrm{rpm}$ (acceleration: $100\,\mathrm{rpm/s}$, duration: $60\,\mathrm{s}$).

The experimental set-up used for solvent vapour annealing is described in detail in Section 3.2.2. Section 3.3.2 explains the interferometry based thickness measurements.

The replication of the polymer samples into free-standing nanostructured gold films is described in Sections 3.2.3–3.2.5. Electrodeposition was carried out using a potentiostat[3] with a saturated calomel reference electrode and a gold-coated stainless steel counter electrode. A commercial plating solution was used[4], and the deposition was nucleated by a cyclic voltammetry between $0\,\mathrm{V}$ and $-1.2\,\mathrm{V}$ (1 full cylce, $0.5\,\mathrm{V/s}$). The deposition was carried out at $-0.8\,\mathrm{V}$ until the desired deposition charge density was reached.

GISAXS data was recorded at the beamline D1 of the Cornell High Energy Synchrotron Source (CHESS), Cornell University, New York (USA). The sample to detector distance was $1820\,\mathrm{mm}$, as determined via calibration with a silver behenate standard. The photon wavelength was $1.162\,\mathrm{\AA}$, and a CCD detector was was used to record the scattering patterns[5]. Data analysis was carried out with the *Nika* software[142] in IGOR Pro[6].

Reflectance and Transmittance spectra were recorded with a high sensitivity CCD-array spectrometer[7]. Linear polarisation was obtained with polaroid sheets[8], and circular polarisation was created by combining a lin-

---

[1]$M_W = 80\,\mathrm{kg/mol}$, $f_I = 30\,\%$, $f_S = 53\,\%$, $f_{PEO} = 17\,\%$, sythesized by Y. Gu

[2]ReagentPlus® grade, Sigma Aldrich, Dorset

[3]AUTOLAB PGSTAT302N, Metrohm Autolab B.V., Utrecht (Netherlands)

[4]ECF60 with E3 brightener ($0.5\,\%$ by volume), Metalor Technologies Ltd., Birmingham

[5]Medoptics CCD, Medoptics Corporation, Arizona (USA)

[6]IGOR Pro 6, WaveMetrics Inc., Oregon (USA)

[7]QE65000, Ocean Optics, Florida (USA)

[8]HN22, Knight Optical Ltd., Kent

ear polariser with a quarter wave plate[9]. The sample holder[10] and detector arm were moved via motorized rotation stages[11] in the reflectance measurements. Here, the samples were illuminated with a xenon light source[12]. In the transmittance goniometer the sample was tilted and rotated with geared stepper motors, powered by a computer controlled driver board[13]. The polarisation state could be automatically adjusted with motorized rotation mounts[14]. An optical microscope with its standard light source was used for illumination[15], and the transmitted light was coupled into a fibre via a $5\times$ objective[16].

---

[9]HNCP37, Knight Optical Ltd., Kent
[10]SGSP-60YAW-0B, SIGMA KOKI, Tokyo (Japan)
[11]INSERT SGSP-120YAW, SIGMA KOKI, Tokyo (Japan)
[12]HPX-2000-HP-DUV, Ocean Optics, Florida (USA)
[13]Stepper Bee+, PC Control Ltd, Northamptonshire
[14]PRM1Z8, Thorlabs Ltd., Ely
[15]BX-51, Olypmus Corporation, Tokyo (Japan)
[16]LMPlanFL N, Olypmus Corporation, Tokyo (Japan)

6

Aligned Crystallisation in Tricontinuous Polymer Matrices

The work presented here is being prepared for publication by Raphael Dehmel*, James A. Dolan*, Bodo D. Wilts, Alessandro Sepe, Yibei Gu, Ulrich Wiesner, Ilja Gunkel and Ullrich Steiner.

A set of remarkable findings on semicrystalline block copolymer films is presented and discussed in this chapter. The principal observation is, that thin films of gyroid forming poly(isoprene)-b-poly(styrene)-b-poly(ethylene oxide) (ISO) exhibit areas of uniform birefringence after certain solvent vapour annealing procedures. Further examination of the samples revealed that these areas of uniform birefringence are due to preferentially aligned crystallisation of the ethylene oxide block, and occur only when the copolymer self-assembles into a gyroid morphology. Finally, it is shown that the crystal domains and the domains of microphase separation coincide spatially, which implies a strong correlation between the orientations of the crystallites and the surrounding microphases.

---

*J. A. Dolan and R. Dehmel contributed equally to this work.

6.1 Introduction

For many solids the energetically most favourable state is reached when all molecules or atoms are arranged in a close-packed periodic structure — a crystal. Aside from their often attractive optical appearance, crystalline materials can exhibit a variety of outstanding mechanical and electronic properties that make them interesting for a vast range of applications. Modern semiconductors, for example, are based on silicon single crystals, which are produced from amorphous material on industrial scales.

For atoms and small molecules the crystallisation process is well understood, and a sufficiently slow solidification of a given material often yields crystals with extended volumes of continuous uniform alignment — so-called domains. For polymers, however, the situation is more complex, as the repeat units are interconnected via covalent bonds and form coiled and entangled chains. These bonds are much stronger than the interaction between unconnected repeat units, which makes the equilibrium spacing between adjacent monomers distinctly lower along the polymer axis. In a crystal these spacings have to be uniform in each direction, which implies that the polymer chains have to assume straight conformations and align parallel to each other to form a crystal. The drastic entropy reduction associated with the stretching of a polymer chain prevents complete crystallisation of the material, and crystallising polymers are generally referred to as *semicrystalline.*

The growth of polymer crystals is highly anisotropic: The crystal can only grow along the chain axes by further straightening all constituent polymers. The lateral crystal growth is not intrinsically limited, and it depends mainly on the mobility of the polymer chains[143] In practice, lamellar sheets are typically formed with a thickness limited to fractions of the polymer contour length.[144, 145] Individual chains are typically folded, traversing the lamellar sheet several times. The fold sections, as well as the polymer ends remain amorphous, and each crystalline slab is covered with amorphous material on two opposing surfaces.

Further constraints are imposed on the crystallisation when a block copolymer is considered, where one of the blocks can crystallise while the others remain amorphous. Here, a competition arises between the driving forces of the microphase separation and the crystallisation. The two processes are not mutually exclusive, but numerous studies have shown that they strongly

influence each other. The interplay between crystallisation and microphase separation depends crucially on the relation between the crystallisation temperature T_c of the crystalline block and the glass transition temperature T_g of the amorphous block[1]. For $T_c < T_g$ the vitrified amorphous block imposes a so-called *hard confinement* on the crystallisation. The semicrystalline chains are tethered to fixed points, and the crystal growth is limited to the rubbery microphase. A similar situation arises for $T_c > T_g$ when the segregation of the microphase separation is stronger than the driving force of the crystallisation. For many copolymers this is, however, not the case, and $T_c > T_g$ causes *soft confinement.* These circumstances usually favour *break-out crystallisation*, where the microphase separated morphology is overwritten by the crystal morphology. The growth kinetics here are often similar to the unconfined case, and identical mesostructures are typically formed: Lamellar sheets start growing from individual nucleation sites in a radial pattern, and a circular growth-front emerges. The anisotropic repeat-unit spacing within the lamellae causes optical anisotropy and birefringence, which can be visualised under crossed polarisation. In this configuration the crystals will appear dark when either of their optic axes are parallel to the polarisation axis of the incident light. The radially arranged lamellae will thus exhibit two dark axes which intersect in the nucleation site, and with the bright areas between these axes a characteristic Maltese cross pattern is formed. Due to their spherical growth front the crystal superstructures are named *spherulites*.

In the hard-confined case the crystal growth is significantly constrained, and in particular the crystallisation kinetics and the resulting degree of crystallinity depend on the confining geometry.[146–151] The influence of hard confinement on the orientation of the crystallites has been studied for lamellar[152, 153] and cylindrical[154, 155] morphologies. In all cases the angle between the crystal stems and the glassy interfaces could be tuned between 0° and 90° by varying the crystallisation temperature. Similar findings have been reported for hexagonally perforated lamellae.[156] Hard-confined crystallisation in gyroid morphologies has also been investigated previously.[148, 150, 157] However, no preferential alignment of the crystallites has been reported so far.

---

[1]For semicrystalline block copolymers with more than one amorphous block the highest T_g is relevant here.
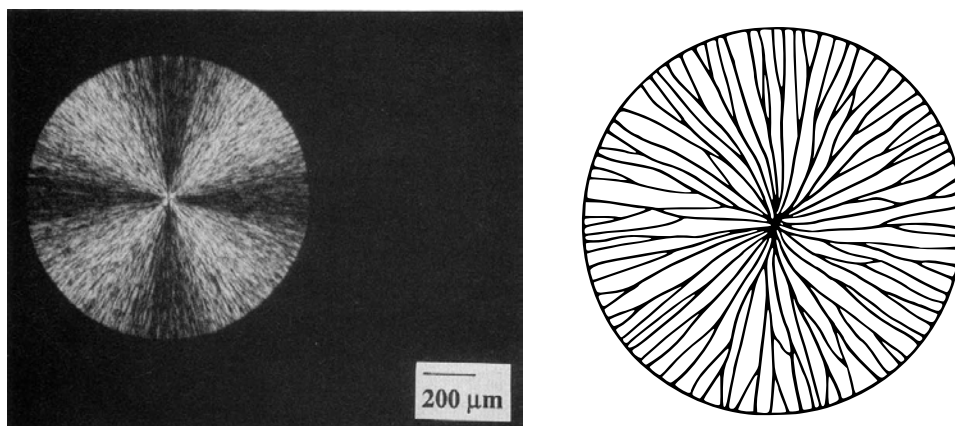
Figure 6.1. Spherulitic mesostructures in polymer crystals. Left: Optical micrograph of semicrystalline PEO recorded under crossed polarisation. The Maltese cross pattern and the circular growth front are clearly visible. Right: Schematic of the orientation of the corresponding lamellar crystals. This Figure was taken from a publication by J. M. Marentette *et al.*[140]

Instead, the crystal orientation has been examined in two gyroid forming systems under soft confinement.[158, 159] The gyroid morphology is replaced by crystalline lamellae via break-out crystallisation in both cases. Remarkably, the lamellar sheets are oriented in certain lattice planes of the previously self-assembled gyroid structure.

The influence of solvents on the interplay of crystallisation has not been investigated extensively so far. The available studies generally report a strong increase in the polymer mobility, and faster crystal growth is observed.[160] The increased mobility also allows different crystallite orientations, and with selective solvents the balance between crystallisation and microphase separation can be shifted.[161, 162]

In this chapter, the influence of solvent vapour annealing on the alignment of the crystallites with respect to the glassy microphase separated structures is studied in ISO triblock copolymers. Well ordered gyroid films are found to exhibit large areas of uniform birefringence. The birefringence can be attributed to the semicrystalline poly(ethylene oxide) (PEO), and preferentially aligned crystallisation was confirmed. Finally, the regions of ordered microphases and preferentially aligned crystallisation were found to overlap perfectly, which suggests that the crystal orientation is strongly influenced by the orientation of the surrounding microphase.

6.2 Results and Discussion

Thin films of ISO polymer were exposed to controlled solvent vapour atmospheres to study the interplay between the microphase separation and the crystallisation of the PEO block. Nitrogen gas rich in chloroform vapour was fed into a sealed annealing chamber, causing the polymer film to swell significantly. In a typical experiment a predefined swelling ratio was held for a certain time before the film was dried by introducing dry nitrogen gas. The resulting film morphology was found to be highly sensitive to a variety of parameters, and only after precise control over the temperature of the annealing chamber, the gas lines and the solvent reservoir was established, the experiments became reproducible (see Chapter 5).

6.2.1 Microphase Morphology

Scanning electron microscopy (SEM) was used to characterise the microphase morphology. For this purpose, the isoprene phase was replicated in gold, as described in Sections 3.2.3–3.2.5. This facilitates electron microscopy with excellent contrast, as shown in Figure 6.2. Two different regions with uniform porosity on the nanometre scale are visible in the image. The hexagonal (top right) and square (bottom left) arrangements of the pores are expected for a single gyroid network viewed from the (111) and (100) directions, respectively. The viewing angle with respect to the surface normal was approximately 45°. The observed unit cell projections are thus consistent with a (110)-axis orientation perpendicular to the substrate, which was observed for all samples with long range order.

The microphase separated morphology was also characterised using grazing incidence small angle X-ray scattering (GISAXS). The scattering patterns shown in Figure 5.6 confirm the presence of gyroid structures in the polymeric templates with unit cell sizes of 85 nm. It can therefore be assumed that the polymer self-assembles into a double gyroid morphology, where the isoprene and ethylene oxide phases form single gyroid networks, separated by a styrene matrix.

6.2.2 Birefringent Mesostructures

Figure 6.3 shows the two distinct patterns of birefringence that were observed in the annealed films: Spherulitic Maltese cross patterns and ex-
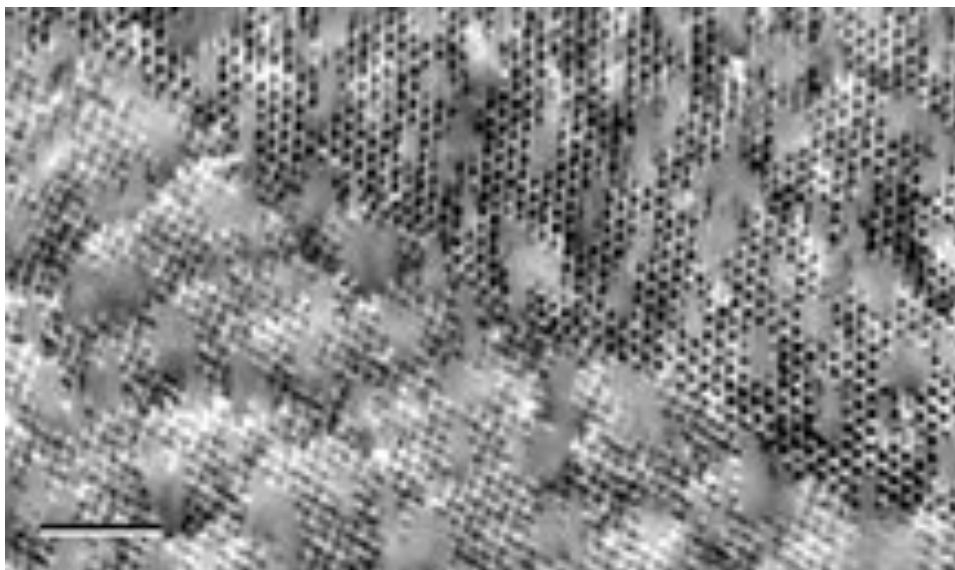
Figure 6.2. SEM image of the gold replication of the poly(isoprene) microphase. The gold is structured in a regular morphology with highly uniform pore sizes. Two domains with different appearances are visible. The pore patterns observed in the top right and the bottom left are consistent with the (111) and (100) projections of a single gyroid, respectively. The flakes at the film surface are artefacts from the electrodeposition procedure. The sample was mounted on a surface with an inclination of $45°$ for imaging. The scale bar is 500 nm.

tended regions of uniform birefringence. While the spherulites were readily obtained for a variety of annealing protocols, the uniform domains could only be fabricated under certain conditions. Here, the focus lies on the characterisation of the birefringent superstructures, while the relevant annealing procedures are discussed in detail in Chapter 5.

Spherulitic growth patterns are commonly observed in semicrystalline homopolymers and block copolymers. Here, they are likely caused by a break-out crystallisation of the PEO block, which is the only crystallisable material in the examined system. Domains of uniform birefringence, on the other hand, have only been reported for non-polymeric, fully crystalline materials so far. Several experiments were carried out to further characterise the material and to determine the nature and origin of the birefringence.

6.2.3 Crystal Melting

Differential scanning colorimetry (DSC) was performed as described in Section 3.3.1 to determine the temperatures of the glass transitions, the crstal melting and the crystallisation. Figure 6.4 shows DSC data for the ISO co-
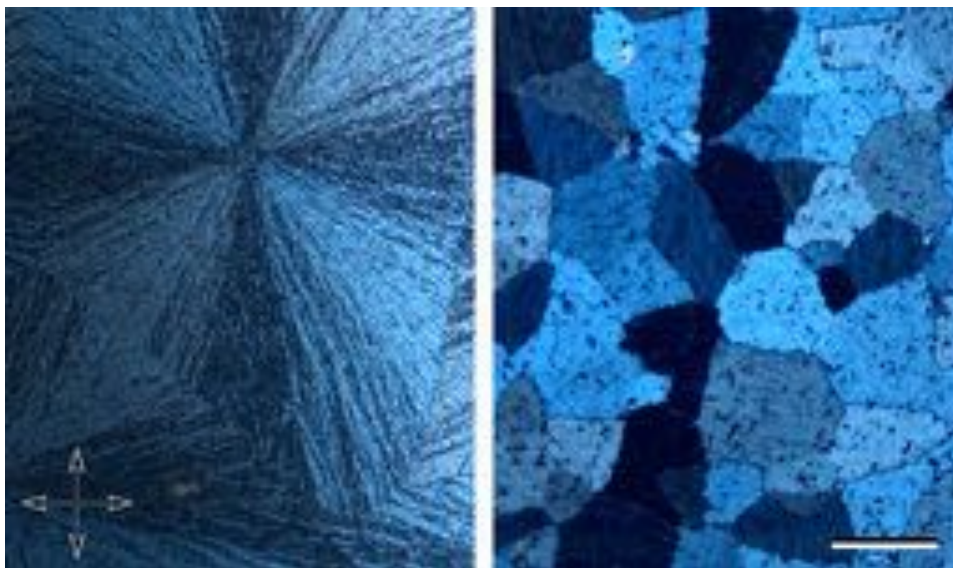
Figure 6.3. Birefringent structures in thin ISO films. Solvent vapour annealing of thin ISO films yields two distinct types of birefringence patterns. The optical micrographs were recorded under crossed polarisation, and show spherulitic Maltese crosses (left), and patterns of uniform domains (right). The crossed arrows indicate the orientation of the polarisers. The scale bar is 200 μm.

polymer. The peaks at $55\,°\mathrm{C}$ during heating and at $30\,°\mathrm{C}$ during cooling are consistent with values previously reported for melting and recrystallisation of PEO.[153] A shallow polystyrene glass transition can be seen around $80\,°\mathrm{C}$ in a magnified section of the plot. This glass transition is spread across a wide temperature range, and it is unclear whether or not the material is still fully vitrified when the crystal melting is completed. Moreover, the presence of a solvent will have a strong influence on both processes, and it can be assumed that both temperature ranges are shifted to lower values. The shifts are unlikely to be exactly equal, implying that the styrene block could be in a rubbery state while the ethylene oxide crystallises.

The presence of crystalline PEO in the thin ISO films could be confirmed by grazing incidence small angle X-ray scattering experiments (GIWAXS). Measurements on samples with domains and spherulites were carried out by C. Zhu, and the data was analysed by I. Gunkel. The recorded scattering patterns are shown in Figure 6.5, and two strong peaks are observed at the expected q-values for the (120) and (032) PEO reflections.[163, 164] A third peak around $q = 1.9\,\text{Å}^{-1}$ originates from the FTO substrate, as confirmed in a reference measurement (not shown). The azimuthal distribution of the (120) reflection shows significant anisotropy: For the spherulitic sample a

98
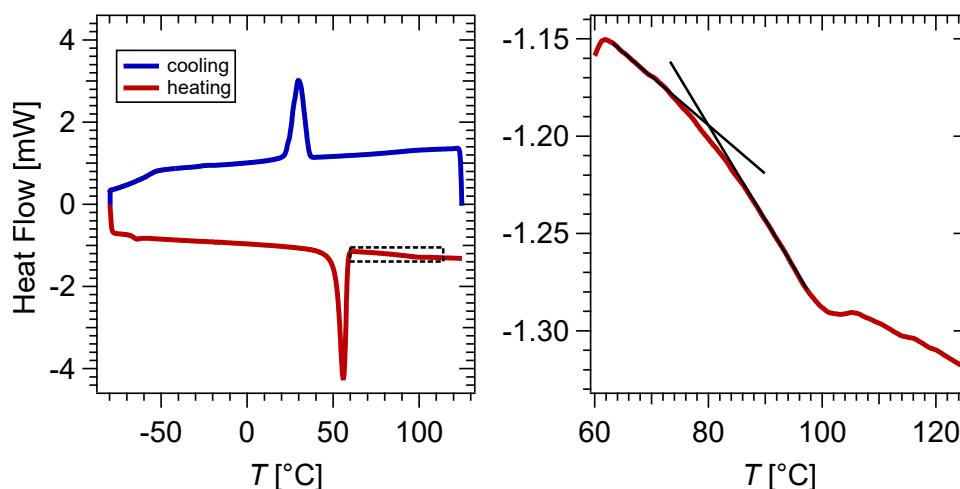
Figure 6.4. Differential scanning calorimetry of ISO copolymer. The DSC scans were carried out at a heating and cooling rate of 10 K/min. Left: Crystal melting and recrystallisation peaks are clearly visible at 55 °C and 30 °C, respectively. Right: A magnification of the region between 60 °C and 120 °C indicates an extremely wide glass transition around 80 °C. This figure was created by I. Gunkel.

single peak at 90° is clearly visible, which implies that the polymer chains in the crystals are mainly parallel to the substrate.[152] For the domain sample two additional peaks at 50° and 135° emerge, indicating three distinct directions of preferential crystallite alignment.

To investigate the causality between the crystallinity and the birefringence, melting experiments were carried out on several samples. A heating chamber with transparent windows was used for this purpose, facilitating the *in-situ* observation of the birefringence via optical microscopy. The samples were heated at a rate of 15 K/min, and the birefringence disappeared between 53 and 55 °C (compare Figures 6.6A and B). This is in line with the PEO crystal melting temperature in the ISO block copolymer, as determined via differential scanning calorimetry. The samples were kept at 55 °C for 1 minute, after which the heating element was deactivated and the samples cooled down. At a temperature of approximately 40 °C the birefringence began to reappear, and below 26 °C no further changes were visible. Figures 6.6A and C show the film before and after heating, and apart from an increased defect density the domain patterns are identical. In combination with the observed melting and recrystallisation temperatures this is a strong indication for the crystalline origin of the birefringent mesostructures. Equivalent experiments were conducted on spherulitic samples, and the same behaviour was observed. The origin of the increased defect
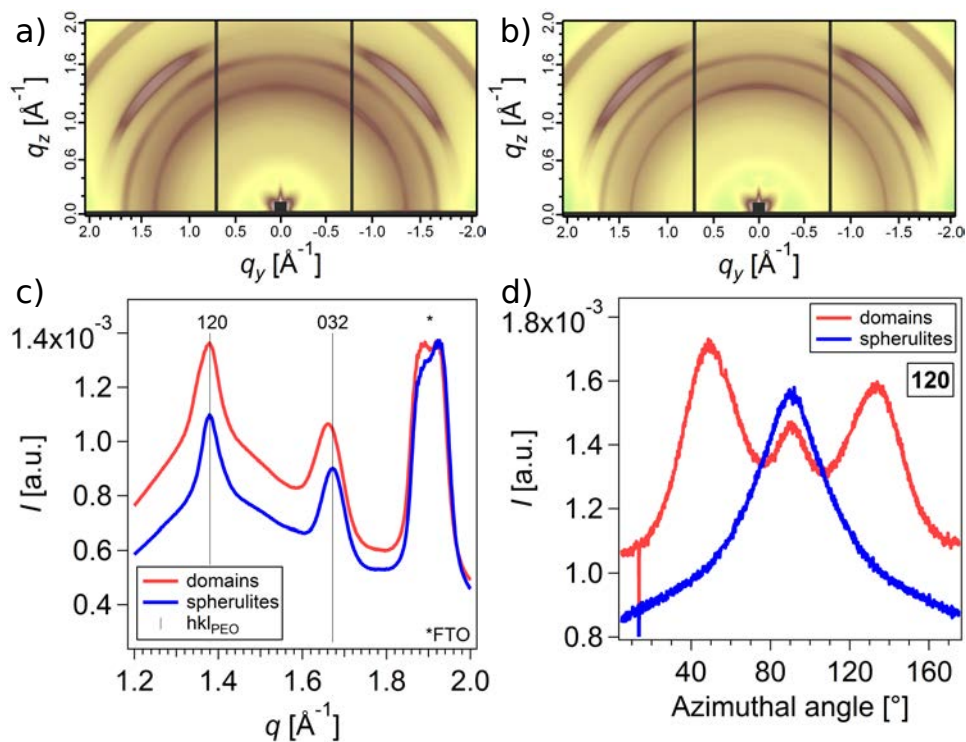
Figure 6.5. X-ray scattering data for polymer crystallites in birefringent meso-structures. This figure shows 2D GIWAXS patterns for polymer films with domains of uniform birefringence (a) and spherulitic Maltese cross patterns (b). Also shown are azimuthally averaged data vs. the q-vector (c), and the intensity of the (120)-peak vs. the azimuthal angle (d). The characteristic PEO (120) and (032) reflection peaks are clearly visible. The signal at $\approx 1.9\,\text{Å}^{-1}$ is caused by the FTO substrate. The uneven intensity distribution of the (120) signal along the azimuthal rotation implies an anisotropic orientation of the crystallites.[152] This figure was created by I. Gunkel.
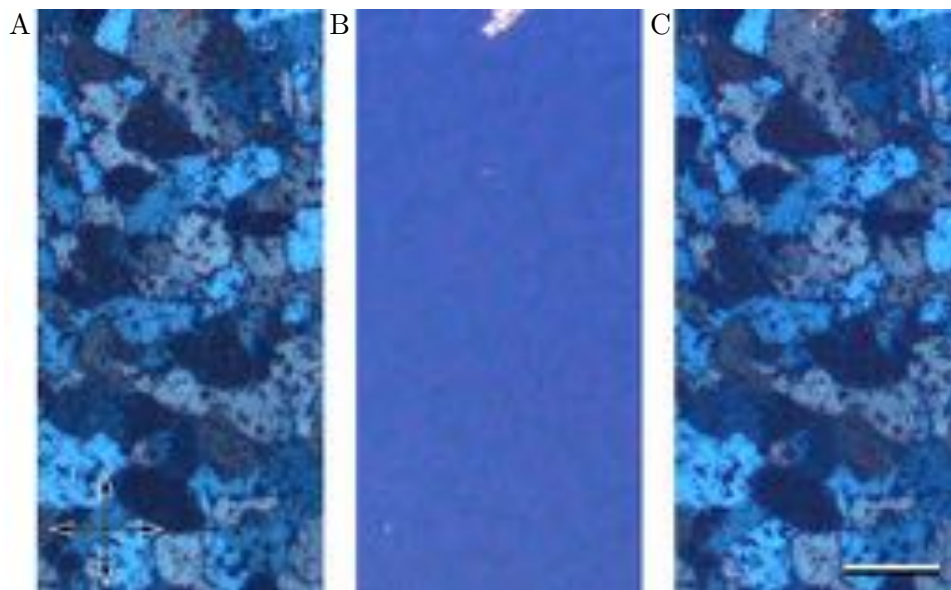
Figure 6.6. Melting and recrystallisation of poly(ethylene oxide). Crossed polarisation optical micrographs of a thin film of ISO on silicon. **A:** Before heating, areas of uniform birefringence are clearly visible. **B:** At a temperature of 55 °C the birefringence is no longer detectable. The non-uniformity in the image is caused by the surface roughness of the polymer film. **C:** The birefringence gradually reappears upon cooling. This image was taken at a temperature of 26 °C and shows identical domains to the pre-melting case. The crossed arrows indicate the orientation of the polarisers. The scale bar is 100 µm.

density is unclear at this point. A possible explanation is the local kinetic trapping of the crystallisable material due to an increased nucleation density compared to the original domain formation.

No further conclusions are drawn from the fact that the areas of birefringence before and after melting and recrystallisation were identical in shape and orientation. This is most likely the consequence of incomplete crystal melting followed by a self-seeding process as described by Xu *et al.*[165]

The observation that the birefringence of the two-dimensional domains is caused by a crystalline polymer has significant implications. Birefringent materials are only visible under crossed polarisation when their refractive index is anisotropic in the image plane, i.e. their *optic axis* has an in-plane component. For a polymer crystallite the optic axis is parallel to the stretched chains and normal to the typical lamellar sheets. Polymer crystallites are thus only visible when they are viewed "edge on", with the polymer chains parallel to the substrate or tilted moderately. The crystallite dimension along the optic axis is, however, limited to nanometre length scales,
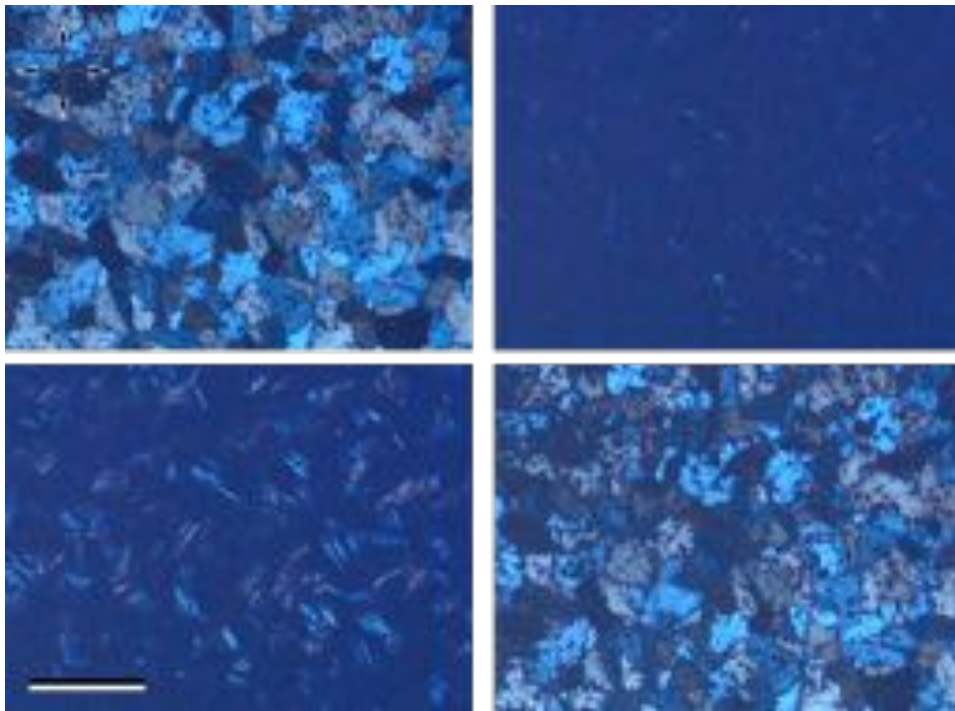
Figure 6.7. Recrystallisation process in birefringent domains. Crossed polarisation micrographs of a semicrystalline sample at different temperatures. Top left: At room temperature, before heating, a pattern of uniform domains is visible. The domains completely disappear during heating to 60 °C (not shown). Top right: Micrograph recorded during cooling at 37 °C. Birefringent regions with large aspect ratios begin to appear. Bottom left: At 36 °C the density of the needle like features is significantly increased. Bottom right: The initial domain pattern reappears at 26 °C. The domains exhibit an increased defect density, which is likely due to incomplete recrystallisation. The crossed arrows indicate the orientation of the polarisers. The scale bar is 200 μm.

which implies that the extended domains of uniform birefringence observed here can only be explained if they consist of large numbers of preferentially aligned crystallites.

To gain more insight on the morphology and arrangement of the individual crystallites, the recrystallisation process was examined more carefully. Figure 6.7 shows optical micrographs recorded at various stages during a crystal melting experiment. The top left and bottom right images show the sample before and after heating to 60 °C. Aside from an increased defect density, the observed domain patterns are identical, indicating that the intermediate states recorded during the cooling step at 37 °C (top right) and 36 °C (bottom left) are representative of the as-annealed sample. These intermediate states show the onset and progression of the recrystallisation

process. The birefringence reappeared in the form of needle-shaped high aspect ratio features that increase in numbers and intensity between the imaged states. The images imply that the domains consist entirely of parallel arrangements of these features. It can further be seen that the correlation between orientation and colour of the needles is equivalent to what is observed in the spherulitic pattern shown in Figure 6.3 : Features oriented along the northwest–southeast axis are light blue in colour, while the perpendicular orientation is grey. No features oriented along the north–south or east–west axes were observed during the recrystallisation stage, and the corresponding directions are dark in the spherulitic patterns. This implies that the needles consist of PEO crystallites with the polymer axes oriented perpendicular to the long needle dimension. The vertical extent of the observed features can not be directly determined via optical microscopy. The crystallite dimensions can, however, be estimated from the peak width in the GIWAXS spectra with the Scherrer equation.[166] A crystallite size of $\approx 9.5\,\text{nm}$ is extracted from the data, which is similar to the expected strut diameter of the PEO gyroid network.

6.2.4 Correlation of Crystal and Microphase Domains

The linear dichroism of single gyroid structured gold facilitates the visualisation of the domains of the microphase separation.[134] To utilise this, the polyisoprene block was replicated in gold as described above, and the resulting films were examined via optical microscopy. Domain patterns were observed for all films fabricated from polymer templates with areas of uniform birefringence. Careful comparison of optical micrographs taken before and after the gold replication procedure revealed that the domain patterns in both cases were congruent. This was consistently the case for all fabricated samples, and an example is shown in Figure 6.8.

To confirm that the domains observed in the gold samples originate from the gold structure, and not from residual crystalline PEO, the heating experiments described above were repeated. The optical appearance of the domains did not change at elevated temperatures (up to 120 °C), confirming the absence of crystalline PEO. Moreover, a gold sample was examined via GIWAXS, and no features associated with crystalline PEO were observed. This confirms that i) no crystalline PEO is present in the film, and ii) the nanoporous gold has not replicated the ordered PEO crystal structure.

Figure 6.8. Domain pattern in polymer film and gold replicate. Optical micrographs of the as annealed polymer film (top) and a free-standing gold replicate (bottom) were recorded under crossed polarisation. Equivalent domain patterns are observed in both cases, which indicates a correlation between the alignment of the crystallites and the microphase separated geometry. The scale bar is 200 μm.

The correlation between the areas of linear dichroism and the domains of microphase separation has been reported before,[134] but it was independently investigated for the present system. Figure 6.9 shows an electron micrograph of a tilted view of a gold gyroid network. Two domains of different orientation are visible, and the inset shows that they are clearly distinguishable at lower magnifications due to their different brightnesses. This can be utilised to image the domain boundaries over large areas without resolving the nanostructure. There is, however, some inherent ambiguity to this method, as the contrast purely relies on the cross-sectional area of the imaged structure. Only significant differences in this cross-sectional area allow the distinction between neighbouring domains. Domains with similar cross sections, for example resulting from slight rotations will appear in the same shading in the micrograph.

104
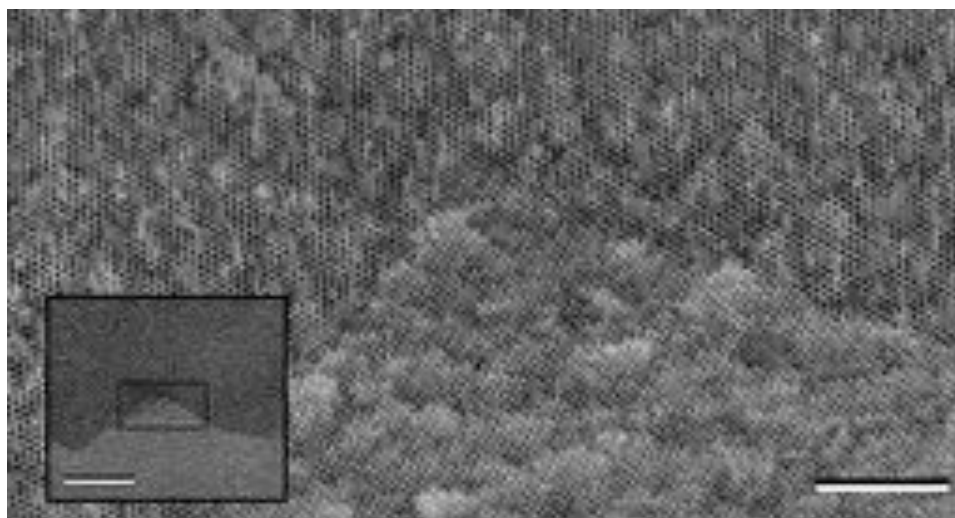
Figure 6.9. Domain detection via electron microscopy. The boundary between two domains of different orientation is imaged under a viewing angle of approximately 45°. The brightness of a pixel corresponds mainly to the cross sectional area of the feature in the respective position. At lower magnifications this causes a visible contrast between the domains, as shown in the inset. The scale bars are 1 μm and 10 μm (inset).

Figure 6.10 shows a comparison between an optical micrograph and and two electron micrographs, taken from the same position. The optical micrograph was recorded under crossed polarisers, and the linear dichroism occurs in several distinct domains. Some of the domain boundaries are also visible in the electron micrographs, and the corresponding contours are congruent. As mentioned above, the contrast mechanism in the electron microscopy is ambiguous, and not all domains can be distinguished. Optical microscopy thus shows further domain segmentation than electron microscopy.

6.3 Conclusion

In summary, the results presented in this chapter prove the existence of semicrystalline poly(ethylene oxide) in microphase separated gyroid networks. The long range order of the structures formed in both processes was visualised via polarised light microscopy, and the complete congruence of the respective domains was observed consistently. This implies a strong correlation between the alignment of the crystallites and the gyroid unit cells, which has not been reported before. The *in-situ* observation of a crystal melting and recrystallisation process revealed that the crystal domains consist of parallel bundles of high aspect ratio crystallites. This observation
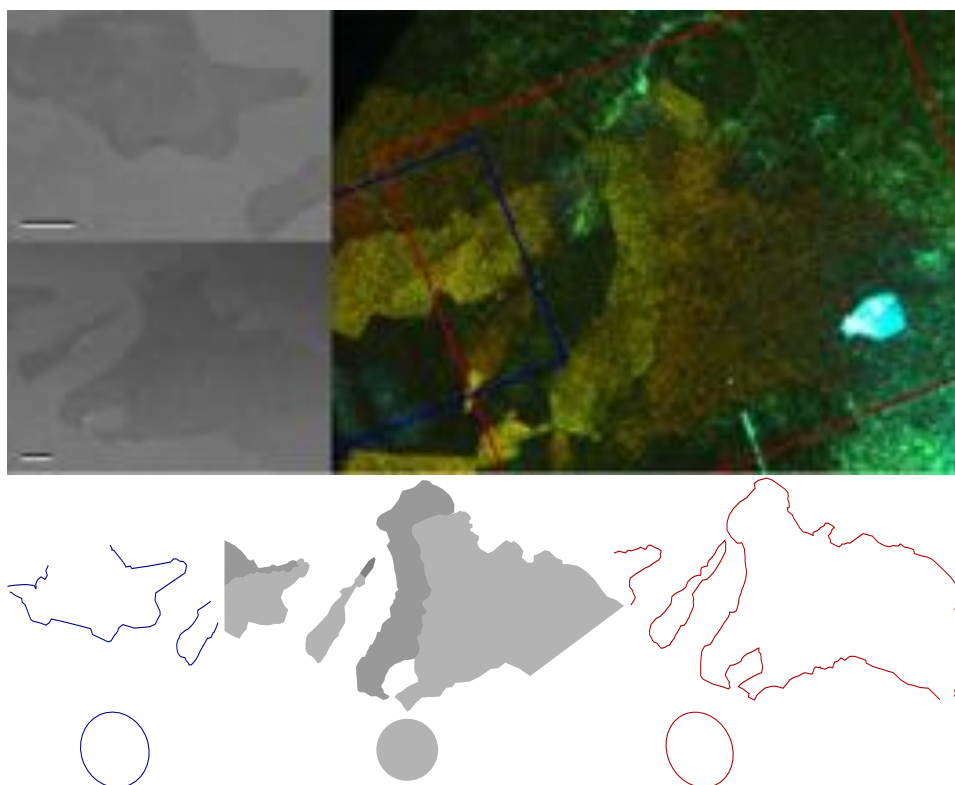
Figure 6.10. Comparison of domain patterns observed optically and via SEM.
The comparison of SEM (top left) and optical (top right) micrographs shows that the domains of linear dichroism correspond to domains of a certain spatial orientation. The ambiguous electron microscopy contrast mechanism is likely to cause the indistinguishability between some of the domains shown here. The images on the bottom show traced versions of the observed domains in the optical (centre) and electron (left and right) micrographs. The traces from the electron micrographs were stretched and rotated to match the optically determined domains. To visualise these distortions 50 µm circles were added to each trace instead of scale bars.

provides further insight into the geometry of the structures, as it suggests a crystallite size several orders of magnitude larger than the unit cells of the surrounding gyroid morphology. The alignment is therefore likely to be caused by the preferential crystal growth along certain network channels, and not by interfacial effects at the channel boundaries.

At this point it can only be speculated about the influence of the solvent on the interplay of the crystallisation and the microphase separation. It is unclear, whether the presence of the solvent causes the two processes to occur simultaneously and under mutual influence, or whether the solvent vapour annealing merely facilitates the formation of long range ordered microphase separation, which in turn causes the aligned crystallisation. It should be kept in mind that a swift solvent removal will cause significant evaporative cooling. The quench rate is therefore likely to have a strong influence on the crystallisation kinetics, as the nucleation density depends on the degree of supercooling. Another hypothesis is that the enhanced long range order and the aligned crystallisation are both independent effects of an intermediate lamellar state: Slow order–order transitions can cause an increased domain size, and the planar interfaces of the lamellar microphases could cause a pre-ordering of the PEO chains, and therefore systematically influence the crystallite orientation.

The upcoming *in-situ* scattering experiments mentioned in Chapter 5 will provide an excellent opportunity to gain further insights.

6.4   Experimental Methods

Sample preparation, solvent vapour annealing and gold replication of the isoprene network were carried out as described in Section 5.4.

Birefringence and linear dichroism were observed with a standard polarised light microscope[2].

A programmable hot-stage[3] was used for the crystal melting experiments in combination with the aforementioned microscope.

GIWAXS data was recorded at the beamline 7.3.3 of the Advanced Light Source, Lawrence Berkeley National Laboratory, California (USA). The incident angle was $0.20°$, and the sample to detector distance was $286\,mm$,

---

[2]BX-60, Olypmus Corporation, Tokyo (Japan)
[3]HFS 91 with TMS 93, Linkam Scientific Instruments, Surrey

as determined via calibration with a silver behenate standard. The photon wavelength was 1.23984 Å, and a silicon hybrid pixel detector was was used to record the scattering patterns[4]. Data analysis was carried out with the *Nika* software[142] in IGOR Pro[5].

---

[4]Pilatus 2M, Dectris AG, Baden-Daettwil (Switzerland)
[5]IGOR Pro 6, WaveMetrics Inc., Oregon (USA)

7

Surface Plasmon Dispersion Measurements

The work presented here is being prepared for publication by Raphael Dehmel, Jeremy J. Baumberg, Ullrich Steiner and Bodo D. Wilts.

In this chapter a novel variant of a Kretschmann-type surface plasmon resonance (SPR) sensor is introduced. The incident light from a confocal microscope is coupled into the sample through a hemispherical glass lens. In contrast to current state-of-the-art techniques which are widely utilised in commercial systems, the proposed method allows the one-shot-acquisition of the full angular reflectance spectrum without any moving parts. The surface plasmon dispersion is mapped by scanning across the entire visible wavelength range with a variable monochromator. A series of measurements on various thin metallic films was conducted, demonstrating the accuracy of the system as well as its sensitivity towards minute changes on the metal surface.

7.1 Introduction

Surface plasmons are charge carrier density oscillations that are confined to the interface between a metal with $\varepsilon_\mathrm{M} < 0$ and a dielectric with $\varepsilon_\mathrm{D} > 0$.[167] When the magnitude of the plasmon wave vector is larger than the wave vector of a photon of the same frequency in the dielectric, the plasmons

can not decay into photons. In this case, the plasmon propagates along the metal surface and the charge carrier oscillations cause evanescent waves in the dielectric.[168] These evanescent waves have a large intensity in the close vicinity of the metal surface, which means that the plasmon oscillations are very sensitive to any change in surface chemistry, such as the adsorption of molecules or the presence of other dielectrics.[169] In practice, these changes are measured via shifts of the excitation resonance, which is visible as a narrow dip in the angular reflectance spectrum. Surface plasmon resonance (SPR) spectroscopy has been a popular technique in chemical and biological sensing applications for many years.[170, 171] The main advantages of SPR sensors are their extremely high sensitivity[172] and the possibility of *in situ*[173] and label-free measurements.[174]

7.1.1 Surface Plasmon Excitation

In order to excite surface plasmons, photons with matching frequency and momentum are required. This means they can not enter the metal film from the dielectric mentioned above, as this would contradict the condition for a non-radiative plasmon. Instead, the photons have to come from an excitation medium with $\varepsilon_E > \varepsilon_D$ where their dispersion and momentum deviate from the vacuum case. Furthermore, the excitation of surface plasmons requires electric field oscillations in the surface plane, which can not be achieved with s-polarised light.[169]

Surface plasmons obey the dispersion relation

$$k_{\mathrm{sp}}(\omega) = \frac{\omega}{c} \left(\frac{1}{\varepsilon_D} + \frac{1}{\varepsilon_M} \right)^{-1/2}.$$

Here ε_D and ε_M are the relative permittivities of the dielectric at the free surface and the metal film respectively and c is the speed of light in vacuum.[170] Since the dielectric constant of the metal is negative in the probed frequency range, changes in ε_D have a large impact on the dispersion relation, which means that even trace amounts of adsorbed material cause measurable shifts in the resonance condition. The excitation photons can only couple to the surface plasmon modes when the projections of their wave vectors onto the surface of the metal film have a matching magnitude. Since this projection
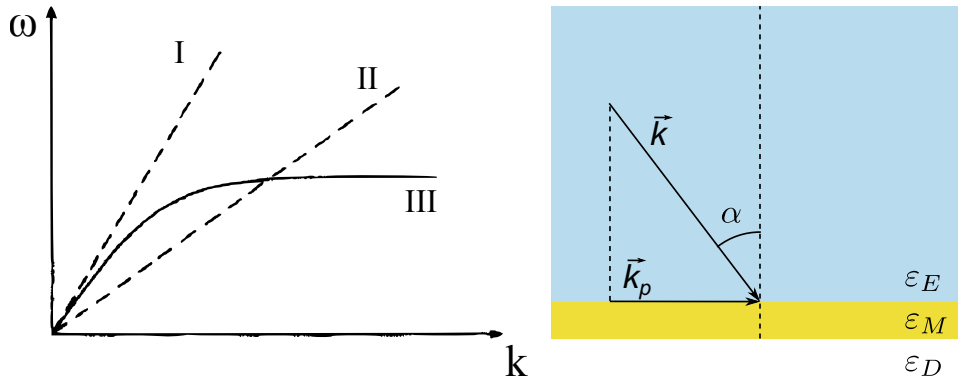
Figure 7.1. Surface plasmon excitation. Left: Dispersion relations for photons in air (I), photons in a dielectric with $\varepsilon \approx 5.5$ (II), and surface plasmons in gold (III). This graph was adapted from Liedberg *et al.*[170] Right: The projection $\vec{k}_\mathrm{p}$ of the wave vector $\vec{k}$ has to match the surface plasmon momentum at the respective energy. Curve II in the graph on the left is valid for $\alpha = 90°$. Decreasing the angle of incidence causes a counter-clockwise rotation of the curve around the origin, shifting the intersect of curves II and III, which marks the case of resonant excitation, to lower frequencies.

depends on the angle of incidence α a pseudo dispersion relation

$$k_\mathrm{p}(\omega) = \frac{\omega}{c}\sqrt{\varepsilon_\mathrm{E}}\sin\alpha$$

can be assigned to the photons (see Figure 7.1). This means that for a given excitation frequency, the resonance condition will be fulfilled for a well-defined angle of incidence which depends on the relation of the dielectric constants,

$$\sin\alpha = \left(\frac{\varepsilon_\mathrm{E}}{\varepsilon_\mathrm{D}} + \frac{\varepsilon_\mathrm{E}}{\varepsilon_\mathrm{M}}\right)^{-1/2}.$$

The non-linearity of the sine function facilitates an increased measurement accuracy, especially at shallow incidence (large α).

7.1.2 Conventional SPR Sensors

The first experimental configuration for an SPR sensor was proposed by A. Otto in 1968.[175] Here, white light is coupled into a glass prism and reaches an opposing surface under a large angle of incidence. The magnitude of wave vector of the photons is increased in the glass, and the high angle of incidence implies that its component parallel to the surface is too large to fulfil the photonic dispersion relation in air. The light undergoes total internal reflection and an evanescent wave propagates along the glass surface. A metal film is positioned parallel to this surface, leaving a narrow air gap

111
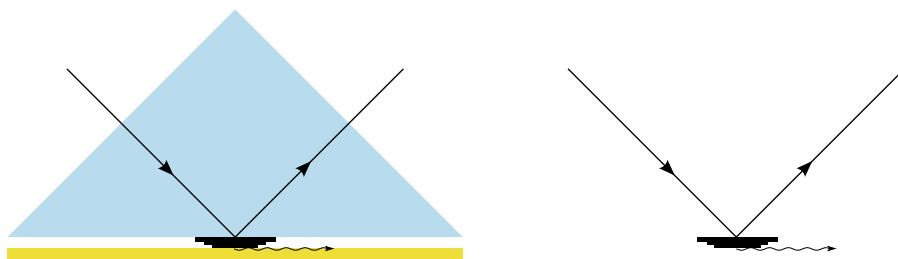
Figure 7.2. Conventional SPR sensors. Left: In the Otto configuration evanescent waves are created via the total internal reflection at a glass–air interface. The evanescent waves couple into a metal film, which is positioned parallel to the glass surface. In the resonant case the excitation of surface plasmons causes a dramatic increase in the tunnelling probability of the photons, which is measurable as a narrow dip in the angular reflectance spectrum. Right: The Kretschmann configuration relies on the sample principles as the Otto configuration, and the only difference between the two is the direct attachment of the metal layer to the glass surface. This makes the sensors significantly more robust and reliable, and the Kretschmann configuration is widely used today.

(see Figure 7.2). For the correct angle, a large fraction of the incident photons tunnel through the potential barrier formed by the air gap, reducing the total internal reflection. When scanning the incident angle, the angular reflectance spectrum exhibits a narrow dip at the plasmon excitation angle.

In a publication from 1971, Erwin Kretschmann argues that an air gap of constant thickness is very hard to realise experimentally on such a small scale and he introduces a more practical experimental configuration.[168] In the so-called Kretschmann configuration, the metal film is deposited directly onto the surface of the prism. Since the non-radiative surface plasmon modes can not exist at the interface with the illumination medium, the evanescent waves have to traverse the metal film before exciting the charge carrier oscillations. The thickness of the metal film should thus be limited to less than 100 nm, to ensure a measurable dip in the angular reflectivity. The Kretschmann configuration is used in most practical applications due to its superior experimental robustness over the Otto configuration.[176] In a typical measurement at least one thin dielectric layer is deposited onto the surface of the metal sensor to functionalise it for a particular analyte of interest.[170, 177] Common sensor metals are gold and silver.[171, 178, 179]

In practice, most sensors use a prism covered by an Au or Ag film and a single wavelength laser is mechanically scanned across an angular range of interest while the reflected intensity is detected. These monochromatic measurements are a significant limitation of the technique as the dispersion
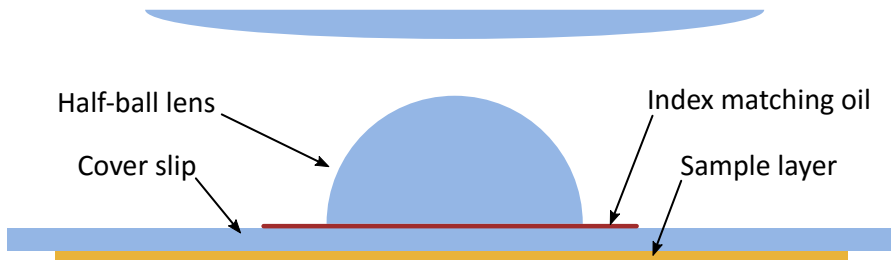
Figure 7.3. Schematic of experimental set-up for SPR measurements. The light-cone emitted by the objective passes through half-ball lens and cover slip and is reflected at the metal layer. Here, surface plasmon resonances are excited by photons with matching polarisation state and angle-of-incidence. The drawing is not to scale.

of the surface plasmon modes can only be characterised by measuring at multiple different wavelengths.[180] Moreover, the mechanical movements required for angular measurements impose a trade-off between angular and temporal resolution on any measurement; real-time experiments often operate in fixed-angle mode and extrapolate the resonance angle from the reflected intensity at a slightly lower angle.[181, 182]

Here we present an adapted Kretschmann approach with a half-ball glass lens replacing the conventional prism (Figure 7.3). The metal film is attached to the flat surface of the half-ball and a confocal microscope is used to illuminate it through the glass, focusing on the metal in the focal point of the sphere. The confocal beam thus enters the glass under normal incidence at all points and no refraction or polarisation occurs at the surface. The same condition holds for the reflected light, which can be detected across the entire numerical aperture of the objective. A light-cone entering the objective from its focal point appears as a circle in the back focal plane. The radius of this circle correlates with the aperture γ of the cone and the focal length f of the objective,

$$r = \tan\left(\frac{\gamma}{2}\right) \cdot f.$$

When recording the back focal plane, i.e. with a Bertrand lens that images the far-field light scattering pattern of the focal point (k-space imaging or conoscopic imaging[183, 184]), the intensity at any given radius r from the optical axis is proportional to the reflectivity at the angle of incidence $\alpha = \arctan\left(r/f\right)$. The back focal plane thus contains the reflectance for all angles of incidence within the numerical aperture of the objective (see Figure 7.4).

A key advantage of this set-up is its wavelength independent geometry. With a tunable light source or an appropriate filtering set-up, a wide spectral range can be rapidly measured and the wavelength-dependent dispersion of the surface plasmons can be easily mapped.

7.2 Results and Discussion

For practical reasons the experimental set-up used in this work deviates from the proposed configuration: The metal layer is not directly deposited onto the planar surface of the half half-ball lens, but onto the underside of a thin glass cover slip. This allows simple sample fabrication pathways, which is more complex with hemispherical substrates, and also facilitates rapid sample changes.

7.2.1 Half-Ball SPR Sensor Assembly

For a measurement, the half-ball lens is placed onto the cover slip, that supports it. A refractive index liquid ($n_\mathrm{r} = 1.52$) is deployed between lens and cover slip to prevent air trapping and interfacial scattering of incident light (see Figure 7.3). The normal incidence condition mentioned above is invalid in this configuration, as the metal layer is no longer in the focal of the glass hemisphere. This could, in principle, be avoided by appropriately manufacturing a spherical lens that accounts for the thickness of the glass slide, but as long as the cover-slip thickness is small compared to the lens radius, the refraction at the spherical surface only causes limited angular deviations which can be taken into account in the data analysis.

The assembly is placed into a conventional light microscope and — using a long-working-distance $50\times$ objective — the incident light is guided through the half-ball lens and focused onto the air-facing metal layer. The insertion of a Bertrand lens moves the back-focal plane of the objective into the image plane and thus images the *k*-space of the reflected light. In a standard microscope with Köhler illumination, the lamp filament is *de facto* imaged confocally with the back focal plane and thus causes strong intensity fluctuations in the k-space images. To circumvent this problem, a diffuse broadband LED light source was used for illumination (see Section 7.4). An example of a surface plasmon resonance in a 40 nm Au layer is shown in

114
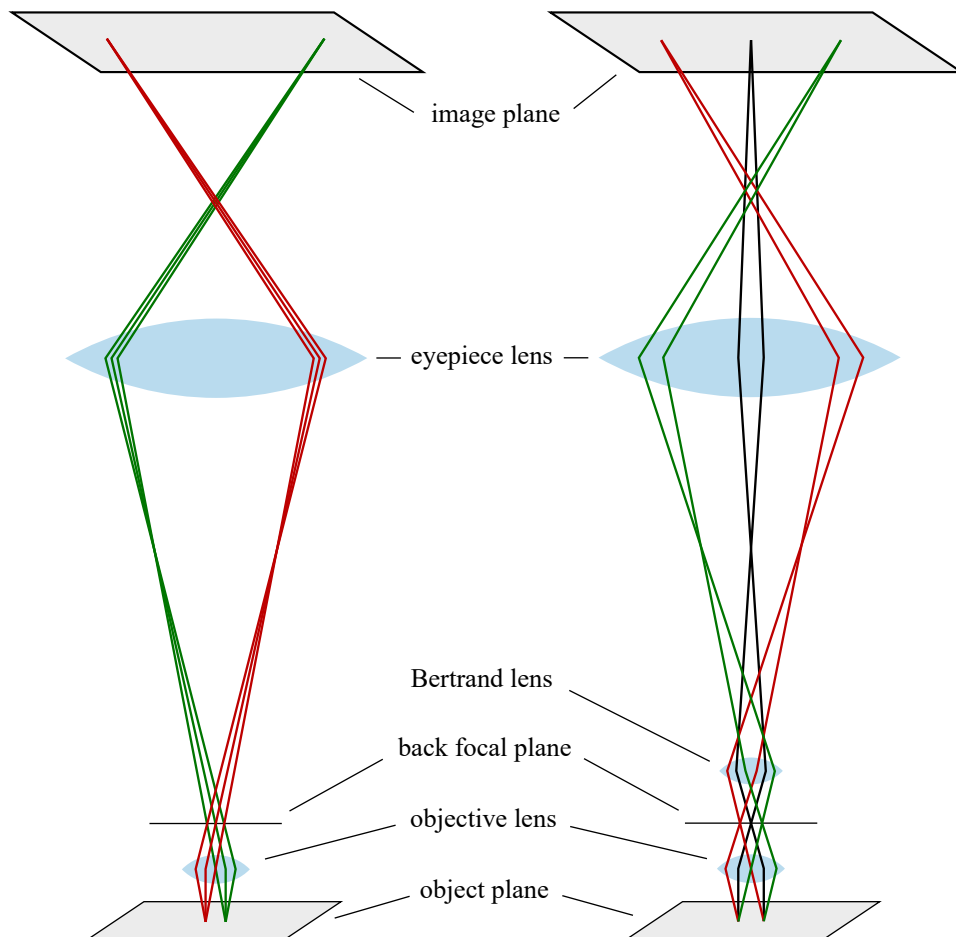
Figure 7.4. Back focal plane imaging. Schematic of the simplified beam path in a conventional microscope with (right) and without (left) a Bertrand lens. In the standard configuration all light emitted from one point in the object plane is focused onto a point in the image plane. When a Betrand lens is used the back focal plane of the objective lens effectively becomes the new object plane. The position of a light ray in the back focal plane depends only on its angle of incidence onto the principal plane of the objective lens. Each point in the image plane thus corresponds to light emitted from the sample under one particular angle.

115
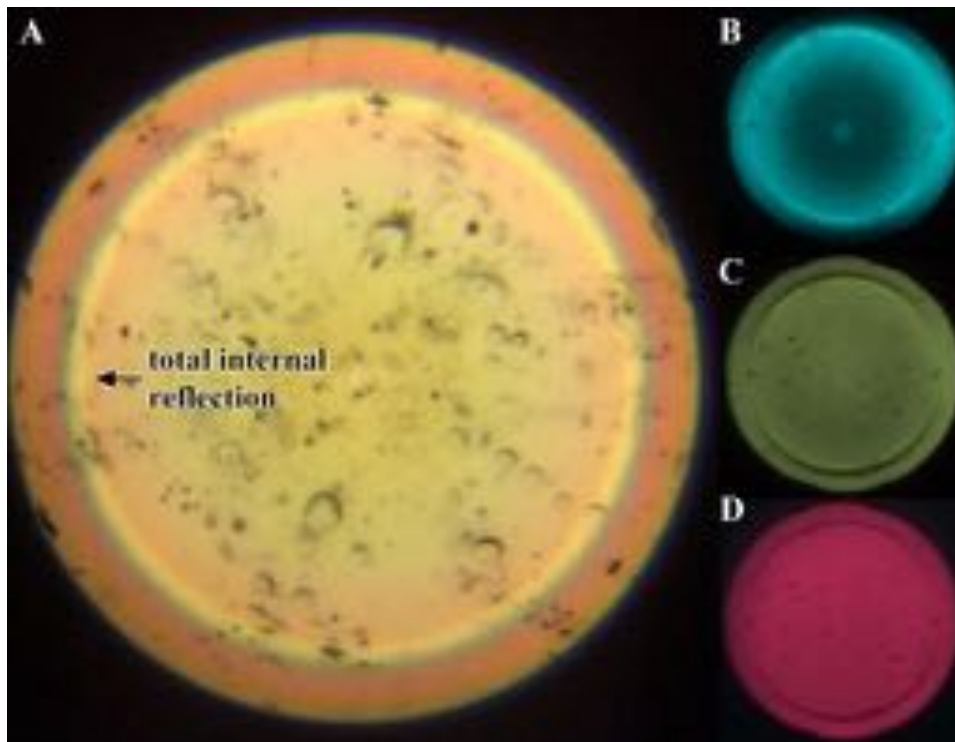
Figure 7.5. Back focal plane images of a 40 nm gold layer illuminated through a glass hemisphere. (A) Reflected RGB image of gold, showing the total internal reflection. (B, C, D) Single wavelength images for 470, 570 and 670 nm with crescent shaped dark areas of frustrated total internal reflection, indicating a resonant surface plasmon excitation. This figure was created by B. D. Wilts.

Figure 7.5. The sample is illuminated with polarised white light and the radius of the recorded circle corresponds to the maximum angle of incidence, which is determined by the numerical aperture of the objective, i.e. $53.13°$ ($NA = 0.8$). One has to keep in mind, however, that the refraction caused by the finite thickness of the cover slip slightly compresses the k-space image, enhancing the cut-off angle to $> 56°$ for an approx. $200\,\mu m$ thick substrate (see Figure 7.7).

Figure 7.5A shows an unfiltered white light image. Close to the total internal reflection angle of the BK7 glass, an isotropic ring of increased reflectance can be seen at $\alpha = 43.13°$. It is surrounded by multiple coloured rings, with a thin blue ring (shorter wavelengths) closer to the centre than a broader ring of red colour (longer wavelengths), indicating the presence of a strong wavelength-dependent resonance. To gain quantitative insight into the wavelength-dependent properties, an adjustable colour filter was inserted into the optical path and monochromatic images (spectral half-width

116

$\approx 7\,\mathrm{nm}$) were taken across the visible spectrum (420–680 nm). Figures 7.5 B–D show reflectance images of a 40 nm gold layer at 470, 570 and 670 nm, respectively. A broad, deep resonance for blue light (Figure 7.5 B) that consecutively narrows for larger wavelengths and shifts towards smaller angles is clearly visible, confirming the white light observations.

7.2.2 Surface Plasmon Dispersion in Metal Films

40 nm thick layers of Au, Ag, and Cu, were imaged in this set-up. For each sample, monochromatic images were taken in 5 nm steps between 420 and 680 nm. A computer algorithm was used for this purpose and the imaging took approximately 10 s per sample. For data analysis a further algorithm was used to first determine the centre of a measured circle and to extract a radial intensity profile for each probed wavelength. These profiles can be averaged across a predefined sector in the image plane to minimise contamination artefacts (see Figure 7.6). The conversion of the radial profiles to angle-dependent reflectance spectra was performed with the help of a previously imaged calibration grating. At this stage, the refraction due to the non-normal incidence on the hemispherical lens has to be taken into account. Figure 7.7 shows how the angle of incidence on the metal film α can be calculated from the angle of incidence on the objective β. The angle θ_1 can be calculated from the lens radius r and the cover slip thickness t via the law of sines,

$$\frac{\sin(\theta_1)}{t} = \frac{\sin(\alpha)}{r}.$$

With Snell's law θ_2 can be calculated from θ_1 and the refractive index n of the lens

$$n \cdot \sin(\theta_1) = \sin(\theta_2).$$

When α, θ_1, and θ_2 are known β can be extracted from the relation

$$\alpha + \theta_1 = \beta + \theta_2.$$

The relation between α and β can thus be written as

$$\beta = \alpha + \arcsin\left(\frac{t}{r} \cdot \sin(\alpha)\right) - \arcsin\left(n \cdot \frac{t}{r} \cdot \sin(\alpha)\right).$$

The conversion facilitates a plot of the reflectivity as a function of the
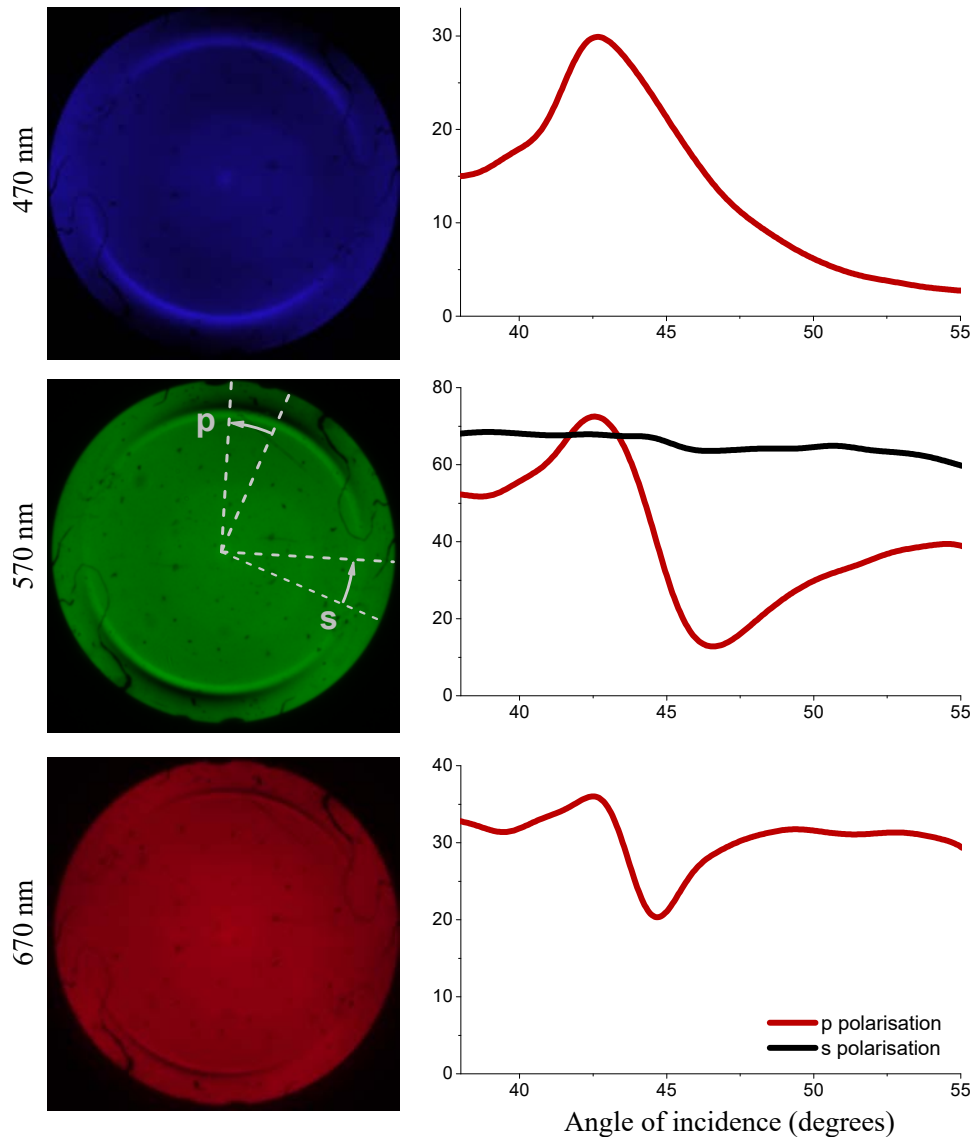
Figure 7.6. Angular intensity profile extraction. Illustration of the extraction of angular reflectance spectra from the acquired *k*-space images. Radial profiles are first extracted from the circular signal, averaging over a predefined sector. With the help of a previously imaged calibration grating the radial values are then converted to angles. The polarisation dependence of the surface plasmon excitation can be seen immediately in the rotational asymmetry of the k-space reflectance. This figure was created by B. D. Wilts and adapted by the author.
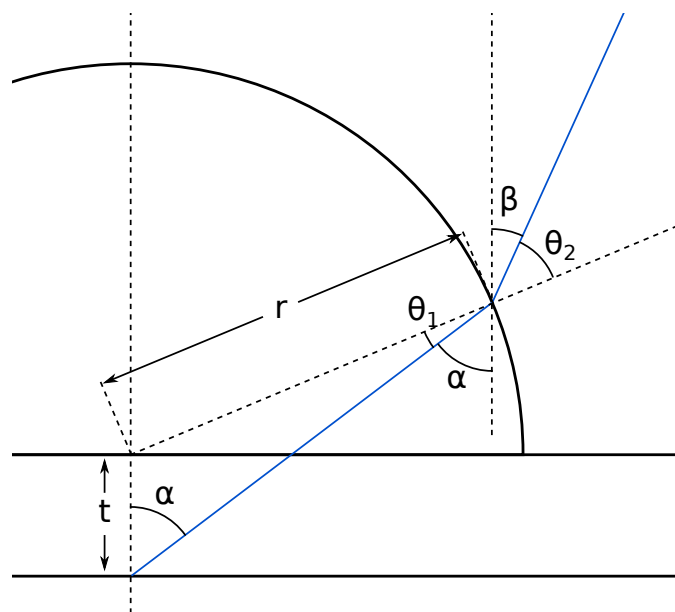
Figure 7.7. Refraction at the half-ball surface. The finite thickness of the cover slip implies that the light can not enter the glass hemisphere under normal incidence when focusing onto the metal surface. The resulting refraction of the light has to be taken into consideration during data analysis. The schematic illustrates that the relation between the angles α and β can be deducted from the angles θ_1 and θ_2, which are related through Snell's law. θ_1 can be determined through the law of the sines from r, t, and α.

angle of incidence and the wavelength of the illumination light. This is equivalent to a dispersion map of the surface plasmons, as the angle of incidence determines the planar momentum of the photons and their energy, which depends on the wavelength. The resonant excitation of surface plasmons causes a frustration of the total internal reflection and is thus visible as a dark feature in the reflectance plot.

Figure 7.8 shows the experimentally determined angular reflectance of 40 nm layers of gold, silver and copper on the left hand side. The corresponding calculated data is shown on the right hand side for comparison . The theoretical angular reflectance was calculated by B. D. Wilts analytically, using a finite-difference time-domain method for each wavelength (see Materials and Methods, ref.[185, 186]). The shapes and positions of the observed features are very similar for all metals, and only the copper data shows slight deviations and noise.

SPR sensors are mainly employed to monitor minute environmental changes, i.e. different analyte binding constants on surfaces or differing layer compositions. To probe the ability of the proposed set-up to detect small amounts of material, a 2 nm thick layer of Ag was evaporated onto a 40 nm thick Au SPR sensor. Figure 7.9 shows the experimental and theoretical angular reflectance at 600 nm for uncoated and coated sensors. The presence of the thin Ag layer is immediately evident, as i) the resonance shifts towards shorter wavelengths, ii) it becomes narrower and iii) it varies in intensity. Again, theoretical and experimental data are in very good agreement with the exception of the resonance intensity. The mismatch here is probably caused by the limited resolution of the acquisition camera combined with the increasing compression in the angular conversion at high angles. Despite these limitations, the presence of the only 2 nm thick layer can be easily detected.

7.3 Conclusion

In conclusion, the technique introduced in this work facilitates rapid characterisation of surface plasmon resonances across wide angular and spectral ranges. It has the potential to significantly outperform state-of-the-art techniques in two key areas: Firstly, monochromatic angular reflectance spectra can be recorded without moving parts in a one-shot measurement, increasing
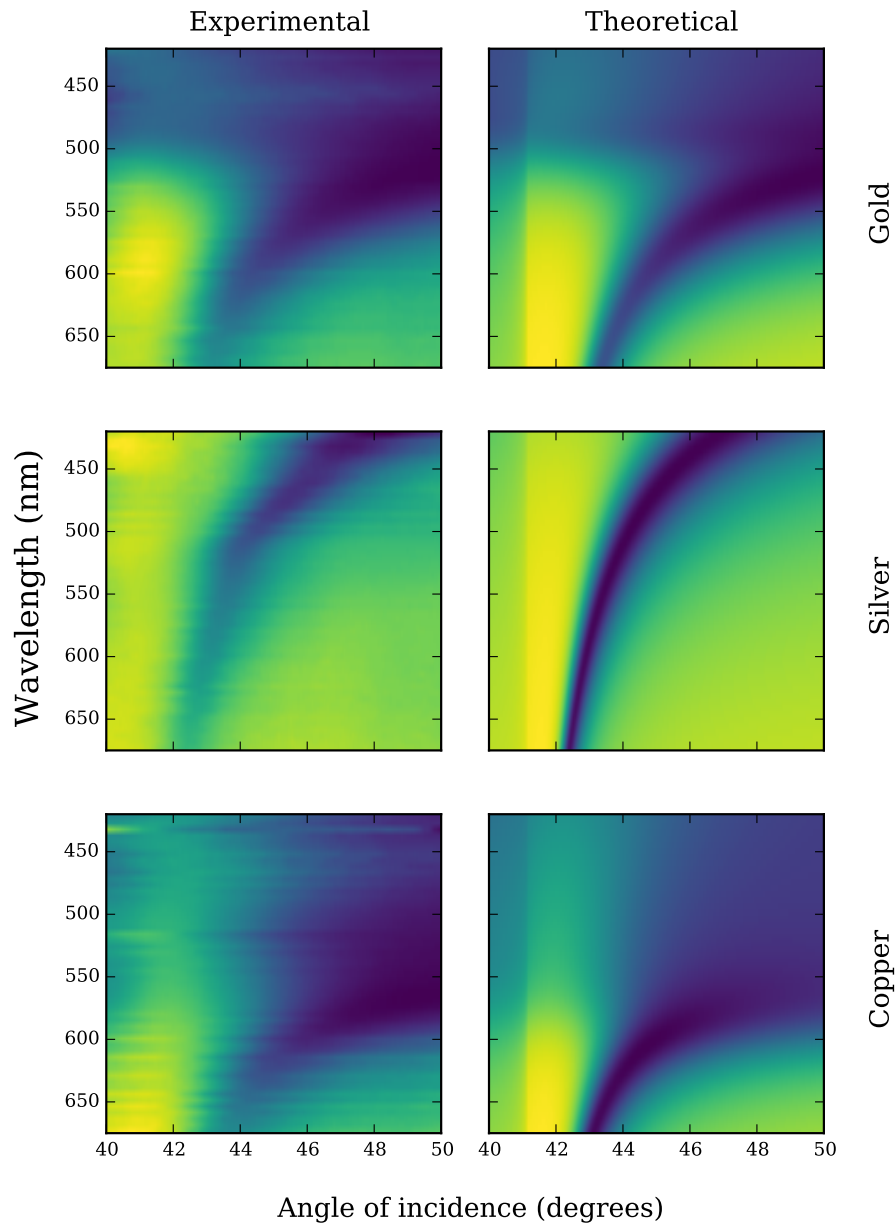
Figure 7.8. Surface Plasmon Resonance in thin metal layers. Experimentally (left) and theoretically (right) determined surface plasmon dispersion in 40nm thick layers of gold (top), silver (middle) and copper (bottom). Intensity units are arbitrary.

121
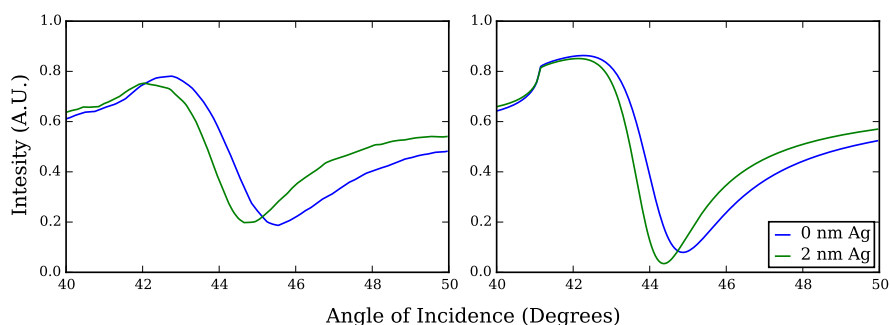
Figure 7.9. Resonance shift caused by a 2 nm thick silver layer on gold. Experimentally (left) and theoretically (right) determined angular reflectance of a 40 nm thick gold layer with (green line) and without (blue line) a 2 nm silver surface layer under 600 nm illumination. The onset of the total internal reflection and the minimum caused by the surface plasmon resonance are clearly visible in the experimental data and the measured resonance shift due to the silver layer is in good agreement with the theoretical data.

the feasible time resolution by orders of magnitude without jeopardising the precision. Secondly, the technique is not limited to monochromatic measurements and a wide range of frequencies can be scanned in an automated fashion. This adds an entirely new dimension to the acquired data, which could, for example, facilitate the discrimination between various analytes with similar dielectric constants but different dispersion behaviour.

The limitations of the presented technique mostly originate from the exclusive use of standard off-the-shelf equipment. While this makes the technique very accessible, its performance could be greatly enhanced by using specialised instruments. The angular resolution for example depends on the pixel density of the detector in the region corresponding to the angular range of interest. A half-ball lens with a higher refractive index would shift this range to lower angles where compression is less significant. A high power light source could improve the signal to noise ratio, or — in combination with a better monochromator — increase the spectral resolution of the technique.

7.4 Materials and Methods

Samples were manufactured by depositing the desired metal onto borosilicate cover slips[1] using an e-beam evaporator[2]. The substrates were first cleaned

---

[1] BK7, Surface Probe Incorporated, Pennsylvania, USA

[2] PVD 75, Kurt J. Lesker Company Limited, East Sussex

in an oxygen plasma[3] for 10 minutes to remove contaminants. Good adhesion of the metal films to the substrates is crucial for the measurements since air pockets caused by de-lamination would falsify the results. For this reason, a 2 nm thick titanium layer was evaporated onto each substrate before the metal layer was deposited.[187]

For k-space imaging, the samples were first placed onto the stage of an optical microscope[4] with the metal layer facing down. The free metal surface has to be air-facing, to avoid a coupling of the evanescent waves into other materials. A home-built microscope slide with a large hole in the centre ensured that the cover slip was only supported at its corners. A thin film of index matching liquid[5] was deployed on top of the cover slip and the hemispherical lens[6] was put into contact, with the planar side facing down. The assembly was illuminated with polarised LED light [7] using a $50 \times$ objective with a numerical aperture of 0.8[8]. Monochromatic back focal plane images were recorded with a Betrand lens[9], a tunable liquid crystal interference filter[10], and a CCD camera[11].

Finite-difference time-domain (FDTD) simulations of the surface plasmon resonances were performed with a commercial grade Maxwell solver[12], using geometries equivalent to the respective experiment (i.e. a 40 nm metal layer and a 2 nm titanium adhesion layer on top of a BK7 glass block).

---

[3]Femto, Diener electronic GmbH + Co. KG, Ebhausen, Germany

[4]BX51, Olympus Corporation, Tokyo, Japan

[5]$n = 1.52$, Series H, Cargille Labs, New Jersey, USA

[6]49-568, Edmund Optics, New Jersey, USA

[7]MCWHL5-C1, Thorlabs Limited, Ely, UK

[8]MPLFLN50x, Olympus Corporation, Tokyo, Japan

[9]U-CPA, Olympus Corporation, Tokyo, Japan

[10]Varispec VIS-7, Perkin Elmer, Massachusets, USA

[11]Infinity 2, Lumenera Corporation, Ontario, Canada

[12]FDTD solutions, Lumerical Corporation, British Columbia, Canada

8

Halogen Bonding and Self-Assembled Monolayers

The work presented here has been submitted for publication by Antonio Abate, Raphael Dehmel, Alessandro Sepe, Ngoc Linh Nguyen, Nicola Marzari, Ullrich Steiner and Chiara Neto.

The work was initiated and coordinated by Antonio Abate and Chiara Neto. The author was responsible for planning and conducting contact angle measurements and AFM scans, and manufactured the majority of the samples for the other characterisation techniques.

This chapter revolves around the fabrication and characterisation of a novel kind of self-assembled monolayer for surface functionalisation. It is based on the formation of halogen bonds between perfluorododecyl iodide molecules and a silicon nitride surface. The substrates were immersed in a dilute solution of the adsorbate for several hours and then washed to remove weakly adsorbed molecules. A variety of characterisation techniques is employed, confirming the formation of a stable and dense monolayer. The author's main contribution was a series of contact angle measurements that point to a surface energy of $2.6\,\mathrm{mJ/m^2}$, which is the lowest value reported for a solid surface.

8.1 Introduction

The interaction between two substances is typically determined by the chemical and mechanical properties of their exposed surfaces. Controlling these surface properties is therefore of great importance for a variety of applications and many industrial processing routes involve some sort of surface treatment. This facilitates the combination of the structural properties of the core material with the surface characteristics of the shell. The benefit of this can be a cost reduction or an increased stability, lifetime and aesthetic appeal of the produced goods. It is, however, also possible to create antibacterial surfaces, or to modify the wettability of a given material. The latter is, for example, used for "self cleaning" products and non-stick pans, but it is also important for a variety of nano-fabrication techniques, such as the ones described in Chapters 4 and 6.

The vast majority of surface treatments involve mechanical modifications of the material or a physical or electrochemical application of a coating layer. In recent years, however, surface modifications by self-assembled monolayers (SAMs) have gained more attention. SAMs are formed when the substrate is brought into contact with certain molecules that are capable of attaching to the surface, while the forces between them are too small to cause large scale aggregation. This approach facilitates complete surface coverage, using only very small amounts of material. Also, energy intensive application procedures are not necessary which makes the technique very interesting for low cost and high volume production.

SAM-forming molecules typically consist of "head groups" and "tail groups". The head chemically reacts with one or more surface molecules of the substrate, creating a strong bond and thus ensuring good adhesion. Attractive forces between neighbouring adsorbate molecules can cause their arrangement into ordered arrays. When the molecules are densely packed, the tail groups will be aligned perpendicular to the substrate. They effectively form a new surface that overrides the properties of the initial substrate material.

For each application, a head group has to be found that is compatible with the substrate and a desired tail group. Thiols, for instance, are carbon–sulphur compounds that bond very well to coin-metal surfaces, such as gold and silver.[188] Other examples are silanes (silicon compounds with four

single bonds), which bond to hydroxyl groups on a variety of inorganic surfaces,[189] and phosphonates (tetrahedral compounds with phosphorus centres), which can bond directly to oxygen atoms.[190]

This chapter introduces a SAM of perfluorododecyl iodide (I-PFC12) on a silicon nitride surface. The novelty of this system is the halogen bond based interaction between adsorbate and substrate.[191]

8.2   Results and Discussion

Samples were fabricated by immersing the substrates into a dilute solution of I-PFC12 in perfluorohexane (FC-72). Theoretical and experimental characterisation was carried out, to investigate the bond strength, morphology and surface energy of the adsorbate layer.

8.2.1   Density Functional Theory Analysis

As chemical bonds are based on electrostatic forces, it can be instructive to evaluate the effective charge distribution in a proposed system. Simulations based on density functional theory (DFT) were performed by N. L. Nguyen and N. Marzari. Their calculations predict a transfer of approximately 0.5 elementary charges from the substrate nitrogen to the iodine in the adsorbate (see Figure 8.1). The bond lengths of carbon–iodine and iodine–nitrogen were calculated as 2.205 and 2.791 Å, respectively. All these results are in good agreement with values previously published for halogen–nitrogen bonds,[192] indicating that this is indeed the dominant interaction in the investigated system.

The self-assembly of large numbers of I-PFC12 molecules on silicon nitride substrates was also modelled with DFT methods. Rendered images of the resulting structures are shown in cross section and from the top in Figure 8.2a and b, respectively. Again, the calculation suggests non-covalent halogen bonding as the energetically most favourable interaction. The corresponding binding energy was calculated as 128 kJ/mol, which is higher than the 84 kJ/mol of the commonly used thiol–gold bond.[194] The theoretical arrangement of the I-PFC12 molecules is highly ordered and extremely dense, as shown in Figure 8.2b, with the flourocarbon tails aligned perpendicular to the substrate (see Figure 8.2).
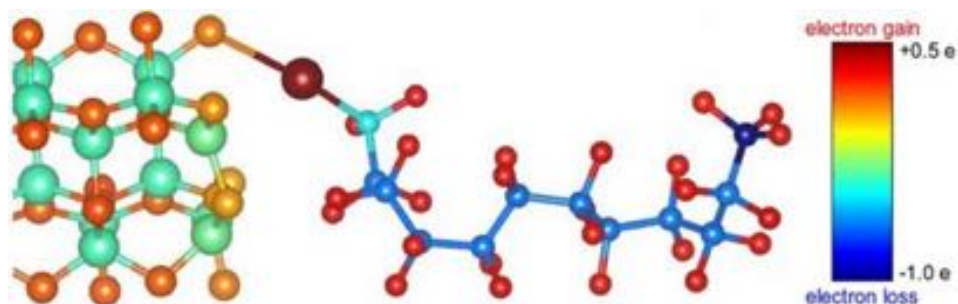
Figure 8.1. Distribution of the Löwdin charges in a I-PFC12 molecule bonded to a silicon nitride surface. The colour of the atoms indicates the deviation of their effective electronic charge from the number of valence electrons, as calculated via DFT methods.[193] The molecule (right) is bonded to the substrate (left) via electrostatic attraction between iodine and nitrogen atoms. Approximately 0.5 e of charge are transferred from the nitrogen to the iodine. This figure was created by N. L. Nguyen and N. Marzari.
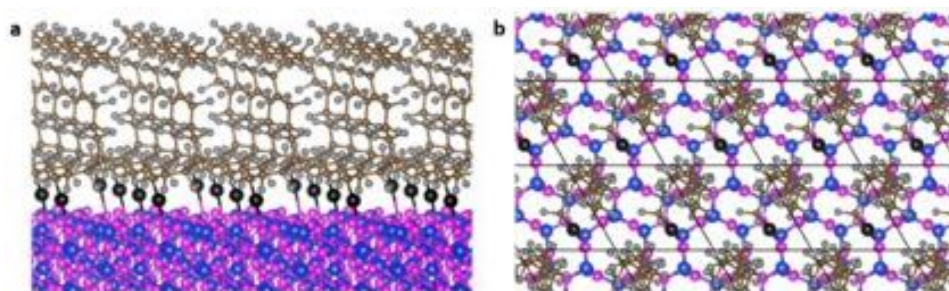
Figure 8.2. Rendered images of the proposed SAM. a) Cross sectional and **b)** birds-eye view of the I-PFC12 molecules on silicon nitride. The different atoms are coloured by element: Iodine: black, carbon: brown, fluorine: white, nitrogen: violet, silicon: blue. This figure was created by N. L. Nguyen and N. Marzari.

It is worth noting that simulations of the same adsorbate on a pure silicon substrate yield covalent iodine–silicon bonds as the dominant interaction. The formed monolayer is inferior to the silicon nitride based SAMs in terms of ordering and coverage density: The average distance between neighbouring adsorbates was calculated as 7.57 Å on silicon nitride and 10.86 Å on silicon.

8.2.2   X-ray Photoelectron Spectroscopy

To examine the nature of the bonds experimentally, x-ray photoelectron spectroscopy (XPS) was performed by Adam Brown and Antonio Abate. XPS relies on the ionisation of analyte atoms by monochromatic high energy photons. The emitted electrons are detected and the distribution of

their kinetic energies is recorded. The kinetic energy of an emitted electron depends on the energy of the incident photon and the binding energy of the electron prior to emission. The binding energy can thus be determined by simply subtracting the kinetic energy of the electron from the photon energy. Electrons that lose kinetic energy in collisions before reaching the detector will have random energies, which means they will only contribute to the background noise in the recorded spectrum and not to one of the detected peaks. This makes the XPS technique inherently surface sensitive, as the probability for collision-free emission is reduced drastically when the distance between the excitation site and the free surface increases. The recorded data thus allows conclusions on the stoichiometric composition of the surface as well as the bonding states of the present atoms. XPS is generally assumed to probe depths of up to 3 nm and has a sensitivity between 0.1 and 1.0 %.[195]

In order to confirm the proposed bonding mechanism, XPS measurements were performed on silicon nitride substrates that were first immersed in a 10 mM solution of I-PFC12 in FC-72 and then rinsed in pure FC-72. Control samples were prepared by immersion in pure FC-72. The spectra presented in Figure 8.3 indicate the presence of oxygen, nitrogen, carbon and silicon on both samples. The O and C signals are likely due to surface contamination, while the Si and N peaks originate from the silicon nitride substrate, as indicated by the Si 2p peak at 101.7 eV.[196] The additional F 1s peak in the spectrum of the I-PFC12 treated sample indicates a surface fluorine content of approximately 20 % and is strong evidence for the formation of an I-PFC12 monolayer. Adsorption of FC-72 molecules to the surface can be ruled out as both samples had similar exposure to the solvent. Also the peak is very sharp and located at 687 eV, which indicates the presence of uniform F–C bonds.[195] The absence of iodine peaks from the spectrum is due to the limited sensitivity of the XPS measurement: The ratio of fluorine to iodine in I-PFC12 is 25:1.

The additional C 1s peaks in the I-PFC12 treated sample can be associated to CF_2 (290 eV) and CF_3 bonds (292 eV) in the perfluorocarbon tail of the molecule[197] (see Figure 8.3B). The N 1s peak is shifted by 0.5 eV between the treated and the untreated sample, which is likely caused by the electron density shift to the adsorbed iodine (see Figure 8.3c). The small, broad peak around 400 eV is due to interactions of nitrogen and sp^2 and

128
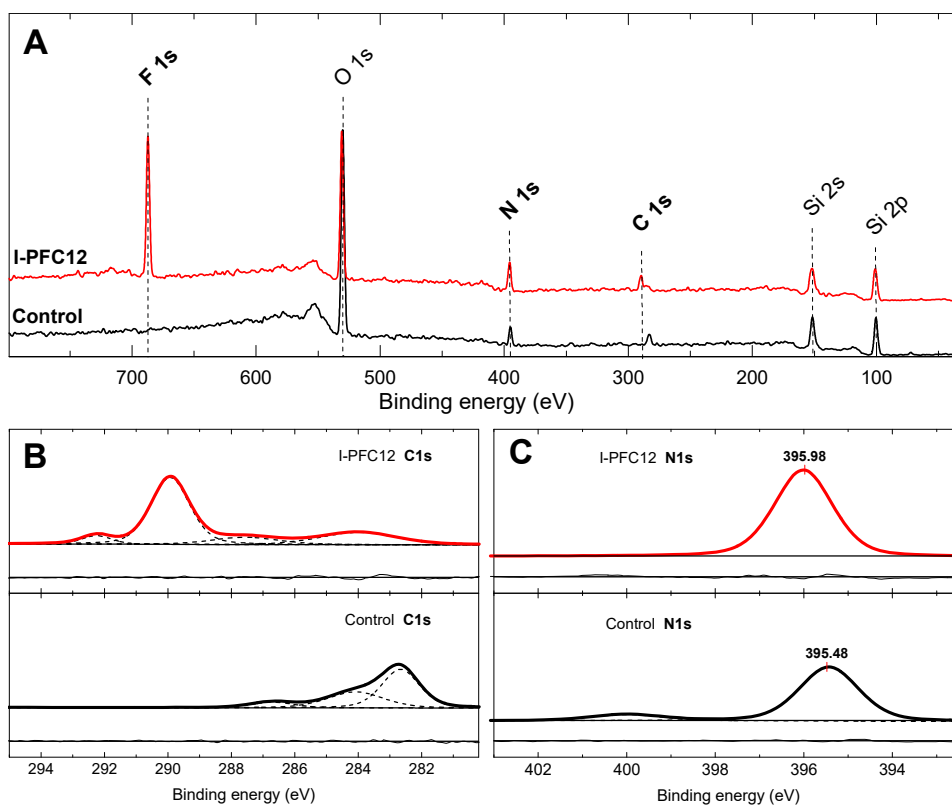
Figure 8.3. XPS spectra of silicon nitride samples with and without I-PFC12 SAMs. A) Both spectra show the same O 1s, Si 2s and Si 2p peaks. The N 1s and C 1s peaks are slightly shifted between the spectra and a strong F 1s peak is only visible in the I-PFC12 sample. **B)** and **C)** show high resolution sections around the C 1s and N 1s peaks, respectively. A Gaussian peak deconvolution was performed to facilitate a quantitative analysis of the spectra. This figure was created by Antonio Abate.
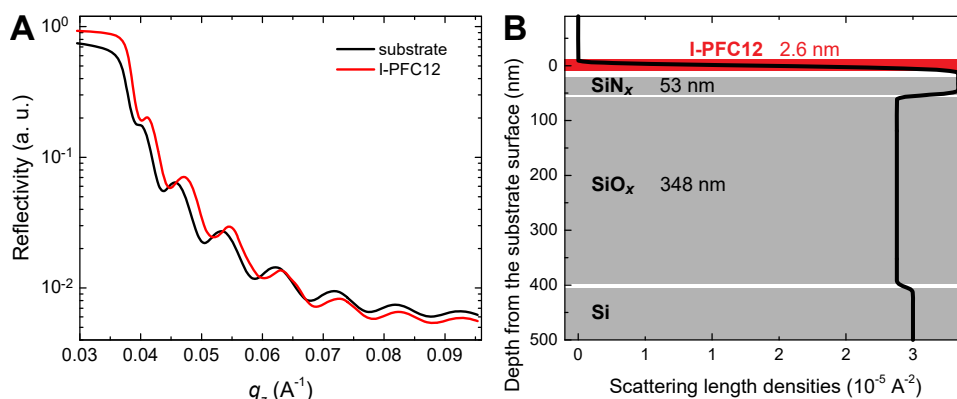
Figure 8.4. X-ray reflectivity data for I-PFC12 SAMs on silicon nitride surfaces.
A) The reflectivity of substrates with and without I-PFC12 monolayers plotted against
the out of plane photon momentum. The solid lines are fits to the measured data
points (hollow spheres/squares). **B)** The thicknesses and scattering length densities
of the layer stack as calculated from the reflectivity data. This figure was created by
Alessandro Sepe.

sp^3-hybridised carbon. The fact that this is not detectable in the I-PFC12
sample indicates that the SAM prevents contaminations or displaces weakly
bonded contaminants.

8.2.3 X-ray Reflectometry Measurements

To determine the thickness of the adsorbed material, x-ray reflectometry
(XRR) measurements were performed by Alessandro Sepe on samples pre-
pared by the author. XRR is based on the specular reflection of collim-
ated x-ray radiation under shallow angles of incidence. The intensity of
the reflected signal depends on the roughness of the reflecting interfaces,
while multilayer structures cause interference fringes in an angular reflect-
ance spectrum. From these fringes it is possible to extract information on
the thickness and scattering length density of the individual layers. This
is, however, a non-trivial step that requires modelling based on reasonable
starting values.

Figure 8.4A shows the angular reflectivity spectra for a silicon nitride
substrate with an I-PFC12 coating as well as a blank control sample. Fitting
and modelling this data yielded a layer stack of 50 nm silicon nitride on
350 nm silicon oxide on a silicon wafer for the untreated sample. These
results are in good agreement with the values stated by the supplier of the
material. For the treated samples an additional layer with a thickness of
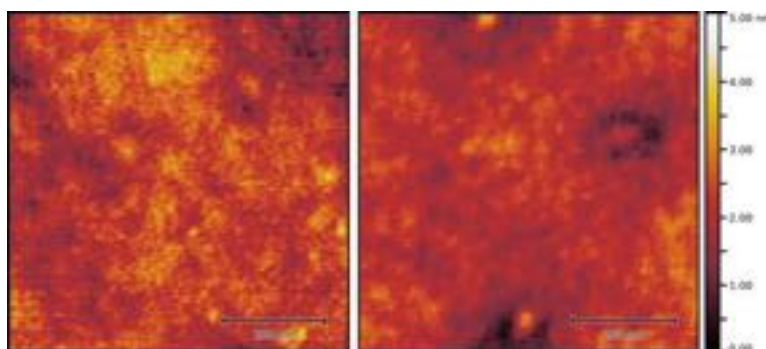
**Figure 8.5. AFM images of blank and I-PFC12 coated silicon nitride surfaces.** Tapping mode AFM measurements were performed on untreated (left) and SAM-coated (right) silicon nitride wafers. The rms surface roughness is 0.5 nm in both cases, indicating a compact and conformal coating of the substrate.

26 ± 4 Å and scattering length density of 1.7×10^{-5}Å^{-2} is found. These values support the hypothesis of a densely packed array of perfluorocarbon chains aligned perpendicular to the substrate.

The stability of the SAMs was evaluated by performing identical XRR measurements on samples that had been immersed into a solvent overnight after the monolayer formation. Three different solvents were evaluated: FC-72, ethanol and toluene. The SAM thicknesses of these samples were 26 ± 4 Å, 9 ± 4 Å and 24 ± 4 Å, respectively. This indicates that the SAMs are very stable in fluorinated (FC-72) and aprotic (toluene) solvents, whereas they slowly degrade in protic solvents (ethanol). As the I-PFC12 molecules are stable in ethanol, the decrease in film thickness is likely due to a reduced surface coverage, and the resulting de-swelling of the perfluorocarbon brush. Also, ethanol or other protic solvents are incapable of dissolving I-PFC12, which means the partial detachment of the SAM is likely due to a displacement of the head groups by another material. Ethanol can be expected to be the displacing adsorbate, as it can form hydrogen bonds with the nitrogen atoms at the substrate surface. The slow speed of this process indicates a good stability of the SAM and the halogen bond, even under unfavourable circumstances. A suppression of halogen bonds in the presence of ethanol has been demonstrated before via force spectroscopy measurements.[198]

The surface of the SAM was also characterised locally via tapping mode AFM. Figure 8.5 shows images of a blank reference sample (left) and a sample with an I-PFC12 SAM (right). Both samples were prepared in identical ways directly before the measurement. The only difference is that

131

the reference sample was immersed in pure FC-72, while the other sample was immersed in a 10 mM solution of I-PFC12 in FC-72. A number of elevated features is visible in the right image, which indicates the formation of agglomerates. This could be due to the same reasons that promote the dense arrangement of the molecules on the surface: Compared to the surface bond, the attractive forces between neighbouring adsorbates are strong enough to give the molecules a certain mobility, facilitating a close packing and potentially also agglomeration. On the other hand it should be noted that surface undulations are also visible on the reference sample. The measurements were not performed under cleanroom conditions, so surface contamination can not be ruled out. The root mean square roughness is about 0.5 nm in both cases, indicating that the SAM exhibits the same surface topography as the substrate, which means it forms a dense conformal coating.

8.2.4 Contact Angle Measurements

The surface energy of the SAM was evaluated using a contact angle goniometer. The surface energy is an important figure of merit, as it indicates the applicability of the SAM for self-cleaning or anti-stick coatings. Perfluorocarbons generally perform well in such applications, as the strong bond between carbon and fluorine drastically decreases their hydrophilicity and lipophilicity.[199] A well known example for this is polytetrafluoroethylene (PTFE, traded under the name Teflon®), which is used as a non-stick coating for cookware and has a surface energy of $20.0 \, \text{mJ/m}^2$.[200] CF_3 groups, as present at the free end of the I-PFC12 molecules, enable even lower surface energies, and values as low as $5.0 \, \text{mJ/m}^2$ have been reported previously for other perfluorocarbons.[201, 202]

To determine the surface energy of the fabricated SAMs a Zisman contact angle analysis was carried out.[203] The underlying assumption of this method is that a surface will only be completely wetted with a contact angle of 0° by substances with equal or lower surface energies. As liquids with arbitrary surface energies aren't readily available, the highest possible surface energy that would completely wet the surface has to be determined via extrapolation. For this purpose, a relation between the surface tension and the contact angle is required. In the case of n-alkanes a linear relationship between the cosine of the contact angle and the surface energy can be assumed.[203] This means that the surface energy of a material can be
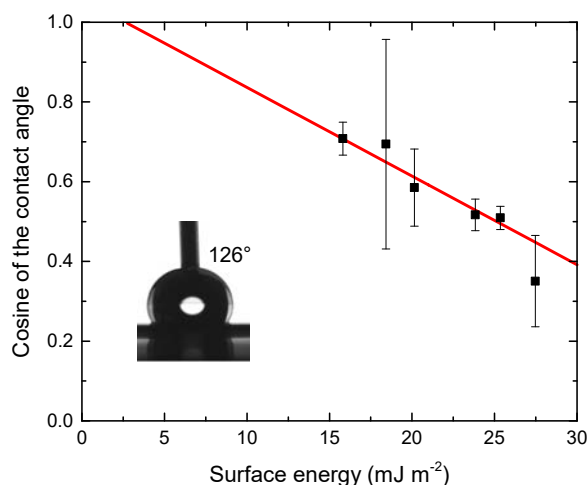
Figure 8.6. Zisman plot of alkane series on I-PFC12 SAMs. The extracted surface energy value is 2.6 mJ/m^2, which is — to the best of our knowledge — the lowest value reported to date. The extremely large water contact angle of 126°, as shown in the inset, confirms the ultra low surface energy. This figure was created by Antonio Abate based on measurements by Chiara Neto (inset) and the author.

determined by first measuring the contact angle of several different alkanes. The cosine of the determined contact angle is then plotted against the surface energy of the respective liquid, and a straight line is fitted to the graph. Finally the intersection of the fitted line and the $y = 1$-line is determined and the corresponding x-value is assumed to be equal to the surface energy of the sample.

Contact angles were measured by slowly dispensing a small droplet of liquid onto a horizontal sample surface. The droplet is then photographed in such a way that the image shows a vertical projection of the assembly. The drop is typically backlit to ensure high contrast contours in the photograph, which in turn facilitate the use of edge detection algorithms to extract the contact angle. To prevent a falsification of the measurement by hysteresis effects, measurements are often performed in the advancing mode, where the volume of the droplet is continuously increased by adding additional solvent through a needle. A series of photos is taken at different volumes, and only when the contact angle no longer changes with increasing volume it is assumed to be correct.

In this work, contact angle measurements were performed on the prepared samples using pentane, hexane, heptane, decane, dodecane and hexadecane. For each solvent seven measurements were performed on different samples. The Zisman plot shown in Figure 8.6 points to a surface energy of

$2.6\,\mathrm{mJ/m^2}$. This is the lowest value reported to date,[202] and is a strong indication of a high I-PFC12 packing density at the surface. The fluctuations of the measurements can to some extent be explained by experimental difficulties with the highly volatile solvents.[203] Also, despite the great care that was taken, surface contaminations could not be completely precluded, as the measurements could not be performed in a cleanroom.

The contact angle of deionised water on a material with a surface energy of $2.6\,\mathrm{mJ/m^2}$ is estimated to be $123°$. The inset of Figure 8.6 shows a contact angle measurement performed by Chiara Neto with de-ionised water on an I-PFC12 SAM. The extracted value of $126°$ is in good agreement with the suggested surface energy, and therefore confirms the results of the Zisman analysis.

8.3 Conclusion

In this chapter, the adsorption behaviour of I-PFC12 molecules on silicon nitride substrates was investigated. The results were evaluated with powerful theoretical and experimental techniques, and all evidence from DFT analysis and XPS measurements points towards non-covalent halogen bonding as the dominant interaction mechanism.

Characterisation via synchrotron based XRR and tapping mode AFM measurements points towards the formation of dense conformal I-PFC12 monolayers on the substrates. This is a significant finding, as halogen bond based self-assembled monolayers have not been reported previously. Furthermore, the SAMs are found to exhibit excellent resistance towards fluorinated and aprotic solvents, while they are only slowly displaced by protic solvents.

Finally, contact angle measurements with a series of alkanes reveal a surface energy of only $2.6\,\mathrm{mJ/m^2}$. This is lower than previously reported values and indicates a high packing density of I-PFC12 on the surface, with the CF_3 groups aligned towards the top.

In summary, the work presented in this chapter shows a simple pathway towards highly dense and well ordered self-assembled monolayers based on halogen bonding. Their high stability and exceptionally low surface energy make them interesting candidates for a variety of technological applications.

8.4 Materials and Methods

Theoretical analysis of the interaction of I-PFC12 and the (001)-surface of silicon nitride was carried out by N. L. Nguyen and N. Marzari. Density functional theory was employed with the generalised gradient approximation of Perdew-Burke-Ernzerhof and van der Waals interaction corrections. Electron–ion interactions were accounted for via ultrasoft pseuopotential calculations with scalar relativistic effects and energy cutoffs of 30 and 300 Ry for the plane wave expansion and the charge density, respectively. For Brillouin-zone integration, the special-point technique was applied with a $6 \times 6 \times 1$ Monkhorst-Pack grid. To model the substrate, a 5 until-cell thick Si_3N_4 slab with periodic boundary conditions in the (100) and (010) directions was generated. In the (001) direction, the bottom layer was fixed to the bulk state and adsorbates were simulated at the top layer. To prevent electrostatic interactions between neighbouring replicas they were separated by 12 Å thick vacuum layers. The PWscf code of the Quantum-ESPRESSO distribution was used for all calculations.

The self-assembled monolayers were prepared on wafers consisting of 50 nm Si_3N_4 on 350 nm SiO_2 on silicon[1]. Substrates were cleaned by sonication in ethanol[2] for 5 minutes and subsequent plasma treatment in air for 1 minute at approximately 0.4 mbar and 30 W[3]. Directly before immersion into the 10 mM solution of perfluorododecyl iodide[4] (I-PFC12) in tetradecafluorohexane[5] (FC-72) or pure FC-72 (control samples) the substrates were cleaned with a CO_2 snow jet[6]. The samples were then immersed over night (14 h), and rinsed with clean FC-72 immediately after removing them from the solution. To remove any weakly bonded species they were then also immersed in clean FC-72 for approximately 6 hours.

X-ray photoelectron spectroscopy was carried out in a commercial instrument[7] with Al Kα radiation for excitation (1486.9 eV, 8.3 Å). The measurements were taken at 120 W power in a 1 mm^2 large spot. The step widths were 1 eV and 0.1 eV for the coarse and high resolution spectra, respectively.

---

[1] Pi-Kem Limited, Staffordshire

[2] Analytical Reagent Grade, Fisher Scientific, Leicestershire

[3] Femto, Diener electronic GmbH + Co. KG, Ebhausen, Germany

[4] 97 %, Sigma Aldrich, Dorset

[5] Fluorinert® FC-72, 3M, Minnesota (USA)

[6] Applied Surface Technologies, New Jersey (USA)

[7] Escalab 220i-XL, VG Scientific, West Sussex

X-ray reflectometry was carried out at a synchrotron[8] at a wavelength of 1.15 Å. An ion chamber with a $50 \times 30\,mm^2$ aperture and a beamstop was used as the detector with an integration time of 1 s per data point. The data was analysed via Parratt formalism based modelling.

Zisman analysis was carried out with the help of a contact angle goniometer[9]. The alkane solvents were purchased from Sigma Aldrich, Dorset at the highest available purity. A 1 ml glass syringe with a special needle and tubing system[10] was used and thoroughly cleaned before each measurement. Due to the high volatility of the low surface energy alkanes the dispensing rate and amount had to be adjusted between the different solvents. For Hexane and Dodecane, 5 µl were dispensed at a rate of 1 µl/s. For decane and heptane (7.5 µl @ 2.5 µl/s), and especially for hexane and pentane (12.5 µl @ 5 µl/s) these values had to be increased to counterbalance the fast solvent evaporation. This fast evaporation also made it impossible to perform meaningful static or receding contact angle measurements, and only advancing contact angles were measured.

---

[8]D1 beamline, Cornell High Energy Synchrotron Source (CHESS), New York (USA)

[9]Cam 200, KSV Instruments Limited, Helsinki (Finland)

[10]90539/00 and 86510 (gauge 22), Hamilton Company, Bonaduz (Switzerland)

9

Summary and Outlook

Nanofabrication techniques are of increasing importance for a wide variety of applications. With conventional top-down methods approaching fundamental limitations in many fields, the bottom-up approach is gaining more and more attention.

9.1 Summary

Polymer self-assembly is a particularly elegant technique, where periodic nanostructures can be formed across macroscopic dimensions with passive building blocks. The integration of this technique into complex fabrication procedures is, however, a key challenge, and practical applications remain rare. In Chapter 4 such an integration was demonstrated, and functional conjugated polymer devices were fabricated. Performance enhancements that have been predicted for many nanostructured materials due to their increased specific surface area were confirmed experimentally, by comparing the electrochromic performance of templated and non-templated devices. The presented fabrication pathway might be interesting for large scale production, as no energy intensive acid etching steps are required to dissolve inorganic templates.

The main part of the presented work is motivated by the optical metamaterial properties of chiral and periodic gold nanostructures. To facilitate the characterisation of the anisotropic optical response of such structures, a solvent vapour annealing protocol was developed to fabricate nanostructured templates with enhanced long range order. The complexity and sensitivity

of the underlying mechanisms is not well represented in previous publications, where mainly slow drying procedures were employed. Especially the requirement for a precise control of the temperature and the drying rate of the polymer samples is often neglected, and little quantitative information is available. The drying process is thus strongly influenced by ambient conditions, which severely limits the reproducibility. The experimental set-up built during the work presented in Chapter 5 allows the automated and precise control of the solvent vapour pressure in the annealing chamber, while the temperatures are regulated to narrow tolerances. After tedious optimisation, a fabrication protocol was found that enabled the reproducible fabrication of samples with enhanced long range order. Fluctuations in the conditions required for the formation of this long range order meant that the recipe had to be adapted regularly, based on phenomenological observations. Gyroid structured gold films with long range order on the millimetre scale were fabricated with this technique, facilitating initial goniometric measurements. Long range ordered polymer templates are, however, also interesting for a variety of other applications, such as self-assembly based surface patterning.

During the optimisation of the annealing protocol large birefringent structures were discovered in the polymer films as discussed in Chapter 6. Further investigation revealed that these features were congruent with the domains of microphase separation, and therefore provided a method for the instantaneous evaluation of the obtained long range order. This observation allowed a much more rapid and efficient optimisation of the annealing protocol, but also provided an avenue for further research: The birefringent domains were found to be caused by preferentially aligned crystallisation of one of the PEO polymer block. Preferential crystal alignment within gyroid networks has not been reported so far, and the competition between the driving forces of the crystallisation and the microphase separation might be a crucial factor in the formation of long range order.

The project discussed in Chapter 7 was based on a more application-oriented approach to the optical characterisation of plasmonic nanostructures. A novel type of surface plasmon resonance sensor was introduced and tested successfully. The use of a small hemispherical glass lens allows a confocal operation of the sensor in a conventional light microscope, and thus an instantaneous characterisation of the total internal reflection across

the entire numerical aperture of the objective. This is a significant advantage over previous sensors, where equivalent measurements are conducted by mechanically moving the light source and detector across the angular range of interest. The geometry of the proposed sensor is also independent of the illumination wavelength, which means that the measurements can be repeated rapidly across wide spectral ranges. This adds a new dimension to the measurement, and facilitates the characterisation of the surface plasmon dispersion, which is a useful aspect for many applications.

In Chapter 8, work on a novel kind of self-assembled monolayer is presented. A remarkable aspect of this project is that the adhesion of the functional molecules to the silicon nitride substrates is based on non-covalent halogen bonding. Samples were fabricated by simply immersing them in dilute solutions of the molecule, and subsequent contact angle measurements revealed a lower surface energy value than previously reported for any substance. Superhydrophobic surfaces are an interesting application on their own, and surface functionalisation techniques are crucial parts of many nanofabrication techniques.

9.2   Outlook

Several of the projects described in this work offer significant scope for further investigation. The fluctuations in the solvent annealing experiments, for example, are not well understood. To learn more about the underlying mechanisms an adapted version of the experimental set-up has been developed to allow small angle X-ray scattering measurements during the annealing procedures. This allows the *in-situ* tracking of the microphase separated morphology and should reveal the cause for the formation of long range order. Other interesting aspects are the influence of electric fields and the chain length and composition of the polymer.

The *in-situ* scattering experiments could also provide valuable insights on the interplay of microphase separation and crystallisation. In particular, the crystallisation is likely to depend crucially on the drying rate of the film and the associated evaporative cooling. Another interesting question is whether or not the volume change associated with the crystallisation causes a measurable deformation of the microphase separated structure.

The presented goniometer measurements are merely the starting point

of a detailed optical characterisation of the fabricated gold gyroids. The understanding of the complex optical response of nanostructured plasmonic materials can only be enhanced if the measurements are combined with theoretical modelling, which in turn depends critically on the experimental data. Additional experimental techniques are also under development: A high precision interferometry set-up is currently being built, to allow the direct measurement of the phase of the reflected and transmitted light. This is necessary to calculate the refractive index of the samples, which would otherwise rely on the exact determination of the effective material parameters. Of particular interest is the sign of the refractive index, as negative index materials remain an important objective in the metamaterial community.

Bibliography

[1] R. P. Feynman. There's Plenty of Room at the Bottom. *Engineering and Science*, 23(5):22–36, February 1960.

[2] Samsung Breaks Ground on $14 Billion Fab. `http://www.eetimes.com/document.asp?doc_id=1326565`.

[3] P. W. K. Rothemund. Folding DNA to create nanoscale shapes and patterns. *Nature*, 440(7082):297–302, March 2006. doi:10.1038/nature04586.

[4] Q. Jiang, C. Song, J. Nangreave, X. Liu, L. Lin, D. Qiu, Z.-G. Wang, G. Zou, X. Liang, H. Yan, and B. Ding. DNA Origami as a Carrier for Circumvention of Drug Resistance. *Journal of the American Chemical Society*, 134(32):13396–13403, August 2012. doi:10.1021/ja304263n.

[5] R. M. Zadegan, M. D. E. Jepsen, K. E. Thomsen, A. H. Okholm, D. H. Schaffert, E. S. Andersen, V. Birkedal, and J. Kjems. Construction of a 4 Zeptoliters Switchable 3D DNA Box Origami. *ACS Nano*, 6(11):10050–10053, November 2012. doi:10.1021/nn303767b.

[6] Y. Amir, E. Ben-Ishay, D. Levner, S. Ittah, A. Abu-Horowitz, and I. Bachelet. Universal computing by DNA origami robots in a living animal. *Nature Nanotechnology*, 9(5):353–357, May 2014. doi:10.1038/nnano.2014.58.

[7] E. Gorter and F. Grendel. ON BIMOLECULAR LAYERS OF LIPOIDS ON THE CHROMOCYTES OF THE BLOOD. *The Journal of Experimental Medicine*, 41(4):439–443, March 1925.

[8] G. van Meer, D. R. Voelker, and G. W. Feigenson. Membrane lipids: where they are and how they behave. *Nature Reviews Molecular Cell Biology*, 9(2):112–124, February 2008. doi:10.1038/nrm2330.

[9] E. Sackmann. Supported Membranes: Scientific and Practical Applications. *Science*, 271(5245):43–48, May 1996. doi:10.1126/science.271.5245.43.

[10] A. Avdeef, P. E. Nielsen, and O. Tsinman. PAMPA—a drug absorption in vitro model: 11. Matching the in vivo unstirred water layer thickness by

individual-well stirring in microtitre plates. *European Journal of Pharmaceutical Sciences*, 22(5):365–374, August 2004. doi:10.1016/j.ejps.2004.04.009.

[11] F. S. Bates and G. H. Fredrickson. Block Copolymers—Designer Soft Materials. *Physics Today*, 52(2):32–38, February 1999. doi:10.1063/1.882522.

[12] J. M. Honig. *Thermodynamics: Principles Characterizing Physical and Chemical Processes*. Academic Press, December 2013. ISBN 978-0-12-420110-1.

[13] M. L. Huggins. Solutions of Long Chain Compounds. *The Journal of Chemical Physics*, 9(5):440–440, May 1941. doi:10.1063/1.1750930.

[14] P. J. Flory. Thermodynamics of High Polymer Solutions. *The Journal of Chemical Physics*, 10(1):51–61, January 1942. doi:10.1063/1.1723621.

[15] P. J. Flory. *Principles of Polymer Chemistry*. Cornell University Press, 1953. ISBN 978-0-8014-0134-3.

[16] P.-G. de Gennes. *Scaling Concepts in Polymer Physics*. Cornell University Press, 1979. ISBN 978-0-8014-1203-5.

[17] K. H. Meyer, E. Wolff, and C. G. Boissonnas. Propriétés des polymères en solution. XII. Energie libre et chaleur de dilution. Système caoutchouc-toluène. *Helvetica Chimica Acta*, 23(1):430–439, January 1940. doi:10.1002/hlca.19400230154.

[18] P. Stamberger. A study of the vapour-pressure diminution of rubber jelies. *Journal of the Chemical Society (Resumed)*, 1929. Part II.(0):2318–2326, January 1929. doi:10.1039/JR9290002318.

[19] F. Scheffold, E. Eiser, A. Budkowski, U. Steiner, J. Klein, and L. J. Fetters. Surface phase behavior in binary polymer mixtures. I. Miscibility, phase coexistence, and interactions in polyolefin blends. *The Journal of Chemical Physics*, 104(21):8786–8794, June 1996. doi:10.1063/1.471568.

[20] M. Rubinstein and R. H. Colby. *Polymer Physics*. OUP Oxford, June 2003. ISBN 978-0-19-852059-7.

[21] L. Leibler. Theory of Microphase Separation in Block Copolymers. *Macromolecules*, 13(6):1602–1617, November 1980. doi:10.1021/ma60078a047.

[22] P.-G. de Gennes. Theory of X-ray scattering by liquid macromolecules with heavy atom labels. *Journal de Physique*, 31(2-3):4, 1970. doi:10.1051/jphys:01970003102-3023500.

[23] M. W. Matsen and M. Schick. Stable and unstable phases of a diblock copolymer melt. *Physical Review Letters*, 72(16):2660–2663, April 1994. doi:10.1103/PhysRevLett.72.2660.

[24] U. Breiner, U. Krappe, T. Jakob, V. Abetz, and R. Stadler. Spheres on spheres – a novel spherical multiphase morphology in polystyrene-block-polybutadiene-block-poly(methyl methacrylate) triblock copolymers. *Polymer Bulletin*, 40(2-3):219–226, February 1998. doi:10.1007/s002890050245.

[25] U. Breiner, U. Krappe, V. Abetz, and R. Stadler. Cylindrical morphologies in asymmetric ABC triblock copolymers. *Macromolecular Chemistry and Physics*, 198(4):1051–1083, April 1997. doi:10.1002/macp.1997.021980411.

[26] T. A. Shefelbine, M. E. Vigild, M. W. Matsen, D. A. Hajduk, M. A. Hillmyer, E. L. Cussler, and F. S. Bates. Core-Shell Gyroid Morphology in a Poly(isoprene-block-styrene-block-dimethylsiloxane) Triblock Copolymer. *Journal of the American Chemical Society*, 121(37):8457–8465, September 1999. doi:10.1021/ja991442h.

[27] T. H. Epps, E. W. Cochran, T. S. Bailey, R. S. Waletzko, C. M. Hardy, and F. S. Bates. Ordered Network Phases in Linear Poly(isoprene-b-styrene-b-ethylene oxide) Triblock Copolymers. *Macromolecules*, 37(22):8325–8341, November 2004. doi:10.1021/ma048762s.

[28] A. H. Schoen. Alan Schoen geometry. http://schoengeometry.com/e-tpms.html.

[29] U. Dierkes, S. Hildebrandt, and F. Sauvigny. Representation Formulas and Examples of Minimal Surfaces. In *Minimal Surfaces*, number 339 in Grundlehren der mathematischen Wissenschaften, pages 91–236. Springer Berlin Heidelberg, 2010. ISBN 978-3-642-11697-1 978-3-642-11698-8. doi:10.1007/978-3-642-11698-8_3.

[30] J. Hoffman and D. Hoffman. The Scientific Graphics Project. https://secure.msri.org/about/sgp/jim/geom/level/minimal/index.html.

[31] D. A. Hajduk, P. E. Harper, S. M. Gruner, C. C. Honeker, G. Kim, E. L. Thomas, and L. J. Fetters. The Gyroid: A New Equilibrium Morphology in Weakly Segregated Diblock Copolymers. *Macromolecules*, 27(15):4063–4075, July 1994. doi:10.1021/ma00093a006.

[32] M. R. J. Scherer. *Double-Gyroid-Structured Functional Materials*. Springer Theses. Springer International Publishing, Heidelberg, 2013. ISBN 978-3-319-00353-5 978-3-319-00354-2.

[33] Y. Tselikas, N. Hadjichristidis, R. L. Lescanec, C. C. Honeker, M. Wohlgemuth, and E. L. Thomas. Architecturally-Induced Tricontinuous Cubic Morphology in Compositionally Symmetric Miktoarm Starblock Copolymers. *Macromolecules*, 29(10):3390–3396, January 1996. doi:10.1021/ma9515083.

[34] Y. Xia, M. Yoshio, and H. Noguchi. Improved electrochemical performance of LiFePO4 by increasing its specific surface area. *Electrochimica Acta*, 52(1):240–245, October 2006. doi:10.1016/j.electacta.2006.05.002.

[35] F. Lu, W. Cai, and Y. Zhang. ZnO Hierarchical Micro/Nanoarchitectures: Solvothermal Synthesis and Structurally Enhanced Photocatalytic Performance. *Advanced Functional Materials*, 18(7):1047–1056, April 2008. doi:10.1002/adfm.200700973.

[36] D. Chen, F. Huang, Y.-B. Cheng, and R. A. Caruso. Mesoporous Anatase TiO2 Beads with High Surface Areas and Controllable Pore Sizes: A Superior Candidate for High-Performance Dye-Sensitized Solar Cells. *Advanced Materials*, 21(21):2206–2210, June 2009. doi:10.1002/adma.200802603.

[37] B. Lim, M. Jiang, P. H. C. Camargo, E. C. Cho, J. Tao, X. Lu, Y. Zhu, and Y. Xia. Pd-Pt Bimetallic Nanodendrites with High Activity for Oxygen Reduction. *Science*, 324(5932):1302–1305, May 2009. doi:10.1126/science.1170377.

[38] R. Rossmanith, C. K. Weiss, J. Geserick, N. Hüsing, U. Hörmann, U. Kaiser, and K. Landfester. Porous Anatase Nanoparticles with High Specific Surface Area Prepared by Miniemulsion Technique. *Chemistry of Materials*, 20(18):5768–5780, September 2008. doi:10.1021/cm800533a.

[39] G. B. DeMaggio, W. E. Frieze, D. W. Gidley, M. Zhu, H. A. Hristov, and A. F. Yee. Interface and Surface Effects on the Glass Transition in Thin Polystyrene Films. *Physical Review Letters*, 78(8):1524–1527, February 1997. doi:10.1103/PhysRevLett.78.1524.

[40] D. R. Burfield and K. L. Lim. Differential scanning calorimetry analysis of natural rubber and related polyisoprenes. Measurement of the glass transition temperature. *Macromolecules*, 16(7):1170–1175, July 1983. doi:10.1021/ma00241a024.

[41] M. M. Feldstein, G. A. Shandryuk, and N. A. Platé. Relation of glass transition temperature to the hydrogen-bonding degree and energy in poly(N-vinyl pyrrolidone) blends with hydroxyl-containing plasticizers. Part 1. Effects of hydroxyl group number in plasticizer molecule. *Polymer*, 42(3):971–979, February 2001. doi:10.1016/S0032-3861(00)00445-6.

[42] A. T. DiBenedetto. Prediction of the glass transition temperature of polymers: A model based on the principle of corresponding states. *Journal of Polymer Science Part B: Polymer Physics*, 25(9):1949–1969, September 1987. doi:10.1002/polb.1987.090250914.

[43] T. S. Chow. Molecular Interpretation of the Glass Transition Temperature of Polymer-Diluent Systems. *Macromolecules*, 13(2):362–364, March 1980. doi:10.1021/ma60074a029.

[44] J. C. Dyre. The glass transition and elastic models of glass-forming liquids. *Reviews of Modern Physics*, 78(3):953–972, September 2006. doi:10.1103/RevModPhys.78.953.

[45] C. T. Moynihan, A. J. Easteal, J. Wilder, and J. Tucker. Dependence of the glass transition temperature on heating and cooling rate. *The Journal of Physical Chemistry*, 78(26):2673–2677, December 1974. doi:10.1021/j100619a008.

[46] A. F. Lewis. The frequency dependence of the glass transition. *Journal of Polymer Science Part B: Polymer Letters*, 1(12):649–654, December 1963. doi:10.1002/pol.1963.110011201.

[47] G. P. Johari and M. Goldstein. Viscous Liquids and the Glass Transition. II. Secondary Relaxations in Glasses of Rigid Molecules. *The Journal of Chemical Physics*, 53(6):2372–2388, September 1970. doi:10.1063/1.1674335.

[48] M. H. Cohen and G. S. Grest. Liquid-glass transition, a free-volume approach. *Physical Review B*, 20(3):1077–1098, August 1979. doi:10.1103/PhysRevB.20.1077.

[49] Y. Maeda and D. R. Paul. Effect of antiplasticization on gas sorption and transport. III. Free volume interpretation. *Journal of Polymer Science Part B: Polymer Physics*, 25(5):1005–1016, May 1987. doi:10.1002/polb.1987.090250503.

[50] J. Zhao, S. L. Simon, and G. B. McKenna. Using 20-million-year-old amber to test the super-Arrhenius behaviour of glass-forming systems. *Nature Communications*, 4:1783, April 2013. doi:10.1038/ncomms2809.

[51] U. Gaur and B. Wunderlich. Study of Microphase Separation in Block Copolymers of Styrene and α-Methylstyrene in the Glass Transition Region Using Quantitative Thermal Analysis. *Macromolecules*, 13(6):1618–1625, November 1980. doi:10.1021/ma60078a048.

[52] R. J. Albalak, E. L. Thomas, and M. S. Capel. Thermal annealing of roll-cast triblock copolymer films. *Polymer*, 38(15):3819–3825, July 1997. doi:10.1016/S0032-3861(96)00938-X.

145

[53] L. M. Leung and J. T. Koberstein. DSC annealing study of microphase separation and multiple endothermic behavior in polyether-based polyurethane block copolymers. *Macromolecules*, 19(3):706–713, March 1986. doi:10.1021/ma00157a038.

[54] J. T. Koberstein and T. P. Russell. Simultaneous SAXS-DSC study of multiple endothermic behavior in polyether-based polyurethane block copolymers. *Macromolecules*, 19(3):714–720, March 1986. doi:10.1021/ma00157a039.

[55] C. D. Doyle. Estimating Thermal Stability of Experimental Polymers by Empirical Thermogravimetric Analysis. *Analytical Chemistry*, 33(1):77–79, January 1961. doi:10.1021/ac60169a022.

[56] D. Cam and M. Marucci. Influence of residual monomers and metals on poly (l-lactide) thermal stability. *Polymer*, 38(8):1879–1884, April 1997. doi:10.1016/S0032-3861(96)00711-2.

[57] T. Xu, H.-C. Kim, J. DeRouchey, C. Seney, C. Levesque, P. Martin, C. M. Stafford, and T. P. Russell. The influence of molecular weight on nanoporous polymer films. *Polymer*, 42(21):9091–9095, October 2001. doi:10.1016/S0032-3861(01)00376-7.

[58] B. C. Berry, A. W. Bosse, J. F. Douglas, R. L. Jones, and A. Karim. Orientational Order in Block Copolymer Films Zone Annealed below the Order-Disorder Transition Temperature. *Nano Letters*, 7(9):2789–2794, September 2007. doi:10.1021/nl071354s.

[59] M. Rubinstein and A. N. Semenov. Dynamics of Entangled Solutions of Associating Polymers. *Macromolecules*, 34(4):1058–1068, February 2001. doi:10.1021/ma0013049.

[60] F. S. Bates and G. H. Fredrickson. Block Copolymer Thermodynamics: Theory and Experiment. *Annual Review of Physical Chemistry*, 41(1):525–557, 1990. doi:10.1146/annurev.pc.41.100190.002521.

[61] P. Alexandridis, U. Olsson, and B. Lindman. A Record Nine Different Phases (Four Cubic, Two Hexagonal, and One Lamellar Lyotropic Liquid Crystalline and Two Micellar Solutions) in a Ternary Isothermal System of an Amphiphilic Block Copolymer and Selective Solvents (Water and Oil). *Langmuir*, 14(10):2627–2638, May 1998. doi:10.1021/la971117c.

[62] K. J. Hanley, T. P. Lodge, and C.-I. Huang. Phase Behavior of a Block Copolymer in Solvents of Varying Selectivity. *Macromolecules*, 33(16):5918–5931, August 2000. doi:10.1021/ma000318b.

[63] M. A. Chavis, D.-M. Smilgies, U. B. Wiesner, and C. K. Ober. Widely Tunable Morphologies in Block Copolymer Thin Films Through Solvent Vapor Annealing Using Mixtures of Selective Solvents. *Advanced Functional Materials*, 25(20):3057–3065, May 2015. doi:10.1002/adfm.201404053.

[64] C. Sinturel, M. Vayer, M. Morris, and M. A. Hillmyer. Solvent Vapor Annealing of Block Polymer Thin Films. *Macromolecules*, 46(14):5399–5415, July 2013. doi:10.1021/ma400735a.

[65] J. N. L. Albert, W.-S. Young, R. L. Lewis, T. D. Bogart, J. R. Smith, and T. H. Epps. Systematic Study on the Effect of Solvent Removal Rate on the Morphology of Solvent Vapor Annealed ABA Triblock Copolymer Thin Films. *ACS Nano*, 6(1):459–466, January 2012. doi:10.1021/nn203776c.

[66] K. Fukunaga, H. Elbs, R. Magerle, and G. Krausch. Large-Scale Alignment of ABC Block Copolymer Microdomains via Solvent Vapor Treatment. *Macromolecules*, 33(3):947–953, February 2000. doi:10.1021/ma9910639.

[67] J. Canning, I. Petermann, and K. Cook. Surface treatment of silicate based glass: base Piranha treatment versus 193nm laser processing. In *Proc. SPIE*, volume 8351, pages 83512N–83512N–5. Sydney, Australia, 2012. doi:10.1117/12.915823.

[68] M. E. McGovern, K. M. R. Kallury, and M. Thompson. Role of Solvent on the Silanization of Glass with Octadecyltrichlorosilane. *Langmuir*, 10(10):3607–3614, October 1994. doi:10.1021/la00022a038.

[69] C. J. Lawrence. The mechanics of spin coating of polymer films. *Physics of Fluids (1958-1988)*, 31(10):2786–2795, October 1988. doi:10.1063/1.866986.

[70] K. Norrman, A. Ghanbari-Siahkali, and N. B. Larsen. 6 Studies of spin-coated polymer films. *Annual Reports Section "C" (Physical Chemistry)*, 101(0):174–201, October 2005. doi:10.1039/B408857N.

[71] W. M. Moreau. *Semiconductor Lithography: Principles, Practices, and Materials*. Springer Science & Business Media, December 2012. ISBN 978-1-4613-0885-0.

[72] M. Geissler and Y. Xia. Patterning: Principles and Some New Developments. *Advanced Materials*, 16(15):1249–1269, August 2004. doi:10.1002/adma.200400835.

[73] H. J. Levinson. *Principles of Lithography*. SPIE Press, January 2005. ISBN 978-0-8194-5660-1.

[74] pyserial. `https://github.com/pyserial/pyserial`.

[75] E. P. Otocka, S. Curran, and R. S. Porter. Photooxidation of polystyrene: Irradiation at 254 and 365 nm. *Journal of Applied Polymer Science*, 28(10):3227–3233, October 1983. doi:10.1002/app.1983.070281017.

[76] K. A. M. dos Santos, P. A. Z. Suarez, and J. C. Rubim. Photo-degradation of synthetic and natural polyisoprenes at specific UV radiations. *Polymer Degradation and Stability*, 90(1):34–43, October 2005. doi:10.1016/j.polymdegradstab.2005.01.038.

[77] Y. D. Gamburg and G. Zangari. *Theory and Practice of Metal Electrodeposition*. Springer New York, New York, NY, 2011. ISBN 978-1-4419-9668-8 978-1-4419-9669-5.

[78] B. A. Miller-Chou and J. L. Koenig. A review of polymer dissolution. *Progress in Polymer Science*, 28(8):1223–1270, 2003. doi:10.1016/S0079-6700(03)00045-5.

[79] python-oceanoptics. `https://github.com/ap--/python-oceanoptics`.

[80] J. I. Goldstein, D. E. Newbury, P. Echlin, D. C. Joy, C. E. Lyman, E. Lifshin, L. Sawyer, and J. R. Michael. *Scanning Electron Microscopy and X-ray Microanalysis*. Springer US, Boston, MA, 2003. ISBN 978-1-4613-4969-3 978-1-4615-0215-9.

[81] G. Haugstad. *Atomic Force Microscopy: Understanding Basic Modes and Advanced Applications*. Wiley, September 2012. ISBN 978-1-118-36069-9.

[82] W. H. Bragg and W. L. Bragg. The Reflection of X-rays by Crystals. *Proceedings of the Royal Society of London A: Mathematical, Physical and Engineering Sciences*, 88(605):428–438, July 1913. doi:10.1098/rspa.1913.0040.

[83] L. A. Feigin, D. I. Svergun, and G. W. Taylor. General Principles of Small-Angle Diffraction. In G. W. Taylor, editor, *Structure Analysis by Small-Angle X-Ray and Neutron Scattering*, pages 25–55. Springer US, 1987. ISBN 978-1-4757-6626-4 978-1-4757-6624-0. doi:10.1007/978-1-4757-6624-0_2.

[84] R. Dehmel, A. Nicolas, M. R. J. Scherer, and U. Steiner. 3D Nanostructured Conjugated Polymers for Optical Applications. *Advanced Functional Materials*, 25(44):6900–6905, November 2015. doi:10.1002/adfm.201502392.

[85] A. Elschner, S. Kirchmeyer, W. Lovenich, U. Merker, and K. Reuter. *PEDOT: Principles and Applications of an Intrinsically Conductive Polymer*. CRC Press, November 2010. ISBN 978-1-4200-6912-9.

[86] G. B. Blanchet, Y.-L. Loo, J. A. Rogers, F. Gao, and C. R. Fincher. Large area, high resolution, dry printing of conducting polymers for organic electronics. *Applied Physics Letters*, 82(3):463–465, January 2003. doi:10.1063/1.1533110.

[87] G. Li, R. Zhu, and Y. Yang. Polymer solar cells. *Nature Photonics*, 6(3):153–161, March 2012. doi:10.1038/nphoton.2012.11.

[88] Y. Yang, G. Yu, J. J. Cha, H. Wu, M. Vosgueritchian, Y. Yao, Z. Bao, and Y. Cui. Improving the Performance of Lithium–Sulfur Batteries by Conductive Polymer Coating. *ACS Nano*, 5(11):9187–9193, November 2011. doi:10.1021/nn203436j.

[89] M.-C. Choi, Y. Kim, and C.-S. Ha. Polymers for flexible displays: From material selection to device applications. *Progress in Polymer Science*, 33(6):581–630, June 2008. doi:10.1016/j.progpolymsci.2007.11.004.

[90] Q. Qiao. *Organic Solar Cells: Materials, Devices, Interfaces, and Modeling.* CRC Press, March 2015. ISBN 978-1-4822-2984-4.

[91] M. Deepa, A. Awadhia, and S. Bhandari. Electrochemistry of poly(3,4-ethylenedioxythiophene)-polyaniline/Prussian blue electrochromic devices containing an ionic liquid based gel electrolyte film. *Physical Chemistry Chemical Physics*, 11(27):5674–5685, June 2009. doi:10.1039/B900091G.

[92] T.-Y. Wei, C.-H. Chen, H.-C. Chien, S.-Y. Lu, and C.-C. Hu. A Cost-Effective Supercapacitor Material of Ultrahigh Specific Capacitances: Spinel Nickel Cobaltite Aerogels from an Epoxide-Driven Sol–Gel Process. *Advanced Materials*, 22(3):347–351, January 2010. doi:10.1002/adma.200902175.

[93] K. J. J. Mayrhofer, D. Strmcnik, B. B. Blizanac, V. Stamenkovic, M. Arenz, and N. M. Markovic. Measurement of oxygen reduction activities via the rotating disc electrode method: From Pt model surfaces to carbon-supported high surface area catalysts. *Electrochimica Acta*, 53(7):3181–3188, February 2008. doi:10.1016/j.electacta.2007.11.057.

[94] A. R. Shahverdi, A. Fakhimi, H. R. Shahverdi, and S. Minaian. Synthesis and effect of silver nanoparticles on the antibacterial activity of different antibiotics against Staphylococcus aureus and Escherichia coli. *Nanomedicine: Nanotechnology, Biology and Medicine*, 3(2):168–171, June 2007. doi:10.1016/j.nano.2007.02.001.

[95] E. J. W. Crossland, S. Ludwigs, M. A. Hillmyer, and U. Steiner. Freestanding nanowire arrays from soft-etch block copolymer templates. *Soft Matter*, 3(1):94–98, 2007. doi:10.1039/b609780d.

[96] E. J. W. Crossland, M. Kamperman, M. Nedelcu, C. Ducati, U. Wiesner, D. M. Smilgies, G. E. S. Toombes, M. A. Hillmyer, S. Ludwigs, U. Steiner, and H. J. Snaith. A Bicontinuous Double Gyroid Hybrid Solar Cell. *Nano Letters*, 9(8):2807–2812, 2009. doi:10.1021/nl803174p.

[97] A. J. Meuler, M. A. Hillmyer, and F. S. Bates. Ordered Network Mesostructures in Block Polymer Materials. *Macromolecules*, 42(19):7221–7250, 2009. doi:10.1021/ma9009593.

[98] H.-Y. Hsueh, H.-Y. Chen, M.-S. She, C.-K. Chen, R.-M. Ho, S. Gwo, H. Hasegawa, and E. L. Thomas. Inorganic Gyroid with Exceptionally Low Refractive Index from Block Copolymer Templating. *Nano Letters*, 10(12):4994–5000, December 2010. doi:10.1021/nl103104w.

[99] M. A. Ghanem, P. N. Bartlett, P. de Groot, and A. Zhukov. A double templated electrodeposition method for the fabrication of arrays of metal nanodots. *Electrochemistry Communications*, 6(5):447–453, May 2004. doi:10.1016/j.elecom.2004.03.001.

[100] M. Miyake, Y.-C. Chen, P. V. Braun, and P. Wiltzius. Fabrication of Three-Dimensional Photonic Crystals Using Multibeam Interference Lithography and Electrodeposition. *Advanced Materials*, 21(29):3012–3015, August 2009. doi:10.1002/adma.200802085.

[101] S. I. Cho, W. J. Kwon, S.-J. Choi, P. Kim, S.-A. Park, J. Kim, S. J. Son, R. Xiao, S.-H. Kim, and S. B. Lee. Nanotube-Based Ultrafast Electrochromic Display. *Advanced Materials*, 17(2):171–175, 2005. doi:10.1002/adma.200400499.

[102] W. Cho, J. Wu, B. S. Shim, W.-F. Kuan, S. E. Mastroianni, W.-S. Young, C.-C. Kuo, I. I. I. Thomas H. Epps, and D. C. Martin. Synthesis and characterization of bicontinuous cubic poly(3,4-ethylene dioxythiophene) gyroid (PEDOT GYR) gels. *Physical Chemistry Chemical Physics*, 17(7):5115–5123, February 2015. doi:10.1039/C4CP04426F.

[103] M. Dietrich, J. Heinze, G. Heywang, and F. Jonas. Electrochemical and spectroscopic characterization of polyalkylenedioxythiophenes. *Journal of Electroanalytical Chemistry*, 369(1):87–92, May 1994. doi:10.1016/0022-0728(94)87085-3.

[104] C. Cutler, M. Bouguettaya, and J. Reynolds. PEDOT Polyelectrolyte Based Electrochromic Films via Electrostatic Adsorption. *Advanced Materials*, 14(9):684–688, May 2002. doi:10.1002/1521-4095(20020503)14:9<684::AID-ADMA684>3.0.CO;2-7.

[105] M. R. J. Scherer, P. M. S. Cunha, and U. Steiner. Labyrinth-Induced Faceted Electrochemical Growth. *Advanced Materials*, 26(15):2403–2407, April 2014. doi:10.1002/adma.201305074.

[106] J. G. Werner, M. R. J. Scherer, U. Steiner, and U. Wiesner. Gyroidal mesoporous multifunctional nanocomposites via atomic layer deposition. *Nanoscale*, 6(15):8736–8742, July 2014. doi:10.1039/C4NR01948B.

[107] S. Salvatore, A. Demetriadou, S. Vignolini, S. S. Oh, S. Wuestner, N. A. Yufa, M. Stefik, U. Wiesner, J. J. Baumberg, O. Hess, and U. Steiner. Tunable 3D Extended Self-Assembled Gold Metamaterials with Enhanced Light Transmission. *Advanced Materials*, 25(19):2713–2716, May 2013. doi:10.1002/adma.201300193.

[108] M. R. J. Scherer, L. Li, P. M. S. Cunha, O. A. Scherman, and U. Steiner. Enhanced Electrochromism in Gyroid-Structured Vanadium Pentoxide. *Advanced Materials*, 24(9):1217–1221, March 2012. doi:10.1002/adma.201104272.

[109] J. M. Ko, H. W. Rhee, S.-M. Park, and C. Y. Kim. Morphology and Electrochemical Properties of Polypyrrole Films Prepared in Aqueous and Nonaqueous Solvents. *Journal of The Electrochemical Society*, 137(3):905–909, January 1990. doi:10.1149/1.2086576.

[110] C. S. C. Bose and K. Rajeshwar. Efficient electrocatalyst assemblies for proton and oxygen reduction: the electrosynthesis and characterization of polypyrrole films containing nanodispersed platinum particles. *Journal of Electroanalytical Chemistry*, 333(1–2):235–256, July 1992. doi:10.1016/0022-0728(92)80394-J.

[111] N. Sakmeche, S. Aeiyach, J.-J. Aaron, M. Jouini, J. C. Lacroix, and P.-C. Lacaze. Improvement of the Electrosynthesis and Physicochemical Properties of Poly(3,4-ethylenedioxythiophene) Using a Sodium Dodecyl Sulfate Micellar Aqueous Medium. *Langmuir*, 15(7):2566–2574, March 1999. doi:10.1021/la980909j.

[112] C. Li, H. Bai, and G. Shi. Conducting polymer nanomaterials: electrosynthesis and applications. *Chemical Society Reviews*, 38(8):2397–2409, July 2009. doi:10.1039/B816681C.

[113] B. H. Jones, K.-Y. Cheng, R. J. Holmes, and T. P. Lodge. Nanoporous Poly(3,4-ethylenedioxythiophene) Derived from Polymeric Bicontinuous Microemulsion Templates. *Macromolecules*, 45(1):599–601, 2011. doi:10.1021/ma202239b.

[114] C. M. Hansen. *Hansen Solubility Parameters: A User's Handbook*. CRC Press, June 2007. ISBN 978-1-4200-0683-4.

[115] C. M. . Estimate, calculated using the HSPiP software by Dr. Charles Hansen, Prof. Steven Abbott, and Dr. Hiroshi Yamamoto, http://hansen-solubility.com/.

[116] C. L. Gaupp, D. M. Welsh, R. D. Rauh, and J. R. Reynolds. Composite Coloration Efficiency Measurements of Electrochromic Polymers Based on 3,4-Alkylenedioxythiophenes. *Chemistry of Materials*, 14(9):3964–3970, September 2002. doi:10.1021/cm020433w.

[117] S. Bhandari, M. Deepa, A. K. Srivastava, C. Lal, and R. Kant. Poly(3,4-ethylenedioxythiophene) (PEDOT)-Coated MWCNTs Tethered to Conducting Substrates: Facile Electrochemistry and Enhanced Coloring Efficiency. *Macromolecular Rapid Communications*, 29(24):1959–1964, December 2008. doi:10.1002/marc.200800550.

[118] G. Sonmez, H. Meng, and F. Wudl. Organic Polymeric Electrochromic Devices: Polychromism with Very High Coloration Efficiency. *Chemistry of Materials*, 16(4):574–580, February 2004. doi:10.1021/cm0301773.

[119] Z. Feng, D. Mo, Z. Wang, S. Zhen, J. Xu, B. Lu, S. Ming, K. Lin, and J. Xiong. Low-potential electrosynthesis of a novel nitrogen analog of PEDOT in an ionic liquid and its optoelectronic properties. *Electrochimica Acta*, 160:160–168, April 2015. doi:10.1016/j.electacta.2015.02.054.

[120] M. Kateb, V. Ahmadi, and M. Mohseni. Fast switching and high contrast electrochromic device based on PEDOT nanotube grown on ZnO nanowires. *Solar Energy Materials and Solar Cells*, 112:57–64, May 2013. doi:10.1016/j.solmat.2013.01.021.

[121] Canon Inc. Canon EOS 450D. `http://www.canon.co.uk/for_home/ product_finder/cameras/digital_slr/eos_450d/`.

[122] M. R. J. Scherer and U. Steiner. Efficient Electrochromic Devices Made from 3D Nanotubular Gyroid Networks. *Nano Letters*, December 2012. doi:10.1021/nl303833h.

[123] D. Maddison and J. Unsworth. Optimization of synthesis conditions of polypyrrole from aqueous solutions. *Synthetic Metals*, 30(1):47–55, April 1989. doi:10.1016/0379-6779(89)90640-1.

[124] D. W. Cai and P. V. Shalaev. Introduction. In *Optical Metamaterials*, pages 1–10. Springer New York, 2010. ISBN 978-1-4419-1150-6 978-1-4419-1151-3. doi:10.1007/978-1-4419-1151-3_1.

[125] J. D. Joannopoulos, S. G. Johnson, J. N. Winn, and R. D. Meade. *Photonic Crystals: Molding the Flow of Light (Second Edition)*. Princeton University Press, October 2011. ISBN 978-1-4008-2824-1.

[126] V. G. Veselago. The Electrodynamics of Substances with Simultaneously negative Values of ϵ and μ. *Soviet Physics Uspekhi*, 10(4), January-February 1968. doi:10.1070/PU1968v010n04ABEH003699.

[127] J. B. Pendry. Negative Refraction Makes a Perfect Lens. *Physical Review Letters*, 85(18):3966–3969, October 2000. doi:10.1103/PhysRevLett.85.3966.

[128] J. Pendry, A. Holden, D. Robbins, and W. Stewart. Magnetism from conductors and enhanced nonlinear phenomena. *Microwave Theory and Techniques, IEEE Transactions on*, 47(11):2075 –2084, November 1999. doi:10.1109/22.798002.

[129] D. R. Smith, W. J. Padilla, D. C. Vier, S. C. Nemat-Nasser, and S. Schultz. Composite Medium with Simultaneously Negative Permeability and Permittivity. *Physical Review Letters*, 84(18):4184–4187, May 2000. doi:10.1103/PhysRevLett.84.4184.

[130] J. B. Pendry, A. J. Holden, W. J. Stewart, and I. Youngs. Extremely Low Frequency Plasmons in Metallic Mesostructures. *Physical Review Letters*, 76(25):4773–4776, June 1996. doi:10.1103/PhysRevLett.76.4773.

[131] J. Valentine, S. Zhang, T. Zentgraf, E. Ulin-Avila, D. A. Genov, G. Bartal, and X. Zhang. Three-dimensional optical metamaterial with a negative refractive index. *Nature*, 455(7211):376–379, September 2008. doi:10.1038/nature07247.

[132] J. B. Pendry. A Chiral Route to Negative Refraction. *Science*, 306(5700):1353–1355, November 2004. doi:10.1126/science.1104467.

[133] K. Hur, Y. Francescato, V. Giannini, S. A. Maier, R. G. Hennig, and U. Wiesner. Three-Dimensionally Isotropic Negative Refractive Index Materials from Block Copolymer Self-Assembled Chiral Gyroid Networks. *Angewandte Chemie International Edition*, 50(50):11985–11989, December 2011. doi:10.1002/anie.201104888.

[134] S. Vignolini, N. A. Yufa, P. S. Cunha, S. Guldin, I. Rushkin, M. Stefik, K. Hur, U. Wiesner, J. J. Baumberg, and U. Steiner. A 3D Optical Metamaterial Made by Self-Assembly. *Advanced Materials*, 24(10):OP23–OP27, March 2012. doi:10.1002/adma.201103610.

[135] S. Salvatore, A. Demetriadou, S. Vignolini, S. S. Oh, S. Wuestner, N. A. Yufa, M. Stefik, U. Wiesner, J. J. Baumberg, O. Hess, and U. Steiner. Tunable 3D Extended Self-Assembled Gold Metamaterials with Enhanced Light Transmission. *Advanced Materials*, 25(19):2713–2716, May 2013. doi:10.1002/adma.201300193.

[136] A. Demetriadou, S. S. Oh, S. Wuestner, and O. Hess. A tri-helical model for nanoplasmonic gyroid metamaterials. *New Journal of Physics*, 14(8):083032, 2012. doi:10.1088/1367-2630/14/8/083032.

[137] P. Farah, A. Demetriadou, S. Salvatore, S. Vignolini, M. Stefik, U. Wiesner, O. Hess, U. Steiner, V. K. Valev, and J. J. Baumberg. Ultrafast Nonlinear Response of Gold Gyroid Three-Dimensional Metamaterials. *Physical Review Applied*, 2(4):044002, October 2014. doi:10.1103/PhysRevApplied.2.044002.

[138] J. A. Dolan, B. D. Wilts, S. Vignolini, J. J. Baumberg, U. Steiner, and T. D. Wilkinson. Optical Properties of Gyroid Structured Materials: From Photonic Crystals to Metamaterials. *Advanced Optical Materials*, 3(1):12–32, January 2015. doi:10.1002/adom.201400333.

[139] S. Hüttner, M. Sommer, A. Chiche, G. Krausch, U. Steiner, and M. Thelakkat. Controlled solvent vapour annealing for polymer electronics. *Soft Matter*, 5(21):4206–4211, October 2009. doi:10.1039/B907147D.

[140] J. M. Marentette and G. R. Brown. Polymer spherulites: I. Birefringence and morphology. *Journal of Chemical Education*, 70(6):435, June 1993. doi:10.1021/ed070p435.

[141] M. Kness. ColorPy. `http://markkness.net/colorpy/ColorPy.html`.

[142] J. Ilavsky. *Nika* : software for two-dimensional data reduction. *Journal of Applied Crystallography*, 45(2):324–328, April 2012. doi:10.1107/S0021889812004037.

[143] P. Welch and M. Muthukumar. Molecular Mechanisms of Polymer Crystallization from Solution. *Physical Review Letters*, 87(21):218302, November 2001. doi:10.1103/PhysRevLett.87.218302.

[144] D. M. Sadler and G. H. Gilmer. Rate-Theory Model of Polymer Crystallization. *Physical Review Letters*, 56(25):2708–2711, June 1986. doi:10.1103/PhysRevLett.56.2708.

[145] G. Reiter. Some unique features of polymer crystallisation. *Chemical Society Reviews*, 43(7):2055–2065, March 2014. doi:10.1039/C3CS60306G.

[146] V. Balsamo, N. Urdaneta, L. Pérez, P. Carrizales, V. Abetz, and A. J. Müller. Effect of the polyethylene confinement and topology on its crystallisation within semicrystalline ABC triblock copolymers. *European Polymer Journal*, 40(6):1033–1049, June 2004. doi:10.1016/j.eurpolymj.2004.01.009.

[147] H.-L. Chen, S.-C. Hsiao, T.-L. Lin, K. Yamauchi, H. Hasegawa, and T. Hashimoto. Microdomain-Tailored Crystallization Kinetics of Block Copolymers. *Macromolecules*, 34(4):671–674, February 2001. doi:10.1021/ma001485e.

[148] Y.-L. Loo, R. A. Register, A. J. Ryan, and G. T. Dee. Polymer Crystallization Confined in One, Two, or Three Dimensions. *Macromolecules*, 34(26):8968–8977, December 2001. doi:10.1021/ma011521p.

[149] J. Maiz, J. Martin, and C. Mijangos. Confinement Effects on the Crystallization of Poly(ethylene oxide) Nanotubes. *Langmuir*, 28(33):12296–12303, August 2012. doi:10.1021/la302675k.

[150] L. Sun, L. Zhu, Q. Ge, R. P. Quirk, C. Xue, S. Z. D. Cheng, B. S. Hsiao, C. A. Avila-Orta, I. Sics, and M. E. Cantino. Comparison of crystallization kinetics in various nanoconfined geometries. *Polymer*, 45(9):2931–2939, April 2004. doi:10.1016/j.polymer.2004.02.068.

[151] A. Boschetti-de Fierro, A. T. Lorenzo, A. J. Müller, H. Schmalz, and V. Abetz. Crystallization Kinetics of PEO and PE in Different Triblock Terpolymers: Effect of Microdomain Geometry and Confinement. *Macromolecular Chemistry and Physics*, 209(5):476–487, March 2008. doi:10.1002/macp.200700434.

[152] L. Zhu, S. Z. D. Cheng, B. H. Calhoun, Q. Ge, R. P. Quirk, E. L. Thomas, B. S. Hsiao, F. Yeh, and B. Lotz. Crystallization Temperature-Dependent Crystal Orientations within Nanoscale Confined Lamellae of a Self-Assembled Crystalline-Amorphous Diblock Copolymer. *Journal of the American Chemical Society*, 122(25):5957–5967, June 2000. doi:10.1021/ja000275e.

[153] L. Zhu, S. Z. D. Cheng, B. H. Calhoun, Q. Ge, R. P. Quirk, E. L. Thomas, B. S. Hsiao, F. Yeh, and B. Lotz. Phase structures and morphologies determined by self-organization, vitrification, and crystallization: confined crystallization in an ordered lamellar phase of PEO-b-PS diblock copolymer. *Polymer*, 42(13):5829–5839, June 2001. doi:10.1016/S0032-3861(00)00902-2.

[154] P. Huang, L. Zhu, S. Z. D. Cheng, Q. Ge, R. P. Quirk, E. L. Thomas, B. Lotz, B. S. Hsiao, L. Liu, and F. Yeh. Crystal Orientation Changes in Two-Dimensionally Confined Nanocylinders in a Poly(ethylene oxide)-b-polystyrene/Polystyrene Blend. *Macromolecules*, 34(19):6649–6657, September 2001. doi:10.1021/ma010671x.

[155] P. Huang, J. X. Zheng, S. Leng, R. M. Van Horn, K.-U. Jeong, Y. Guo, R. P. Quirk, S. Z. D. Cheng, B. Lotz, E. L. Thomas, and B. S. Hsiao.

Poly(ethylene oxide) Crystal Orientation Changes in an Inverse Hexagonal Cylindrical Phase Morphology Constructed by a Poly(ethylene oxide)-block-polystyrene Diblock Copolymer. *Macromolecules*, 40(3):526–534, February 2007. doi:10.1021/ma061871h.

[156] L. Zhu, P. Huang, W. Y. Chen, Q. Ge, R. P. Quirk, S. Z. D. Cheng, E. L. Thomas, B. Lotz, B. S. Hsiao, F. Yeh, and L. Liu. Nanotailored Crystalline Morphology in Hexagonally Perforated Layers of a Self-Assembled PS-b-PEO Diblock Copolymer. *Macromolecules*, 35(9):3553–3562, April 2002. doi:10.1021/ma012184n.

[157] P. A. Weimann, D. A. Hajduk, C. Chu, K. A. Chaffin, J. C. Brodil, and F. S. Bates. Crystallization of tethered polyethylene in confined geometries. *Journal of Polymer Science Part B: Polymer Physics*, 37(16):2053–2068, August 1999. doi: 10.1002/(SICI)1099-0488(19990815)37:16<2053::AID-POLB9>3.0.CO;2-L.

[158] J. P. A. Fairclough, S.-M. Mai, M. W. Matsen, W. Bras, L. Messe, S. C. Turner, A. J. Gleeson, C. Booth, I. W. Hamley, and A. J. Ryan. Crystallization in block copolymer melts: Small soft structures that template larger hard structures. *The Journal of Chemical Physics*, 114(12):5425–5431, March 2001. doi:10.1063/1.1344605.

[159] I. W. Hamley, V. Castelletto, G. Floudas, and F. Schipper. Templated Crystallization from Oriented Gyroid and Hexagonal Melt Phases in a Diblock Copolymer. *Macromolecules*, 35(23):8839–8845, November 2002. doi:10.1021/ma0207069.

[160] L.-Z. Liu, W. Xu, H. Li, F. Su, and E. Zhou. Crystallization and Intriguing Morphologies of Compatible Mixtures of Tetrahydrofuran-Methyl Methacrylate Diblock Copolymer with Poly(tetrahydrofuran). *Macromolecules*, 30(5):1363–1374, March 1997. doi:10.1021/ma960684o.

[161] P. Yang and Y. Han. Crystal Growth Transition from Flat-On to Edge-On Induced by Solvent Evaporation in Ultrathin Films of Polystyrene-b-Poly(ethylene oxide). *Langmuir*, 25(17):9960–9968, September 2009. doi:10.1021/la901108p.

[162] P. Yang, X. Yu, and Y. Han. Transition between crystallization and microphase separation in PS-b-PEO thin film Influenced by solvent vapor selectivity. *Polymer*, 51(21):4948–4957, October 2010. doi:10.1016/j.polymer.2010.08.025.

[163] J. Yang, Y. Liang, and C. C. Han. Crystallization-Driven Surface Segregation and Surface Structures in Poly(l-lactide)-block-Poly(ethylene

glycol) Copolymer Thick Films. *Langmuir*, 30(1):394–401, January 2014. doi:10.1021/la4041387.

[164] C. Darko, I. Botiz, G. Reiter, D. W. Breiby, J. W. Andreasen, S. V. Roth, D.-M. Smilgies, E. Metwalli, and C. M. Papadakis. Crystallization in diblock copolymer thin films at different degrees of supercooling. *Physical Review E*, 79(4):041802, April 2009. doi:10.1103/PhysRevE.79.041802.

[165] J. Xu, Y. Ma, W. Hu, M. Rehahn, and G. Reiter. Cloning polymer single crystals through self-seeding. *Nature Materials*, 8(4):348–353, April 2009. doi:10.1038/nmat2405.

[166] U. Holzwarth and N. Gibson. The Scherrer equation versus the 'Debye-Scherrer equation'. *Nature Nanotechnology*, 6(9):534–534, September 2011. doi:10.1038/nnano.2011.145.

[167] E. Kretschmann and H. Raether. Radiative Decay of Non Radiative Surface Plasmons Excited by Light. *Zeitschirft für Naturforschung*, 23a:2135–2136, November 1968.

[168] E. Kretschmann. Die bestimmung optischer konstanten von metallen durch anregung von oberflächenplasmaschwingungen. *Zeitschrift für Physik*, 241(4):313–324, August 1971. doi:10.1007/BF01395428.

[169] A. V. Zayats, I. I. Smolyaninov, and A. A. Maradudin. Nano-optics of surface plasmon polaritons. *Physics Reports*, 408(3–4):131–314, March 2005. doi:10.1016/j.physrep.2004.11.001.

[170] B. Liedberg, C. Nylander, and I. Lunström. Surface plasmon resonance for gas detection and biosensing. *Sensors and Actuators*, 4:299–304, 1983. doi:10.1016/0250-6874(83)85036-7.

[171] J. Homola, S. S. Yee, and G. Gauglitz. Surface plasmon resonance sensors: review. *Sensors and Actuators B: Chemical*, 54(1–2):3–15, January 1999. doi:10.1016/S0925-4005(98)00321-9.

[172] C.-M. Wu, Z.-C. Jian, S.-F. Joe, and L.-B. Chang. High-sensitivity sensor based on surface plasmon resonance and heterodyne interferometry. *Sensors and Actuators B: Chemical*, 92(1–2):133–136, July 2003. doi:10.1016/S0925-4005(03)00157-6.

[173] M. Mrksich, G. B. Sigal, and G. M. Whitesides. Surface Plasmon Resonance Permits in Situ Measurement of Protein Adsorption on Self-Assembled Monolayers of Alkanethiolates on Gold. *Langmuir*, 11(11):4383–4385, November 1995. doi:10.1021/la00011a034.

[174] K. V. Gobi, H. Iwasaka, and N. Miura. Self-assembled PEG monolayer based SPR immunosensor for label-free detection of insulin. *Biosensors and Bioelectronics*, 22(7):1382–1389, February 2007. doi:10.1016/j.bios.2006.06.012.

[175] A. Otto. Excitation of nonradiative surface plasma waves in silver by the method of frustrated total reflection. *Zeitschrift für Physik*, 216(4):398–410, August 1968. doi:10.1007/BF01391532.

[176] R. Karlsson. SPR for molecular interaction analysis: a review of emerging application areas. *Journal of Molecular Recognition*, 17(3):151–161, May 2004. doi:10.1002/jmr.660.

[177] D. B. Shuwen Zeng. Nanomaterials enhanced surface plasmon resonance for biological and chemical sensing applications. *Chemical Society Reviews*, 43:3426–3452, 2014. doi:10.1039/c3cs60479a.

[178] B. Johnsson, S. Löfås, and G. Lindquist. Immobilization of proteins to a carboxymethyldextran-modified gold surface for biospecific interaction analysis in surface plasmon resonance sensors. *Analytical Biochemistry*, 198(2):268–277, November 1991. doi:10.1016/0003-2697(91)90424-R.

[179] W. A. Weimer and M. J. Dyer. Tunable surface plasmon resonance silver films. *Applied Physics Letters*, 79(19):3164–3166, November 2001. doi:10.1063/1.1416473.

[180] T. J. Constant, A. P. Hibbins, A. J. Lethbridge, J. R. Sambles, E. K. Stone, and P. Vukusic. Direct mapping of surface plasmon dispersion using imaging scatterometry. *Applied Physics Letters*, 102(25):251107, June 2013. doi:10.1063/1.4812482.

[181] B. P. Nelson, T. E. Grimsrud, M. R. Liles, R. M. Goodman, and R. M. Corn. Surface Plasmon Resonance Imaging Measurements of DNA and RNA Hybridization Adsorption onto DNA Microarrays. *Analytical Chemistry*, 73(1):1–7, January 2001. doi:10.1021/ac0010431.

[182] J. S. Shumaker-Parry and C. T. Campbell. Quantitative Methods for Spatially Resolved Adsorption/Desorption Measurements in Real Time by Surface Plasmon Resonance Microscopy. *Analytical Chemistry*, 76(4):907–917, February 2004. doi:10.1021/ac034962a.

[183] S. Vignolini, E. Moyroud, B. J. Glover, and U. Steiner. Analysing photonic structures in plants. *Journal of The Royal Society Interface*, 10(87):20130394–20130394, July 2013. doi:10.1098/rsif.2013.0394.

[184] P. Vukusic and D. Stavenga. Physical methods for investigating structural colours in biological systems. *Journal of The Royal Society Interface*, 6(Suppl_2):S133–S148, April 2009. doi:10.1098/rsif.2008.0386.focus.

[185] P. Yeh. *Optical waves in layered media*. Wiley-Interscience, Hoboken NJ, 2005.

[186] B. D. Wilts, K. Michielsen, H. De Raedt, and D. G. Stavenga. Sparkling feather reflections of a bird-of-paradise explained by finite-difference time-domain modeling. *Proceedings of the National Academy of Sciences of the United States of America*, 111:4363–4368, March 2014. doi:10.1073/pnas.1323611111.

[187] J. C. Hoogvliet and W. P. van Bennekom. Gold thin-film electrodes: an EQCM study of the influence of chromium and titanium adhesion layers on the response. *Electrochimica Acta*, 47(4):599–611, November 2001. doi:10.1016/S0013-4686(01)00793-9.

[188] H.-T. Rong, S. Frey, Y.-J. Yang, M. Zharnikov, M. Buck, M. Wühn, C. Wöll, and G. Helmchen. On the Importance of the Headgroup Substrate Bond in Thiol Monolayers: A Study of Biphenyl-Based Thiols on Gold and Silver. *Langmuir*, 17(5):1582–1593, March 2001. doi:10.1021/la0014050.

[189] J. Sagiv. Organized monolayers by adsorption. 1. Formation and structure of oleophobic mixed monolayers on solid surfaces. *Journal of the American Chemical Society*, 102(1):92–98, January 1980. doi:10.1021/ja00521a016.

[190] E. L. Hanson, J. Schwartz, B. Nickel, N. Koch, and M. F. Danisman. Bonding Self-Assembled, Compact Organophosphonate Monolayers to the Native Oxide Surface of Silicon. *Journal of the American Chemical Society*, 125(51):16074–16080, December 2003. doi:10.1021/ja035956z.

[191] P. Metrangolo, H. Neukirch, T. Pilati, and G. Resnati. Halogen Bonding Based Recognition Processes: A World Parallel to Hydrogen Bonding†. *Accounts of Chemical Research*, 38(5):386–395, May 2005. doi:10.1021/ar0400995.

[192] P. Metrangolo, T. Pilati, G. Terraneo, S. Biella, and G. Resnati. Anion coordination and anion-templated assembly under halogen bonding control. *CrystEngComm*, 11(7):1187–1196, July 2009. doi:10.1039/B821300C.

[193] P.-O. Löwdin. On the Non-Orthogonality Problem Connected with the Use of Atomic Wave Functions in the Theory of Molecules and Crystals. *The Journal of Chemical Physics*, 18(3):365–375, March 1950. doi:10.1063/1.1747632.

[194] A. H. Pakiari and Z. Jamshidi. Nature and Strength of M-S Bonds (M = Au, Ag, and Cu) in Binary Alloy Gold Clusters. *The Journal of Physical Chemistry A*, 114(34):9212–9221, September 2010. doi:10.1021/jp100423b.

[195] M. P. Seah. A review of the analysis of surfaces and thin films by AES and XPS. *Vacuum*, 34(3–4):463–478, March 1984. doi:10.1016/0042-207X(84)90084-8.

[196] Q. Cheng, S. Xu, and K. K. Ostrikov. Controlled-bandgap silicon nitride nanomaterials: deterministic nitrogenation in high-density plasmas. *Journal of Materials Chemistry*, 20(28):5853–5859, July 2010. doi:10.1039/C0JM01060J.

[197] M. Sansotera, W. Navarrini, L. Magagnin, C. L. Bianchi, A. Sanguineti, P. Metrangolo, and G. Resnati. Hydrophobic carbonaceous materials obtained by covalent bonding of perfluorocarbon and perfluoropolyether chains. *Journal of Materials Chemistry*, 20(39):8607–8616, September 2010. doi:10.1039/C0JM02077J.

[198] M. Boterashvili, T. Shirman, S. R. Cohen, G. Evmenenko, P. Dutta, P. Milko, G. Leitus, M. Lahav, and M. E. van der Boom. Interfacial halogen bonding probed using force spectroscopy. *Chemical Communications*, 49(34):3531–3533, April 2013. doi:10.1039/C3CC40378E.

[199] D. M. Lemal. Perspective on Fluorocarbon Chemistry. *The Journal of Organic Chemistry*, 69(1):1–11, January 2004. doi:10.1021/jo0302556.

[200] C. Jie-Rong and T. Wakida. Studies on the surface free energy and surface structure of PTFE film treated with low temperature plasma. *Journal of Applied Polymer Science*, 63(13):1733–1739, March 1997. doi: 10.1002/(SICI)1097-4628(19970328)63:13<1733::AID-APP4>3.0.CO;2-H.

[201] A. F. Thünemann, A. Lieske, and B.-R. Paulke. Low Surface Energy Coatings from Waterborne Nano-Dispersions of Polymer Complexes. *Advanced Materials*, 11(4):321–324, March 1999. doi: 10.1002/(SICI)1521-4095(199903)11:4<321::AID-ADMA321>3.0.CO;2-M.

[202] J. Tsibouklis and T. Nevell. Ultra-Low Surface Energy Polymers: The Molecular Design Requirements. *Advanced Materials*, 15(7-8):647–650, April 2003. doi:10.1002/adma.200301638.

[203] H. W. Fox and W. A. Zisman. The spreading of liquids on low energy surfaces. I. polytetrafluoroethylene. *Journal of Colloid Science*, 5(6):514–531, December 1950. doi:10.1016/0095-8522(50)90044-4.